Delft University of Technology

Prognostics and health management of safety relevant electronics for autonomous driving

Prisacaru, Alexandru

DOI
10.4233/uuid:a586c76e-ff97-4f24-9b0f-f62417539495

Publication date
2021

Document Version
Final published version

Citation (APA)
Prisacaru, A. (2021). *Prognostics and health management of safety relevant electronics for autonomous driving*. [Dissertation (TU Delft), Delft University of Technology]. https://doi.org/10.4233/uuid:a586c76e-ff97-4f24-9b0f-f62417539495

Important note
To cite this publication, please use the final published version (if applicable).
Please check the document version above.

Copyright
Other than for strictly personal use, it is not permitted to download, forward or distribute the text or part of it, without the consent of the author(s) and/or copyright holder(s), unless the work is under an open content license such as Creative Commons.

Takedown policy
Please contact us and provide details if you believe this document breaches copyrights.
We will remove access to the work immediately and investigate your claim.

This work is downloaded from Delft University of Technology.
For technical reasons the number of authors shown on this cover page is limited to a maximum of 10.

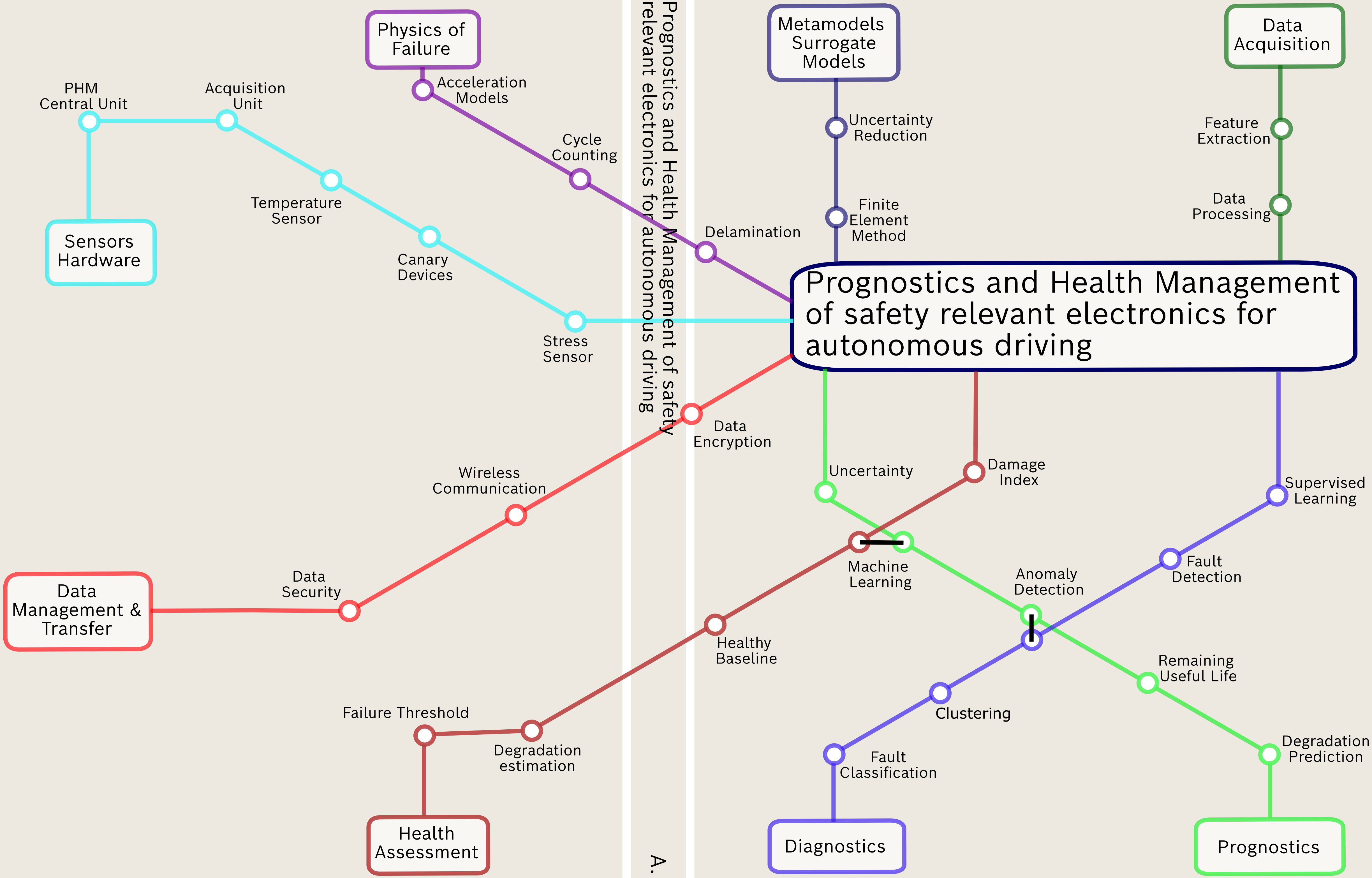

Prognostics and Health Management of safety relevant electronics for autonomous driving

A. Prisacaru

Alexandru Prisacaru

ISBN 978-94-6421-400-0
9 789464 214000

Delft University of Technology

PROGNOSTICS AND HEALTH MANAGEMENT OF SAFETY RELEVANT ELECTRONICS FOR AUTONOMOUS DRIVING

PROGNOSTICS AND HEALTH MANAGEMENT OF SAFETY RELEVANT ELECTRONICS FOR AUTONOMOUS DRIVING

Proefschrift

ter verkrijging van de graad van doctor
aan de Technische Universiteit Delft,
op gezag van de Rector Magnificus Prof. dr. ir. T.H.J.J. van der Hagen,
voorzitter van het College voor Promoties,
in het openbaar te verdedigen op woensdag 23 juni 2021 om 12:30 uur

door

Alexandru PRISACARU

Master of Science in Structural Engineering
Technische Universiteit 'Gheorghe Asachi' Iasi, Roemenië
Master of Science in Computational Engineering
Ruhr Universiteit Bochum, Duitsland
geboren te Comanesti, Roemenië.

Dit proefschrift is goedgekeurd door de promotoren.

Samenstelling promotiecommissie:

Rector Magnificus,	voorzitter
Prof.dr. G.Q. Zhang	Technische Universiteit Delft, promotor
Dr. P.J. Gromala	Robert Bosch GmbH, copromotor
Onafhankelijke leden:	
Prof.dr. B. Han	Maryland University, USA
Prof.dr. X.J. Fan	Lamar University, USA
Prof.dr. C.J. Bailey	University of Greenwich, UK
Prof.dr.ir. W.D. van Driel	Technische Universiteit Delft
Prof.dr.ir. S. Hamdioui	Technische Universiteit Delft
Prof.dr.ir. P.M. Sarro	Technische Universiteit Delft, reservelid

Keywords: prognostics, piezoresitive stress sensor, diagnostics, machine learning, reliability, electronic packages, virtual twin.

Printed by: Ipskamp drukkers

Cover: Alexandru Prisacaru

Copyright © 2021 by A. Prisacaru

ISBN 978-94-6421-400-0

An electronic version of this dissertation is available at
http://repository.tudelft.nl/.

Contents

1 Introduction **1**
1.1 Background and Motivation 2
1.1.1 Scientific Challenges 4
1.1.2 Novelty. 5
1.2 Outline of the Thesis 6
References 6

2 Prognostics and Health Monitoring of Electronic System: A Review **7**
2.1 Introduction 8
2.2 PHM Frameworks/Architectures in electronic systems 10
2.2.1 System definition 11
2.2.2 Strategies/Schematics used in implementation 11
2.3 Sensor and parameter selection. 12
2.3.1 Sensors used in electronic systems and the parameters related to the sensors. 12
2.3.2 Non-physical software parameters. 13
2.4 An overview of Data-driven approaches. 14
2.4.1 Fault detection. 14
2.4.2 Fault Diagnostics. 14
2.4.3 Fault prediction 15
2.4.4 Case studies 16
2.5 An overview of Model-driven approaches. 18
2.5.1 PoF description and FMMEA. 19
2.5.2 Models used 19
2.5.3 Case studies 20
2.6 Summary and recommendation 21
2.7 Conclusions. 22
References 23

3 On the Accuracy of CMOS-based Piezoresistive Stress Sensor: Theoretical Review and Experimental Validation **29**
3.1 Introduction 29
3.2 Fundamentals of CMOS-Based Stress Sensor 31
3.3 Sensor Chip and Data Acquisition. 34
3.3.1 Sensor Chip Construction 34
3.3.2 Data Acquisition Unit 36
3.4 Uncertainty of Sensor Signal 36
3.4.1 Random Measurement Uncertainties 36
3.4.2 Systematic Uncertainty Associated with Residual Stresses 38

3.5 Accuracy of Load-Induced Stress Measurements 40
3.5.1 Test Vehicle and Numerical Model Construction 40
3.5.2 Numerical Model Construction 40
3.5.3 Model Validation by Moiré interferometry 42
3.5.4 Accuracy of Load-induced Stress Measurements 44
3.6 Conclusion 46
References 46

4 In-situ Failure Detection of Electronic Control Units Using Piezoresistive Stress Sensor **51**
4.1 iForce Sensor 53
4.2 Proposed Algorithm 55
4.3 Implementation 57
4.3.1 Test Vehicle 57
4.3.2 Initial Data 58
4.3.3 Data from Thermal Cycling Data 60
4.3.4 Failure Analysis by SAM 64
4.3.5 Data understanding using visual analytics 64
4.4 Data Analysis by the Proposed Algorithm 64
4.4.1 Health Assessment 64
4.4.2 Damage Quantification 67
4.4.3 Feature Extraction 68
4.4.4 Fault Classification 70
4.5 Conclusion 74
References 74

5 Degradation Prediction of Electronic Packages using Data-driven Approach **77**
5.1 Introduction 78
5.2 Methodology 79
5.2.1 Acquisition Unit and Central PHM Unit 80
5.3 Experimental Setup and Test Vehicle 82
5.3.1 Test Vehicle 82
5.4 Experimental Results 82
5.4.1 Data Preprocessing 84
5.4.2 Visualization Metric 86
5.4.3 Failure Analysis 87
5.5 Diagnostics 89
5.5.1 Fault Detection 89
5.5.2 Fault Classification 90
5.5.3 Fault Location 90
5.6 Health Assessment and Prognostics 92
5.6.1 Degradation estimation 92
5.7 Conclusion 95
References 95

6 Towards Virtual Twin for Electronic Packages in Automotive Field 99
6.1 Introduction 100
6.1.1 Automotive Electronics 101
6.1.2 Machine Learning 101
6.2 Experiment 103
6.2.1 Test Vehicle 103
6.2.2 Stress Evaluation 104
6.2.3 Acquisition Unit 105
6.2.4 Delamination validation through SAM images 106
6.2.5 Data from Thermal Cycling Data 106
6.2.6 Thermal Deformation with Moiré interferometry 107
6.3 Simulation Data. 108
6.4 Surrogate Modelling 113
6.4.1 Back Propagation Artificial Neural Network 113
6.5 Conclusions. 117
References 117

7 Concluding Remarks and Recommendations 121

Summary 123

Samenvatting 127

Acknowledgements 131

Curriculum Vitæ 133

List of Publications 135
.1 Journal Papers 135
.2 Conference Papers 136
.3 Book Chapter 137
.4 Patent 137

1

INTRODUCTION

1.1. BACKGROUND AND MOTIVATION

SAfety relevant electronics refers to a part of the electronic system that belongs to the overall safety of the car functionalities. In applications such as automated driving and electrification, assuring no-fault or avoiding unreasonable risks due to hardware reliability is mandatory. Therefore, two concepts have been used so far. First, mainly used today, is called redundancy. The system itself has a physical twin built-in to take over the functionality immediately when the initial one does not fulfill the requirements anymore. The second concept, Prognostics and Health Management (PHM), is a broad combination of techniques such as parameter monitoring, fault detection, classification, prediction, and decision-making. Using this concept assures the replacement of the system before it cannot fulfill the requirements. The second would be a better option from perspectives like resources, product life cycle, design optimization, new business models, and environment protection. However, considering the complexity of electronics and their rapid design change, this will be an utmost challenge.

PHM technology was for many years restricted by the development of the equipment, e.g., data acquisition units, sensors, computing power, and communication units. In addition, data processing, transmission, and science were not sufficiently studied and advanced enough. Recently, the additional hardware price reduction and the maturity level of Machine Learning (ML) made PHM technology evolve. Another trend, which comes in the aid of PHM, is big data, cloud computing power, greater connectivity, and advancements in sensors and signal processing. The ultimate goal is to use all these capabilities and interdisciplinary sciences to emulate virtual twins of the physical assets (and replace the physical twin in the redundancy concept). Models and algorithms are deployed to simulate manufacturing processes and physical functions to predict failures and when to do repairs or replacements. Furthermore, this process will improve the product quality and customer experience. [1]

The real driving force of PHM in the automotive field is automated driving (AD). Certain vital functions need monitoring capabilities, such as the driving assistance, braking, and steering system. The near future includes a world of complex electronic systems aimed to increase user experience and the safety of current technologies. Every German automobile manufacturer is working on AD to some degree (as individual research or part of a consortium). The advent of autonomous driving depends on the development of new technologies hand-in-hand with ML. Self-driving technologies are the most notorious as they are presented as the solution to a virtually impossible problem to solve using hard coding. Nevertheless, any generated solution will depend on the reliability and safety of the operation of the available hardware. Two new requirements arise: (i) Make the best possible software to guarantee safe performance and (ii) make the best hardware to drive this software. The goal is to aim to hardware with reliability close to 100%, which predicts a failure before it happens.

This work relates to the operational safety of electronics in the automotive industry. In automotive electronics, an Electronic Control Unit (ECU) is an embedded system that controls one or more of the electronic systems or subsystems in a transport vehicle, such as a door control unit, engine control unit, and speed control unit. As Figure 1.1 illustrates, the average number of semiconductors on a car will further increase in the following years. The more complexity a car processes, the more semiconductors it has.

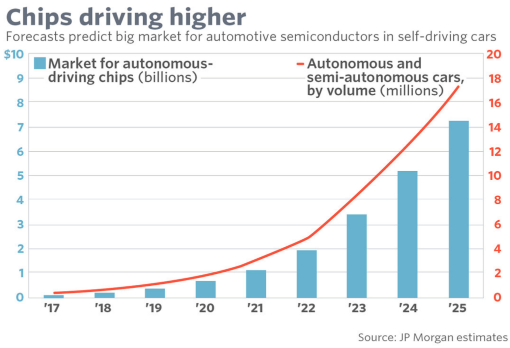

Figure 1.1: Number of semiconductors in a car [2].

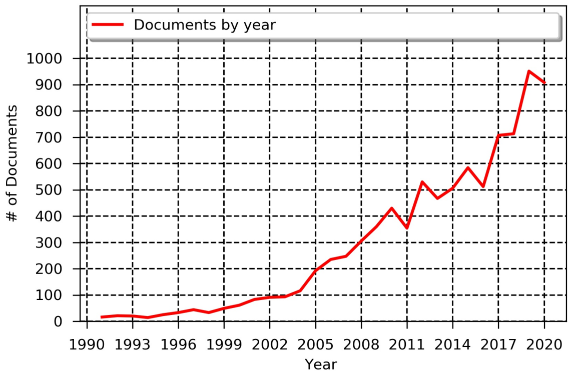

Figure 1.2: Number of documents related to PHM in engineering field according to Scopus.

Therefore, the importance of electronics reliability will also increase. To create a PHM technology for every electronic in the future car would be almost impossible. However, reducing it to a few crucial electronics that sustain essential functions is mandatory.

The number sees the attention and its necessity in the engineering world of documents rise shown by Scopus in Figure 1.2. The scientific community is showing an increased interest in PHM and its benefits. Therefore, not only in automotive engineering, PHM technologies are still to be developed. This Thesis is proposing for the first time a system-level PHM framework applied to the automotive ECUs.

Figure 1.3 depicts a typical ECU used for engine control. The processor is packaged in a module with hundreds of other components, like analog-to-digital converters, signal conditioners, communication chips, high-level digital outputs on a multi-layer circuit board.

Electronic components have a wide range of failure modes, such as packaging failure, contact failure, printed circuit board failure. The majority of electronic failures are packaging-related.[3] Electronic Packaging serves as a protection of the inside circuits

1

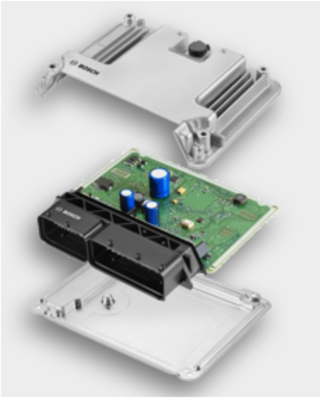

Figure 1.3: Automotive ECU[2].

from the environment, which is susceptible to improper environmental factors. The materials of packaging are different, so are their thermal expansion coefficients. Since ECUs in cars are often exposed to high and low temperatures periodically, the environmental load is similar to thermal cycling. Suffered from thermal cycling, materials in packaging deform differently, which causes mechanical stresses in the package. Exceeding stresses can crack the semiconductor dies, tear off the lead frame or cause cracks in the packaging itself. Humidity could then get into the package and corrode metallic leads. All these lead to the partial non-functionality or even full non-functionality of this component, which might cause failure eventually. Therefore, in this Thesis, the use case is the electronic package. The biggest advantage of this use case is that the entire framework can be easily applied to any other electronic package used in the automotive field. In the following few chapters, a PHM framework is built based on the current state of the art and then deployed in automotive electronics in few applications.

1.1.1. SCIENTIFIC CHALLENGES

- Tremendous amount of data to be evaluated and interpreted “quantitatively” despite inherent random noise

- Numerous variables to be considered for experiments and simulation

- Unique algorithms developments for piezoresistive stress sensors, considering the state-of-art machine learning/big data/deep learning

- Remaining Useful Life (RUL) calculation based on degrading features extracted from the stress evolution before failure

- Inherent uncertainty of the data-driven approach and the model-driven approach employed in failure prediction

1.1.2. NOVELTY

- Development of novel data acquisition unit for piezoresistive stress sensor that provides unique capabilities of online monitoring and data encryption
- Development of package structures for advanced piezoresistive stress sensor based on TQFP and QFN (typical automotive electronic packages)
- Successful implementation of Prognostics and Health Management in the field of automotive electronics using the unit and sensors; specific technical achievements include:
  - Detection of the delamination during accelerated testing
  - Quantitative estimation of the state of health of automotive electronic packages
  - Quantitative estimation of package degradation using Artificial Intelligence
  - Implementation of the concept of Digital Twin for the effect of aging/drifting of high-temperature storage on mechanical stresses

1.2. Outline of the Thesis

The outline of the research presented in this Thesis is shortly summarized below for each chapter.

Chapter 2 starts with theoretical fundamentals regarding Reliability, PHM, and Machine Learning applied for electronics found in the literature. Later, a review of state of the art in ML methods applied for Prognostics and Health Management (PHM) in electronics is presented. Chapter 3 gives a broad theoretical overview of the piezoresistive stress sensor used in this Thesis. Experimental validation describes the accuracy and the uncertainty of the sensor when used for reliability temperature cycles. Chapter 4 introduces the PHM framework developed for automotive applications. An overmolded electronic control unit is used to study the feasibility of using stress sensors in detecting and classifying the failure. Chapter 5 extends the PHM framework from Chapter 4 into a general one for automotive electronics. Creates a definition of degradation signal and describes the machine learning models set up and how they were trained. This chapter includes the validation of the experiment, quantifies the fault detection, classification and estimation. Chapter 6 presents an analysis of a built surrogate model to directly predict the stresses that produce the delamination instead of a degradation signal. Finally, Chapter 6 ends this Thesis by presenting the conclusions and some advice for further research on this area.

References

[1] Z. Liu, Z. Jia, C.-M. Vong, J. Han, C. Yan, and M. Pecht, *A patent analysis of prognostics and health management (phm) innovations for electrical systems,* IEEE Access **6**, 18088 (2018).

[2] R. B. S. Consultants, *Consolidation in Vehicle Elctronic Architechtures* (2015).

[3] F. Metzger, *Failure Modes of Electronics*, Vol. vol. 88 (The English Press, 2010).

2

Prognostics and Health Monitoring of Electronic System: A Review

Miniaturization of electronics, reduction of time to market, and new functionalities in the current context of autonomous driving, electrification, and connectivity, are bringing new reliability challenges. Prognostics and Health Management (PHM) can be used effectively to address some of the fundamental challenges, particularly new challenges associated with the transfer of consumer electronics to the automotive industry. The concept of PHM is not new, but its application to electronic systems is relatively new. It is expected that the PHM demand for electronic systems would continuously increase as autonomous driving is being realized. This chapter attempts to summarize the recent studies in the system-level PHM of electronic systems. Condition monitoring (CM) techniques and prognostics methods used for the PHM of electronic systems are reviewed first. Various implementation examples are followed using different system classifications. The findings from this review are expected to offer a technical summary of accomplishments and challenges during the application of PHM for electronic systems and to identify future research tasks to make the PHM a more viable tool for the reliability assessment of electronic systems.

Parts of this chapter have been published in EurosimE conference, (2016) [1].

2.1. INTRODUCTION

Functional safety is a crucial reason for the development of PHM, and it has been widely implemented in avionics and large mechanical systems. Compared to mechanical systems, the degradation of electronics is somewhat difficult to detect due to the geometric scales of components, and their complex architectures [2]. Quantification of the degradation and fault progression in an electronic system is even more difficult since not all faults necessarily lead to system failure or functionality loss [3]. In addition, there is an uprising trend in which the industry shifts to increase system availability. This happens because some businesses are not selling the product anymore but lease it or sell the system with the services included.

The electronics industry encounters an ever-increasing demand for cost reduction, short time-to-market, miniaturization, higher density/compactness of components, rapid upgrades, and enhanced customer satisfaction. All of these create numerous reliability problems. In some cases, solutions are available only by allowing trade-offs, inducing loss of profit, time, and product availability. Implementing PHM on a system level at the design stage [4] as well as the qualification phase [2], can help solving most of the problems. PHM of electronic components and systems can offer competitive advantages as it improves performance, reliability, safety, maintainability, and availability [5].

In Telecom, it is called Intelligent Platform Management Interface (IPMI), in aerospace, Integrated Vehicle Health Management (IVHM) [6], in electronics, Prognostics and Health Management [7]. In the maintenance perspective, it is Condition Monitoring (CM) [8]. Implementations may vary in different applications, but the same basic principles are employed. In CM, the system/equipment health is monitored by the sensors, and predictive measures are taken before the incipient failure. In contrast, in Prognostics and Health Management, the Remaining Useful Life (RUL) is calculated at any time.

Prognostics has not been applied to electronic systems until recently. It may be attributed to the fact that: The time to failure is not readily quantifiable. Prognostics techniques are not ready for the complexity of electronic systems. Safety is not a significant issue. PHM for electronics has first been introduced in avionics, followed by automotive, and more recently, in consumer electronics.

Due to the large variety of techniques used for PHM, it is challenging to study and review all of the exiting techniques. Hence, this study focuses on the most relevant techniques to integrate PHM in electronic systems and subsystems and highlights the papers that offer a solution to the system-level PHM problems. PHM is an algorithm or a set of algorithms based on measurements and models, which collect as input already known information about the system/structure and data from strategically positioned sensors. Then it subsequently provides, as an output, different levels of prognostics such as failure detection, diagnostics, and prediction. Various levels of prognostics require different strategies/algorithms for successful implementation.

As depicted in Figure 2.1, a well-implemented prognostic methodology should include the following items:

- Sensors for prognostics
- Data collection, processing, reduction, and feature extraction
- Data Security and integrity

- Identification and analyze precursors, Risk and uncertainty analysis
- Health assessment, anomaly detection, fault recognition, fault classification, fault propagation
- Physics-of-Failure (PoF), Damage Models, Reliability testing
- Model Order Reduction, Metamodels, Surrogate Models of Finite Element Methods (FEM) or any other Physical Model

Methods used for recording relevant loading information include measuring the temperatures [9],[7], installing canary devices [10], collecting data about operational conditions [11] or usage hours[9], using strain gauges to measure the strain on solder joints, using piezoresistive stress sensor inside a system package [12] and detecting when the performance of a system degrades [7].

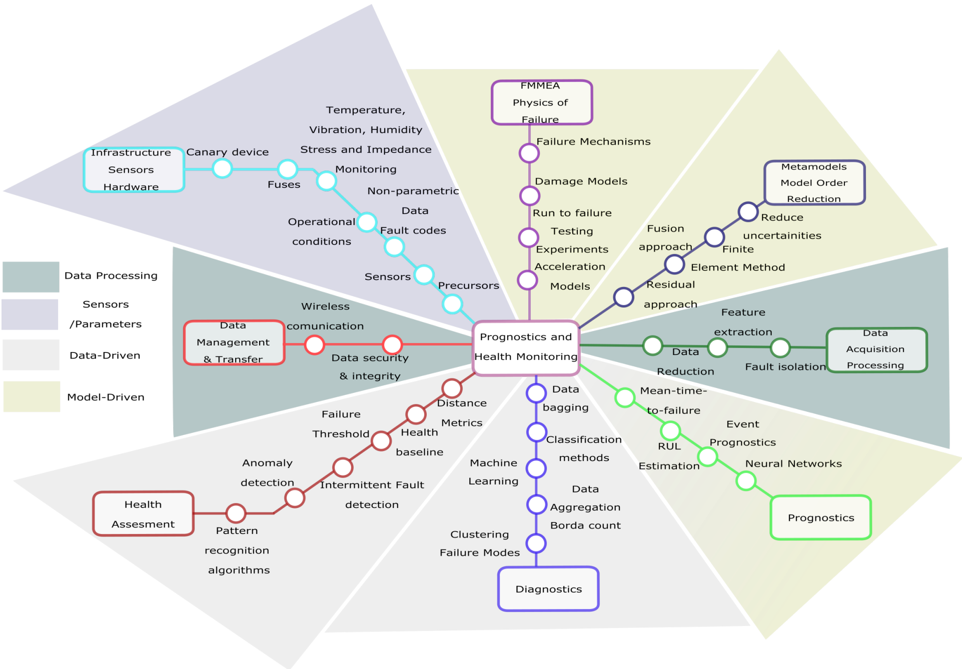

Figure 2.1: PHM for Electronic Systems Metro-Map. The main areas are Data Processing, Sensors, Data-Driven and Model-Driven Approaches.

PHM algorithms performance relies on [2], [3]:

- real-time sensor data which contains relevant structural data
- accurate data collection (limited resources, noise cancellation and so on)
- accurate,robust and effectiveness fault detection algorithm
- reduced false alarms

- accurate models for prognostics

Three approaches of PHM are (1) data-driven approach, (2) model-driven approach, and (3) fusion approach, which combines the first two approaches. Due to the limited availability of the fusion approach, this chapter focuses on the first two. The data-driven approach aims at transforming the raw data from sensors into relevant information, which is used to learn models for health assessment and RUL prediction. The model-based approach deals with predicting the RUL of systems by using numerical models to simulate the physical behavior of degradation mechanisms.

This chapter will review the two PHM approaches implemented for electronic systems, emphasizing the subsystem and system levels. The concepts and case studies found in the literature will be presented.

2.2. PHM FRAMEWORKS/ARCHITECTURES IN ELECTRONIC SYSTEMS

In this section, several PHM frameworks for electronic systems found in the literature are presented. The number of frameworks far exceeds the number of actual case studies based on the electronic system. The reason behind this is the considerable complexity and the non-linearity of the systems that these techniques are to be applied to or the insufficient technological breakthroughs. Also, in [13] it is stated that one of the reasons for the lack of progress is the available data on which to apply predictive algorithms. Even with a lot more possibilities available now, there are few electronic systems equipped with sensors that can support the collection of data. A PHM approach utilizes measurements, models, and software to perform incipient fault detection, condition assessment, and failure progression prediction [15]. PHM can be performed on different completion stages, starting from fault/anomaly detection through diagnostics to fault prediction. A fault is defined as the operation outside of specifications, while failure is defined as the lack of operation [16]. Another advantage of PHM is that it can be implemented in steps, for example, in the design, development stage [17], production and released products [18]. An essential requirement in any prognostics method is identifying the appropriate parameter(s), which can assess impending failure. It is usually called precursor parameter selection. Also, a failure precursor is an event that signifies impending failure [11]. Although effective, most approaches to PHM focused on monitoring failure precursor indications that do not require system failures to be deterministic but do require that the selected precursor has a deterministic link to the actual system failure [19].

One way of identifying and select the precursor parameters is to apply Fault Mode and Mechanisms Effect Analysis (FMMEA) proposed by Pecht et al. [20]. A failure mechanism is defined as the physical phenomena causing the onset of failure. Common examples of failure mechanisms are fatigue, fracture, corrosion, cracking, and so on. Failure mode defines how a system or device fails, for example, overheating, unexpected shutdown, reduced performance [21], lack of electrical contact. Also, based on FMMEA, a decision is made on where to place the sensors. It is used along with the PoF approach, which utilizes knowledge of a product's life cycle loading and failure mechanisms to assess product reliability [22].

In comparison with PHM, CM is the application of the appropriate sensors (data), analysis (knowledge), and reasoning (context) to estimate the health and track the degradation of equipment [15] and in some cases assessing the remaining useful life.

The ultimate goal of PHM is to determine the RUL of a monitored system. RUL is typically a time, cycle, or mission-based expression, correctly accompanied by uncertainty bounds. Similarly, RUL may be a range of values correctly accompanied by a confidence interval. The RUL predicts a component or system functional/operational usage expectancy based on measured, detected, modeled, and/or predicted health state. The RUL is dependent on the intended set of operating conditions or mission to be performed [15].

2.2.1. SYSTEM DEFINITION

There is a lot of discussion regarding system classification, definition, and what it exactly represents. In the case of electronics, we can establish different levels of system classification as it follows [11]:

- Device Level (die and metalization)
- Component Level (resistor, capacitor, lead frame)
- Board level (circuit board and solder joints)
- Subsystem (Hard Drive, Electronic Unit)
- System
- System of systems

As previously mentioned, this chapter is mainly focusing on the PHM methodology implemented on the subsystem and system level.

2.2.2. STRATEGIES/SCHEMATICS USED IN IMPLEMENTATION

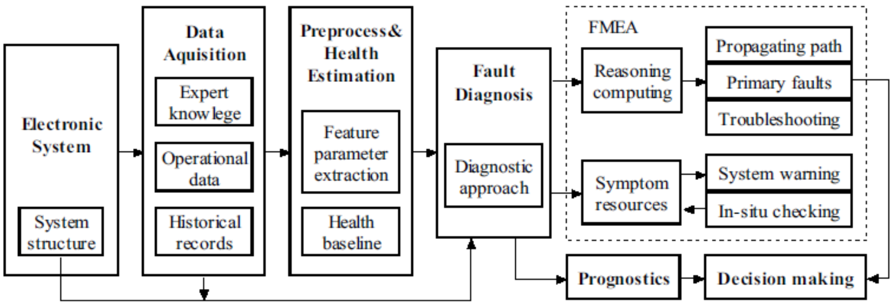

Figure 2.2: Conceptual architecture of PHM-based fault diagnosis for electronics-rich system. [23]

Mishra and Pecht [24] introduced the Life Consumption Method (LCM) for PHM in electronic systems, which uses the environmental loads combined with PoF models to assess the life consumed. Based on the same approach, Zhang et al. [25] developed an enhanced method adding uncertainty adjusted prognostics. Uncertainties are included to capture the fault evolution as a distribution of the predicted RUL.

CALCE PHM Research Center at the University of Maryland used different approaches, including canaries and fuses, precursors feature, and PoF models based on life-cycle loads [11].

Amor-Segan et al. [6] focuses on the automotive industry and proposes a new system-level approach to manage the faults in vehicle networked electronic systems. The framework involves different phases - data collection, data analysis, knowledge discovery, diagnostics, or prognostics leading to corrective and preventative intervention.

Terrissa et al. [26] described PHM architecture into seven layers:

- Data Acquisition
- Data processing
- Condition assessment
- Diagnostic
- Prognostic
- Decision support
- Human machine interface (HMI)

Braden [2], proposed a framework for development stage for validation and testing the automotive electronics. The proposed techniques are providing the estimation of RUL based on real-time monitoring data during reliability testing. In Figure 2.2 a conceptual architecture of PHM is shown, with a focus on diagnostics techniques. Most of the work performed until now reaches different diagnostic stages, implying that the prediction part is not yet mature in electronic systems.

2.3. Sensor and parameter selection

Every PHM system typically collects the data throughout the sensors located strategically and usually measures exterior and interior loading conditions. There are many references regarding sensor and parameter selection for the electronic system, although there are not many examples of such devices used, especially to handle the system level prognostics. According to [27], monitoring the parameters is a fundamental step to assess the health accurately and to predict the remaining useful life. This section is a brief and general introduction to sensors and parameters used for PHM in the electronic system. For More detailed information please check [27].

2.3.1. Sensors used in electronic systems and the parameters related to the sensors

Typical parameters that have the potential to be monitoring devices in a PHM system are showed in Table 2.1.

Domain	Examples
Mechanical	Length, area, volume, velocity or acceleration, mass flow, force, torque, stress, shock, vibration, strain, density, stiffness, strength, angular, direction, pressure, acoustic intensity or power, acoustic spectral distribution
Electrical	Voltage, current, resistance, inductance, capacitance, dielectric constant, charge, polarization, electric field, frequency, power, noise level, impedance
Thermal	Temperature (ranges, cycles, gradients, ramp rates), heat flux, heat dissipation
Chemical	Chemical, species concentration, gradient, reactivity, mess, molecular weight
Humidity	Relative humidity, absolute humidity
Biological	pH, concentration of biological molecules, microorganisms
Electromagnetic radiation and ionizing radiation	Intensity, phase, wavelength (frequency), polarization, reflectance, transmittance, refractive index, distance, exposure dose, dose rate
Magnetic	Magnetic field, flux density, permeability, direction, distance, position, flow

Table 2.1: Examples of parameters for PHM applications. [28]

The sensors suggested above have to be addressed with real-world components that are available in a reasonable size and at a reasonable cost to support use under a cost-benefit analysis [13].

2.3.2. NON-PHYSICAL SOFTWARE PARAMETERS

Except for the physical parameters that can be monitored throughout the electronic system, also software parameters can be monitored and indicate an impending failure of the system. These parameters are, for example, software values concerning the performance and the quality of the service. The System Telemetry Harness proposed by Sun Microsystems [16] uses soft variables (given by the operating system regarding hardware performance) and canary variables (provided by the software such as quality of the service, number of transactions per minute) for estimating the health of the electronics for computer servers.

Even though the physical parameters indicate the system degradation, these non-physical values can link some physical parameters to the actual system performance. A framework is proposed in [6] regarding Electronic Control Unit (ECU) to use ECU hardware and software data to assess the health. It uses ECU parameters such as ECU reset and initialization statistics, ECU error counts, function activation statistics, network status, and performance statistics. Also, FMMEA can indicate software parameters to be monitored such as CPU usage, CPU throttle [22], CPU loading factor [29]. Other examples can be fault codes, scan errors, memory usage capacity, or queue lengths.

2

2.4. An overview of Data-driven approaches

From the electronic systems perspective, diagnostics refers to the ability to identify deviation from its typical operational profile as well as to detect, isolate and diagnose electrical faults [3]. Data-driven approaches, also called model-free, rely on observation data without a priori knowledge about the system [30] and according to [31] they are also called a black box. In this section, techniques used in data-driven approaches for the electronic system are presented. Usually, it refers to fault detection, diagnostics, and prediction. In most cases, the first two parts are handled with Data-driven approaches. The prediction part can also be obtained from PoF.

Distance Metric	Machine Learning	Statistical	Neural Computation	Stochastic
Euclidean	Fuzzy Logic	Bayesian Methods	Artificial Neural Networks	Markov chain
Mahalanobis	Support Vector Machine	Principal Component Analysis	Deep Learning	Monte Carlo
Bayesian	Kalman Filter	Regression Analysis	Self Organizing Maps	Wiener Process
K-nearest Neighbour	Particle Filter			Gamma Process

Table 2.2: Data-driven techniques.

In Table 2.2, a selection of representative methods used in prognostics is shown. These methods are used or have the potential to be used in all necessary steps in prognostics. Improvements of all these methods implemented for different purposes are found in the literature. Also, there are many other techniques in other fields, which can be transferred to the electronic systems to improve predictive requirements.

2.4.1. Fault detection

Fault detection, also found as anomaly detection in the literature, is a fundamental requirement for prognostics. The method should be accurate enough that the false alarm rate is close to zero. So far, the distance metric techniques have been shown the most effective in fault detection. Also, fault detection can use methods like one-class Support Vector Machine and Fuzzy Logic.

Canary devices mounted on the actual product can also provide a warning of failure due to specific wear-out failure mechanisms. The time to failure of these prognostic cells can be pre-calibrated for the time to fail the actual product. The stresses experienced by the product are applied to these cells as well. The canaries can be calibrated to provide sufficient warning of failure to enable appropriate maintenance, and replacement activities [32].

2.4.2. Fault Diagnostics

Diagnostics monitors determine the current state of health of a system and determine potential problems [16]. Also, [26] diagnostic determines if the health of the system has degraded, suggests fault possibilities, and identifies the component that has ceased to operate. For electronic systems, diagnostics refers to the ability to recognize deviation from its typical operational profile as well as detect, isolate and diagnose electrical faults

[3]. The first efforts in diagnostic health monitoring of electronics involved using a built-in test (BIT), defined as an onboard hardware-software diagnostic device to identify and locate faults. It is used as a diagnostic tool, although it has a significant rate of false alarms [32].

Diagnostic parameters and measures can be generated using the time series [33], Bayesian network approach [23], an advanced remote intelligent diagnostic support system (RIDES) [34], self-diagnostic Automatic Test Equipment (ATE) [8], etc.

FAULT ISOLATION

This concept is typically used in systems, where data detected as faulty should indicate from which component or subsystem the faulty signal is coming from. In the literature, this is presented mainly as a concept, and there were no relevant examples in the electronic system where techniques or methods are used to isolate the fault.

FAULT IDENTIFICATION

It is the process of identifying the cause of a failure at various points in a system. Fault identification is the key concept of diagnostics. Recently, classification methods were used to mitigate the fault identification such as machine learning techniques [35], [36]. For example :

- Random Forrest - is an ensemble classifier that consists of many decision trees and outputs the class that is the mode of the classes output by individual trees

- Voting - Given a class of learned models, voting or majority response could be used to determine the response of the overall PHM system.

- Support Vector Machine - It is based on the boundary optimization problem of an already known failure data

2.4.3. FAULT PREDICTION

The data-driven approach can realize predictions for RUL through statistical and probabilistic methods [5]. Models built for prognostics are focused on building computation models that learn a specific or holistic behavior of the system based on empirical sensor data. Examples of data-driven techniques used for fault prediction [37] are:

- Ensemble Learning - such methods use multiple models to obtain better predictive performance

- Neural Networks - This creates a linear RUL model based on the historical sensor data of the system till failure

- Stochastic - These methods employ probabilistic methods to handle system-level prognostics

Prognostics is possible for system modeling through Markov chains, stochastic methods, and time series analysis, considering Shannon's principle, which states that the physical processes in the past will remain in the future.

2

2.4.4. CASE STUDIES

Lopez et al. [16] used Sequential Probability Ratio Test (SPRT) and the Multivariate State Estimation Technique (MSET) for computer servers soft variables, canary variables, and physical variables to implement prognostics. Also, Urmanov [31] uses an approach to implement prognostics for computer servers. He added empiric models such as the Wiener process with a drift in the process.

A unique hybrid prognostics and health management methodology combining both data-driven and physics-of-failure models are proposed in [22] for fault diagnostics and life prediction of a computer system. First, an FMMEA was conducted, and parameters as fan speed, CPU temperature, motherboard temperature, video card temperature, %CPU usage, and %CPU throttle were established to be monitored. Fault detection was performed using Mahalanobis Distance (MD), and a Projection pursuit analysis was performed to show which variables vary the most. These parameters can be matched to a PoF damage model to assess the damage.

In [38] it is described the nonlinear Wiener process with a time drift for degradation process and the Proportional hazard model for RUL. Also, methods such Gamma process and continuous-time Markov chain can be used for the degradation process.

In [39] failure prognostics of an electronic system is performed by Fast Relevant Vector Machine based on Fruit Fly Optimization Algorithm. It does not provide a concrete example, and the procedure is a general approach.

Hirohata et al. [29], monitors the cooling performance degradation and load history of a Printed Circuit Board (PCB) in digital equipment. A hierarchical Bayes model based on Computer-aided Engineering results of thermal stress simulation and experiment data from actual measurements is used. The case study is a notebook PC on which the temperature and deformation distribution from monitoring variables using the Bayes model can be estimated. Based on the monitored data such as device load factor and revolution number of a cooling fan, it can calculate the temperature and the deformation distribution of the PCB. The FEM simulation provides this linking parameter, such as thermal dissipation of the device and thermal boundary condition using the hierarchical Bayes model. Health Distance was developed between two signals D1 and D2, as a shift on an angle. This angle is computed as the inverse of cosinus between the sum of all dot product and the product of each euclidean norm of D1 and D2. When the angle is 0, the signals are the same, and when the angle is pi, the signals are different.

In [30] an improved approach was presented that makes it possible to extract and analyze the power systems eigenvalues, which are related to the frequency of the power system that determines correlations between extracted features and state of health. The goal is to provide correlation information such as SOH using pattern analysis with real-time data from a non-intrusive smart power sensor. The test vehicle represents the electronic power systems (e.g., switched-mode power supply).

A data-driven approach presented in [33] is applied to electronic systems and uses methods such as pattern recognition (SVMR), signal processing, and Markov chain techniques. In [33] it is stated that building analytical models for even rudimentary onboard systems from the component models is virtually impossible due to the high level of complexity and non-linearity. The methodology consists of four main stages: (1) Mahalanobis Distance to generate healthy baseline, (2) Noise suppression and conversion to generate symbolic time-series, (3) A Markov state model, and (4) Diagnostic and prognostic parameters and measures to be generated using the time series and neural network techniques. A wavelet transformation was performed on an MD time series to remove noise from the signal and extract features from the data. This data was partitioned into eight regions, each being represented by a symbol. Based on this, a Markov state model is generated to provide the parameters and measures for health condition monitoring and prognostics.

In [23], a Diagnostic Bayesian network based on PHM is proposed to perform available and efficient fault diagnostics for the electronic system. The numerical data is gathered based on a set of radar indicators on the avionics system. The algorithm uses the Bayesian approach. The basic idea is a formula used to calculate the conditional probability of fault B occurring when a fault symptom A appears. The monitored data is voltage or current, and it is used to define the fault symptoms.

Jin et al. [8], proposes a model to monitor the degradation of electronic equipment and further predict the RUL based on the self-diagnostic data. The degradation precursor, characterized by voltage or current signals, is modeled as a Non-stationary Gaussian process with time-varying mean and variance. The algorithm is periodically executed to collect the system health information using voltage and current signals as failure precursors for the healthy index. This model is based on a Statistical signal degradation based on the shift of the mean or the change of the variance.

Lall et al [35][36] uses different data-driven techniques. In [35] prognostic framework for electronic systems has been developed with neural network-based self-organizing maps with multiple failure modes. Unsupervised learning of the neural net has been used to train the neural net to identify individual failure modes. Transient strain is measured during the drop-event by digital image correlation. In addition, FEM models are constructed to which different failure modes are imposed. A prognostic framework is studied with neural network self-organizing maps. The Artificial Neural Network approach conducts Fault-mode isolation and mode classification. The test vehicles are two PCBs test boards of JEDEC Standard.

In [36] a new technique has been developed for health monitoring and failure mode classification based on measured damage precursors. The Karhunen Loeve Transform has been used to reduce and decorrelate the feature vectors for fault mode classification in electronic assemblies. Euclidean, Mahalanobis, and Bayesian distance classifiers based on joint-time frequency analysis have been used to classify the resulting feature space. The system approach determines throughout the drop-test all the failure modes such as solder inter-connect failure, inter-connect missing, chip delamination, or chip cracking in packaging architectures. The monitored parameters are the transient strains recorded during the drop-event using digital image correlation. The test vehicles are two PCBs with various components mounted on them. A feature vector is created by analyzing the transient strain signal with the time-frequency technique. Karhunen Loeve Transforms is used to decorrelate the feature space of damage progression. The same failure modes are simulated with explicit FEM, and the same transient strain data is extracted. On the decorrelated feature space containing data from both experiments and simulation, dominant directions are extracted with MD and PCA to represent each failure mode. Doing so, a clustering of the failure data is made.

A method based on the simulation-before-test (SBT) technique to quantitatively assess the health of an electronic system is presented in [40]. The case study is an analog state-variable filter circuit. A circuit-centric approach assessing the health of an electronic system is highlighted, enabling an electronic system to be decomposed into individual critical circuits from which local results can be merged to obtain a system-level health indication. Thus, by monitoring few nodes within the circuit and estimating and combining HIs for the critical circuits, one could get a health indicator for the whole system. The proposed approach involves three stages: system decomposition, offline testing, and online testing. The offline testing is mainly represented by simulations-before-test to understand the circuit behavior under healthy and failure conditions. Hence various faults are seeded into critical components. To assess the health, an index of +1 healthy and -1 faulty is considered. A function is used to evaluate the state between these two values. This function is the same as in the case of SVM and LS-SVM. Another circuit-centric example is also presented in [41].

An example of applying PHM at the design stage to enhance reliability is presented in [4]. It introduces failure precursors and investigates their impact on real product failure to improve the accuracy of reliability prediction in the design phase. Hard disk drives are selected as a case study. A failure precursor is used, such as scan error from Self-Monitoring Analysis and Reporting Technology (SMART) which can be caused by bad sectors (damage on hard drive sectors) on hard disk or malfunction of the magnetic head. These failure precursors are selected, and their statistical distribution of time-to-failure-precursor is obtained. The calculation shows that mean-time-to-failure for drives with failure precursors is 49 times shorter than mean-time-to-failure for a drive with no failure precursors. Also, it indicates that PHM applied at three months, six months, and one year of operational hours have different results in RUL calculations. The one calculated at one year is getting more closer to the actual drive failure occurrence.

Niu et al. [42] presents a novel approach for health monitoring of electronic products using MD and Weibull distribution. The MD value is used as a health index, and the Weibull distribution is used to determine health decision metrics. A case study of a notebook computer health monitoring system is carried out. First, FMMEA is used to select effective performance parameters, and then a normalization process is performed on the data. The failure mode contains the fan's rotation failures, head crashes in the hard disk drive, and electrical short on the memory card with the corresponding measurable variables, such as the fan's temperature, hard disk drive, and memory usage capacity. The scale parameters are extracted from the distribution. Additionally, the distribution and the mean are calculated. Weibull distribution is used because not always MD values follow a Gaussian distribution.

2.5. AN OVERVIEW OF MODEL-DRIVEN APPROACHES

Data-driven approaches can be very effective for electronic systems, considering that realizing complex physical models for the system is problematic. However, in most cases, the parameters monitored have no connections to the actual fault/failure. This fact is demanding for a method to link the real failure with the monitored parameters. Using physical models can easily make this link and have the benefit of being more accurate.

2

2.5.1. PoF DESCRIPTION AND FMMEA

The PoF approach utilizes knowledge of a system's life cycle loading conditions, geometry, and material properties to identify potential failure mechanisms and estimate RUL [32]. A prognostic feature or failure precursor provides an advanced warning of impending failure that, in turn, may predict RUL. Essential to any predictive system is the careful selection of prognostic product features that correlate damage accumulation with known failure modes [2]. The PoF approach includes several steps, mainly FMMEA, feature extraction, and RUL estimation. Further, failure models or graph-based models are not suitable for detecting intermittent system behavior as they are modeled for specific degradation mechanisms. Sudden changes in system parameters that characterize intermittent fault are not accounted for in these models [20]. The model-based approach uses prior knowledge of the system to develop mathematical models to process and evaluate the current data [30]. These mathematical representations incorporate a physical understanding of the system and include both system modeling and PoF modeling. RUL is carried out based on knowledge of the processes causing degradation and leading to failure of the system. In the system modeling approach, mathematical functions or mappings, such as differential equations represent the system. Statistical estimation techniques based on residuals are then used to detect, isolate and predict degradation [20]. PoF approaches to model electronic system reliability have shown that time-to-failure for electronic parts and interconnects can be predicted within quantifiable bounds of uncertainty. [17]

Failure Mechanisms	Failure sites	Relevant loads
Fatigue	Wire-bond,solder leads, bond pads, traces, vias, interfaaces	ΔT,$Tmean$,dT/dt,dwell time,ΔH,ΔV
Corrosion	Metalization	M,ΔV,T
Electro-mitigation	Metalization	T,J
Conductive filament formation	Between metalization	M,∇V
Stress-driven diffusion voiding	Metal traces	s,T
Time-dependent dielectric breakdown	Dielectric layers	V,T

Table 2.3: Standard failure mechanisms in electronic systems. [23], [43]

where: Δ: Cyclic range; ∇: Gradient; V: Voltage; T: Temperature; M: Moisture; J: Current density; s: Stress, H: Humidity.

2.5.2. MODELS USED

There are several mathematical techniques that can provide prognostics measures for electronic systems. PoF models used in electronics:

- Fatigue - Coffin - Manson, Merkle
- Corrosion - Howard
- Electromitigation - Black
- Conductive filament formation - Rudra

- Stress driven diffusion voiding - Okabayashi
- time dependent dielectric breakdown - Fowler - Nordheim

According to [3], there are four main models used in PHM such as:

- Statistical reliability-based approaches. Developed for non-critical systems. Weibull distribution is the most used method.
- Life cycle load-based approaches. Damage accumulation models based on environmental data are used.
- State estimation-based approaches. It can track the gradual degradation of the system.
- Feature extraction-based approaches. Feature extracted from the monitored data.

These models used in electronics are primarily suitable for components because they do not consider the interactions between components in a system. A much better approach for models can represent the adoption of FEM, reduction techniques for FEM, metamodels, or surrogate models to reproduce the entire system behavior.

2.5.3. CASE STUDIES

Gu et al. [44] proposed Life Cycle Monitoring (LCM) to be applied to an electronic component-board assembly placed under the hood of an automobile and subjected to normal driving conditions in the Washington DC area. Solder joint fatigue was identified as the dominant failure mechanism. Vibrations were measured in-situ and used to estimate the LCM using the environmental data. Then, acceleration data recorded from vibration loading was analyzed for remaining-life prediction.

Zhang et al. [25], used PoF to calculate the RUL of a PCB with different Ball Grid Array packages mounted on it. They used daisy chain resistance as monitoring parameters input for LCM and Uncertainty Adjusted Prognostics methods.

Gu and Pecht [11] analyzed the electronic products with FMMEA, and they developed a predictive approach to estimate the remaining useful life using PCB strain data. Prognostics were performed by using the stress data extracted at the component solder joint.

Fault mode effect analysis (FMEA) is applied in [45], identifying the root cause of failure, probability of occurrence, and system-level effects on a GPS. Failure criteria are the deviation in primary feature value by 30dB below the initial value. A prognostic feature provides an advanced warning of impending failure to predict RUL.

In [19] prognostics methods are applied to a Line Replaceable Unit (LRU). This can be an engine controller for a jet engine. Discrete event simulation is used to follow the life of individual socket instances from the start of their field life to the end of their operation and support. This can be an alternative for continuous monitoring. The input for such a simulation model is a stochastic analysis based on a Monte Carlo simulation.

Pecht et al. [20] proposed an FMMEA analysis, which determined the critical modes and mechanisms affecting the assembly due to the thermal cycling resulting in an open circuit. Temperature and resistance were found to be essential to detect system failure for the given loading conditions. FMMEA can be used for PHM for electronic systems because it can track all the failure modes and mechanisms in a system on a given loading condition. The anomaly detection was performed using a data-driven residual analysis technique, and the healthy baseline creation was based on ten-cycle data. A regression model was created based on component resistance in the function of temperature. The residual between the model and the observed data was used for the SPRT algorithm to detect anomalies. SPRT is a statistical likelihood ratio test for anomaly detection. When an anomaly is detected, the parameters causing the anomaly are identified and then used in physics-based models. For example, in this case, what was causing the anomaly is the resistance change due to thermal fatigue was identified. Hence a Coffin-Manson model was used to calculate RUL. This approach is also capable of detecting intermittent failures.

Ramakrishnan and Pecht [46] used PoF based prognostics to assess the RUL of an electronic component board placed under the hood of an automobile and subjected to normal driving conditions. The test board incorporated surface-mount leadless inductors soldered onto an FR-4 substrate using eutectic tin-lead solder. Temperature and vibration were measured in situ on the board in the application environment. Using the monitored environmental data, stress and damage models were successfully used to estimate consumed life.

The uncertainties in prognostics have an effect on its applicability and the quality of prognostics results. The Monte Carlo method is the most common method for uncertainty analysis. In [47] the prognostics uncertainty analysis method based on the stochastic response surface method has been proposed. The case study is a board-level electronic product of a strain tester (it measures resistance strain test signal). The SRSM constructs the response surface based on the Hermite polynomial to approximate the random response function, guaranteeing the convergence in probability. Here, the PoF-based method is used to calculate the RUL of the electronic products. A solder fatigue model such as Coffin-Manson, plate through hole thermal fatigue model (PTH), electro-mitigation model (Black) is chosen. A predictive linear cumulative damage model and failure mechanism competition model are constructed to deal with different failure mechanisms.

In [48] the case study is a laptop computer by implementing FMMEA using software called MADe. FMMEA is applied to divide the system into subsystems. However, the software does not include all the possible mechanisms that may occur in assemblies. This software can model the entire system and identify the failure mechanisms in the selected subsystems.

2.6. SUMMARY AND RECOMMENDATION

The existing PHM examples are usually using the current and voltage of the systems as monitoring parameters. It would be more desired if parameters representing the actual physical quantities linked to failures could be identified. This would require the development of new sensors as well as new PHM strategies. Based on the literature reviewed in this chapter, it can be stated that the data-driven approaches are more suitable for system monitoring since the physical models are usually developed to analyze components or failure mechanisms. Regarding model-driven procedures, efficient model reduction techniques and advanced statistical uncertainty propagation techniques would be needed to be able to tackle complicated and expensive system modules. The concept of surrogate models can be combined with simulation models to alleviate the burden of computational cost. Further advances are expected to be added to PHM applied to electronic systems.

2

Conceptual	Technical	Economical
Systems Complexity	System design	Warranty issues
Time to market, size, and cost	Precursor selection	PHM Benefits in product value
Higher loads, longer functionality time	Intermittent Failures	Development Extra Cost
Maintenance Culture	System Physical Models	

Table 2.4: Challenges in PHM for Electronic Systems.

2.7. CONCLUSIONS

Prognostics and Health Monitoring for electronic systems is not a mature subject and requires further work to be performed in several areas. The most important tasks involve developing sensors and their location throughout the system, transferring data-driven techniques already developed for different PHM applications to electronic systems. It would be interesting if, in the context of Big data/Deep Learning, just one algorithm could be used to reach all the levels of prognostics based on the input size and quality. This could simplify all the necessary methods to be used in a chain and be very costly computationally. Nevertheless, the current advancement in Artificial Intelligence techniques will play a vital role in the next generations of PHM systems in any field. The fusion between data-driven approaches and model-driven approaches is vital in the performance of the PHM system.

The future trend should be focused on developing smart electronic components with embedded sensors, which contain sensing cells and the logic part in the system-on-chip and have wireless communication and ultra-low power consumption.

Methods	Parameters	Test Vehicle	Ref
Mahalanobis Distance - Healthy Baseline; Noise suppression, time series, signal processing - Data Handling; Markov state Model - Generating prognostics parameters	System Specs usage, Environmental Loads, Fan Speed, CPU Usage, Temperature	Personal Computers	[33]
Mahalanobis Distance - Healthy Index, Weibull Distribution	Memory Usage Capacity, Temperature of the fan, Hard Disk Drive	Notebook Computers	[42]
Reliability Mean-Time-to-Failure	Scan error	Hard Disk Drive	[4]
Support Vector Machine, Least Square - Support Vector Machine	Resistance and Capacitance	Analog State Variable Filter Circuit	[40]
Karhunen Loeve Transform, Euclidean, Mahalanobis and Bayesian Distance, Finite Element Methods, Principal Component Analysis, Neural Networks, Self-Organizing Maps	Transient Strains	PCB	[36], [35]
Empirical Methods, Multivariate State Estimation Technique, Sequential Probability Ratio Test	Temperatures, Humidity, Vibration, Voltages, Current, CPU and Memory Loads, Fan Speed, Queue Lengths	Computer Servers	[31], [16]
Physics-of-Failure	Temperatures, Humidity, Vibration, Voltages, Current, Power	PCB	[46]
Non-Stationary Gaussian - Analytical Model	Voltages, Current		[8]
Bayesian Network - Fault Identification	Voltages, Current		[23]
Mean-Time-between-Failures, State of Health	Voltages	Power Supply	[30]
Hierarchical Bayes Model, Finite Element Methods	CPU Loading Factor, Fan Rotation Speed	Note PC	[29]
Life Consumption Methods, Physics-of-Failure	Acceleration Data	PCB, Line Replaceable Units	[44],[19]
Physics-of-Failure	Signal Strength	RF system, GPS	[45]
Life Consumption Method, Uncertainty Adjusted Prognostics Fusion	Resistance	PCB	[25]
Failure Modes and Mechanisms Effect Analysis Software	The software identifies the parameters.	Laptop	[48]
Markov Theory, Stochastic prediction model	Thermal failure rate, Repair rates, Mean time between thermal failures	DC frequency Conversion conditioning	[49]
Ferni-Dirac Health description, Quantum mechanics analogy, Back-propagation Neural Network remaining useful life model	Voltage	PCB Power Conversion Board	[50]
Finite Element Methods, Mahalanobis Distance, Singular Value Decomposition, Support Vector Machine	Mechanical Stresses	Outer Molded Electronic Control Unit	[12]

Table 2.5: Case Studies.

REFERENCES

[1] A. Prisacaru, P. J. Gromala, M. B. Jeronimo, Bongtae Han, and Guo Qi Zhang, *Prognostics and health monitoring of electronic system: A review,* in *2017 18th International Conference on Thermal, Mechanical and Multi-Physics Simulation and Experiments in Microelectronics and Microsystems (EuroSimE)* (2017) pp. 1–11.

[2] D. R. Braden and D. M. Harvey, *A prognostic and data fusion based approach to validating automotive electronics,* .

[3] S. Kumar and M. Pecht, *Modeling approaches for prognostics and health management of electronics,* **6**, 467.

[4] Y. Chien, Y.-X. Huang, and J. Y.-C. Wang, *Prognostics based design for reliability technique for electronic product design,* in *Proceedings of the Institute of Industrial Engineers Asian Conference 2013*, edited by Y.-K. Lin, Y.-C. Tsao, and S.-W. Lin (Springer Singapore) pp. 1343–1351.

[5] M. Ahsan, S. Stoyanov, and C. Bailey, *Prognostics of automotive electronics with data driven approach: A review,* in *Electronics Technology (ISSE), 2016 39th International Spring Seminar on* (IEEE) pp. 279–284.

[6] M. Amor-Segan and R. P. Jones, *A framework for health monitoring of automotive electrical and electronic control systems (poster),* in *Vehicular Networking Conference (VNC), 2011 IEEE* (IEEE) pp. 177–184.

[7] N. M. Vichare and M. G. Pecht, *Prognostics and health management of electronics,* **29**, 222.

[8] T. Jin, P. Wang, and Q. Sun, *Reliability prognostics for electronics via built-in diagnostic tools,* in *Reliability and Maintainability Symposium (RAMS), 2011 Proceedings-Annual* (IEEE) pp. 1–7.

[9] *Collection of papers presented at the 12th international workshop on thermal investigation of ICs and systems: Nice, cote d'azur, france, 27 - 29 september 2006,* OCLC: 255790607.

[10] S. Mathew, M. Osterman, and M. Pecht, *Considerations in implementing canary based prognostics,* in *Prognostics and Health Management (PHM), 2015 IEEE Conference on* (IEEE) pp. 1–7.

[11] J. Gu, N. Vichare, T. Tracy, and M. Pocht, *Prognostics implementation methods for electronics,* in *Reliability and Maintainability Symposium, 2007. RAMS'07. Annual* (IEEE) pp. 101–106.

[12] A. Palczynska, A. Prisacaru, P. J. Gromala, B. Han, D. Mayer, and T. Melz, *Towards prognostics and health monitoring: The potential of fault detection by piezoresistive silicon stress sensor,* in *2016 17th International Conference on Thermal, Mechanical and Multi-Physics Simulation and Experiments in Microelectronics and Microsystems (EuroSimE)* (IEEE) pp. 1–8.

[13] D. Droste and K. Finklea, *Prognostics for electronic systems,* in *2006 IEEE Autotestcon* (IEEE) pp. 181–186.

[14] Y. G. Bagul, I. Zeid, and S. V. Kamarthi, *A framework for prognostics and health management of electronic systems,* in *2008 IEEE Aerospace Conference*, pp. 1–9.

[15] P. W. Kalgren, C. S. Byington, M. J. Roemer, and M. J. Watson, *Defining PHM, a lexical evolution of maintenance and logistics,* in *2006 IEEE Autotestcon* (IEEE) pp. 353–358.

[16] L. Lopez, *Advanced electronic prognostics through system telemetry and pattern recognition methods,* **47**, 1865.

[17] M. Pecht, T. Shibutani, M. Kang, M. Hodkiewicz, and E. Cripps, *A fusion prognostics-based qualification test methodology for microelectronic products,* 10.1016/j.microrel.2016.04.002.

[18] S. Mathew, D. Das, R. Rossenberger, and M. Pecht, *Failure mechanisms based prognostics,* in *International Conference on Prognostics and Health Management, 2008. PHM 2008*, pp. 1–6.

[19] P. A. Sandborn and C. Wilkinson, *A maintenance planning and business case development model for the application of prognostics and health management (PHM) to electronic systems,* **47**, 1889.

[20] M. Pecht and R. Jaai, *A prognostics and health management roadmap for information and electronics-rich systems,* **50**, 317.

[21] P. W. Kalgren, M. Baybutt, A. Ginart, C. Minnella, M. J. Roemer, and T. Dabney, *Application of prognostic health management in digital electronic systems,* in *Aerospace Conference, 2007 IEEE* (IEEE) pp. 1–9.

[22] Sachin Kumar, M. Torres, Y. C. Chan, and M. Pecht, *A hybrid prognostics methodology for electronic products,* (IEEE) pp. 3479–3485.

[23] L. Xu and M. Xu, *PHM-based fault identification for electronics-rich systems under uncertainty,* in *Proceedings of the Sixth International Conference on Management Science and Engineering Management*, Vol. 185, edited by J. Xu, M. Yasinzai, and B. Lev (Springer London) pp. 209–218.

[24] S. Mishra, S. Ganesan, M. Pecht, and J. Xie, *Life consumption monitoring for electronics prognostics,* in *Aerospace Conference, 2004. Proceedings. 2004 IEEE*, Vol. 5 (IEEE) pp. 3455–3467.

[25] G. Zhang, C. Kwan, R. Xu, N. Vichare, and M. Pecht, *An enhanced prognostic model for intermittent failures in digital electronics,* in *2007 IEEE Aerospace Conference* (IEEE) pp. 1–8.

[26] L. S. Terrissa, S. Meraghni, Z. Bouzidi, and N. Zerhouni, *A new approach of PHM as a service in cloud computing,* in *Information Science and Technology (CiSt), 2016 4th IEEE International Colloquium on* (IEEE) pp. 610–614.

[27] S. Cheng, M. Azarian, and M. Pecht, *Sensor system selection for prognostics and health monitoring,* in *ASME 2008 International Design Engineering Technical Conferences and Computers and Information in Engineering Conference* (American Society of Mechanical Engineers) pp. 1383–1389.

2

[28] S. Cheng, M. H. Azarian, and M. G. Pecht, *Sensor systems for prognostics and health management,* **10**, 5774 ().

[29] K. Hirohata, K. Hisano, Y. Hisakuni, T. Omori, and M. Mukai, *Health monitoring method for load assessment and cooling performance degradation of printed circuit boards,* in *ASME 2010 International Mechanical Engineering Congress and Exposition* (American Society of Mechanical Engineers) pp. 469–478.

[30] B. U. Kim, C. Lynn, N. Kunst, and T. Dudgeon, *Pattern analysis in real time with smart power sensor,* in *Aerospace Conference, 2010 IEEE* (IEEE) pp. 1–8.

[31] A. Urmanov, *Electronic prognostics for computer servers,* in *2007 Annual Reliability and Maintainability Symposium* (IEEE) pp. 65–70.

[32] N. Vichare, B. Tuchband, and M. Pecht, *Prognostics and health monitoring of electronics,* in *Handbook of Performability Engineering* (Springer) pp. 1107–1122.

[33] C. Sankavaram, B. Pattipati, A. Kodali, K. Pattipati, M. Azam, S. Kumar, and M. Pecht, *Model-based and data-driven prognosis of automotive and electronic systems,* in *2009 IEEE International Conference on Automation Science and Engineering* (IEEE) pp. 96–101.

[34] M. Stora and P. Kalgren, *Remote intelligent diagnostics for electronic systems (RIDES),* in *2009 IEEE AUTOTESTCON* (IEEE) pp. 11–16.

[35] P. Lall, P. Gupta, and D. Panchagade, *Self-organized mapping of failure modes in portable electronics subjected to drop and shock,* in *2010 Proceedings 60th Electronic Components and Technology Conference (ECTC)* (IEEE) pp. 1195–1208.

[36] P. Lall, P. Gupta, and A. Angral, *Anomaly detection and fault-mode isolation for prognostics health monitoring of electronics subjected to drop and shock,* in *Thermal, Mechanical & Multi-Physics Simulation, and Experiments in Microelectronics and Microsystems (EuroSimE), 2010 11th International Conference on* (IEEE) pp. 1–14.

[37] S. Das, *An efficient way to enable prognostics in an onboard system,* in *2015 IEEE Aerospace Conference* (IEEE) pp. 1–7.

[38] S. Zhao, V. Makis, S. Chen, and Y. Li, *On-line reliability assessment for an electronic system subject to condition monitoring,* in *Prognostics and Health Management (ICPHM), 2016 IEEE International Conference on* (IEEE) pp. 1–6.

[39] K. Wu, J. Kang, and X. Wang, *Research on failure prognostics method of electronic system based on improved fruit fly algorithm and grey fast relevance vector machine,* (IEEE) pp. 94–98.

[40] A. S. S. Vasan, M. Pecht, and B. Long, *Health assessment of electronic systems,* (IEEE) pp. 1689–1694.

[41] M. Yin, X. Ye, and Y. Tian, *Research of fault prognostic based on LSSVM for electronic equipment,* in *Prognostics and System Health Management Conference (PHM), 2015* (IEEE) pp. 1–5.

[42] G. Niu, S. Singh, S. W. Holland, and M. Pecht, *Health monitoring of electronic products based on mahalanobis distance and weibull decision metrics,* **51**, 279.

[43] M. Pecht and Jie Gu, *Physics-of-failure-based prognostics for electronic products,* **31**, 309.

[44] J. Gu, D. Barker, and M. Pecht, *Prognostics implementation of electronics under vibration loading,* **47**, 1849 ().

[45] D. Brown and P. Kalgren, *Electronic prognostics - a case study using global positioning system (GPS),* (IEEE) pp. 832–838.

[46] A. Ramakrishnan and M. Pecht, *A life consumption monitoring methodology for electronic systems,* in *2003 IEEETransactions on Components and Packaging Technologies* (IEEE).

[47] W. Pan, Z. Wang, and B. Sun, *Comparison of stochastic response surface method and monte carlo method for uncertainty analysis of electronics prognostics,* in *Prognostics and Health Management (PHM), 2015 IEEE Conference on* (IEEE) pp. 1–7.

[48] S. Menon, C. Stecki, J. Song, and M. Pecht, *Optimization of PHM system for electronic assemblies using maintenance aware design environment software,* in *Australian International Aerospace Congress*.

[49] Y. Wan, H. Huang, D. Das, and M. Pecht, *Thermal reliability prediction and analysis for high-density electronic systems based on the markov process,* **56**, 182.

[50] Y. Cui, J. Shi, and Z. Wang, *Quantum assimilation based state-of-health assessment and remaining useful life estimation for electronic systems,* , 1.

2

3

On the Accuracy of CMOS-based Piezoresistive Stress Sensor: Theoretical Review and Experimental Validation

The measurement uncertainties of the CMOS-based stress sensor are studied. After the sensor fundamentals are reviewed, the random uncertainties associated with the data acquisition unit are evaluated by measuring raw current signals from uniquely fabricated free-standing stress sensor chips. The free-standing sensor chips are tested further for systematic uncertainties associated with the manufacturing-induced residual stresses by subjecting them to a thermal cycle. By incorporating the quantified uncertainties, the stress measurement accuracy of the sensor chip under an in-situ loading is finally quantified by a numerical model verified by a sub-micron sensitivity optical technique.

3.1. Introduction

The piezoresistive stress sensors were developed to measure directly the stresses of a silicon chip embedded in a package. The concept of a resistance-based sensor was first introduced in 1961 [2], and later it was implemented for packaging applications [3],[4]. The resistance-based sensors are typically fabricated on a relatively large scale ($\approx 300\mu m$ by $300\mu m$). The measured stress value represents average stress over the sensor area, making quantitative measurements of critical stresses challenging. In addition, the resistive stress sensors require a reference measurement for a stress-free state. These

Parts of this chapter have been published in IEEE Sensors Journal [1] (2019)

reference measurements have to be repeated at all temperatures of interest [4], which implements manufacturing problems impractical.

The CMOS (Complementary Metal-Oxide Semiconductor) based sensor was developed to cope with the limitations of the resistance-based sensor [5]. It can be fabricated on a much smaller scale (a typical single measurement cell of 50 μm x 50 μm), enabling the sensor to detect a local stress concentration. The calibration is no longer required for the CMOS-based sensor by placing transistors in a current mirror configuration. Additional benefits include: (1) the measurement system becomes much more straightforward as the output signal is an electric current that can be measured directly; (2) it is easy to integrate the sensor with active circuitries; (3) multiplexers are readily implementable, which allows simultaneous data acquisition from all measurement cells; and (4) the sensitivity is enhanced because lightly doped silicon is used to fabricate the sensor.

Various research groups implemented the CMOS-based sensor, most notably, by Jaeger et al. [6],[7],[8]. They analyzed the behavior of the CMOS stress sensor in various measurement circuits. They selected a cascade current mirror configuration to investigate the effect of the encapsulation process on the package stress. A research group of Freiburg University IMTEK designed a CMOS-based stress sensor, which used the pseudo hall effect in silicon. They characterized the sensor [9], [10], created the matrix of cells with active circuitries [11],[12],[13], and utilized it to monitor the wire bonding process [14],[15].

More recently, the sensor was considered for prognostics and health management (PHM). In Refs. [16],[17],[18], Roberts et al. studied the evolution of stresses during packaging processes and thermal cycling reliability testing using a resistive type of stress sensor. They found that the stress changed rapidly at the beginning of cycling but had only small changes afterward. In Ref. [19], Rahim et al. showed the changes in stress sensor signal caused by delamination and warpage failure. Similar results during thermal cycling were presented by Shindler-Saefkow et al. [20], and Yu-Yao Chang et al. [21],[22]. In Ref. [23],[24], Lall et al. observed the changes in stresses measured by the sensor before delamination occurred, which was identified as a possible leading indicator of failure. In Ref. [25],[26],[27],[28],[29],[30], various prognostics attempts were made using the sensor, including the internal stress measurement of molded electronic control units and the in-situ failure or fault detection.

Some considerations about the measurement accuracy of the resistance-based sensor, associated with calibration errors and rosette alignment errors, can be found in the literature [3],[31]. Still, only limited information is available for the accuracy of the CMOS-based sensor. To extend its applicability further into actual applications in the PHM domain, it is imperative to assess quantitatively the uncertainties associated with the stress measurements using the advanced CMOS-based sensor. This is the motivation of the chapter. The objective of this chapter is, thus, to quantify the measurement uncertainties of the advanced CMOS-based stress sensor and to provide the engineering guidelines for PHM applications. The fundamentals of the CMOS-based sensor are reviewed in Section 3.2. The sensor chip and the data acquisition unit are described in Section 3.3. The uncertainties of the stresses of free-standing sensors are discussed in Section 3.4. In Section 3.5, a uniquely verified predictive numerical model is used to evaluate the measurement accuracy of the stresses of the sensor chip mounted on a ceramic substrate that is subjected to a thermal excursion.

3.2. FUNDAMENTALS OF CMOS-BASED STRESS SENSOR

Let us consider a coordination system shown in Figure 4.1, where the x and y axes are aligned with [110] and [$\bar{1}$00] crystallographic axes of silicon, respectively. The resistivity in the directions shown in Figure 4.1 can be described by the following set of equations [4]:

$$\left.\frac{\Delta\rho}{\rho}\right|_{0°} = \frac{\pi_S^p}{2}(\sigma_{11}+\sigma_{22}) + \frac{\pi_{44}^p}{2}(\sigma_{11}-\sigma_{22}) + \pi_{12}^p\sigma_{33} + f_p(\Delta T) \tag{3.1}$$

$$\left.\frac{\Delta\rho}{\rho}\right|_{90°} = \frac{\pi_S^p}{2}(\sigma_{11}+\sigma_{22}) - \frac{\pi_{44}^p}{2}(\sigma_{11}-\sigma_{22}) + \pi_{12}^p\sigma_{33} + f_p(\Delta T) \tag{3.2}$$

$$\left.\frac{\Delta\rho}{\rho}\right|_{45°} = \frac{\pi_S^n}{2}(\sigma_{11}+\sigma_{22}) + \pi_D^n\sigma_{12} + \pi_{12}^n\sigma_{33} + f_n(\Delta T) \tag{3.3}$$

$$\left.\frac{\Delta\rho}{\rho}\right|_{-45°} = \frac{\pi_S^n}{2}(\sigma_{11}+\sigma_{22}) - \pi_D^n\sigma_{12} + \pi_{12}^n\sigma_{33} + f_n(\Delta T) \tag{3.4}$$

where ρ is the directional resistivity of silicon and $f(\Delta T)$ is a function describing the effect of temperature on resistivity.

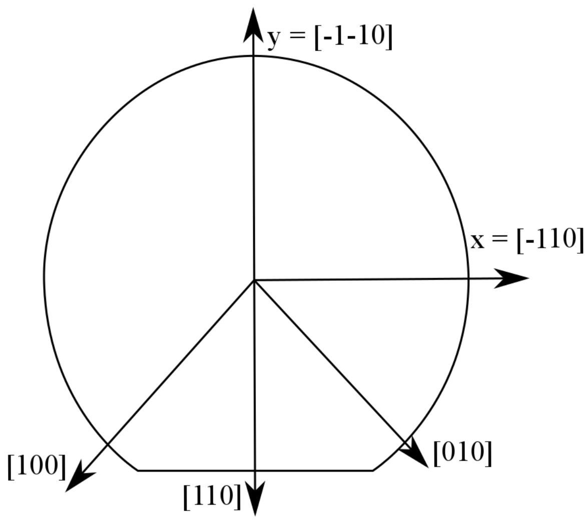

Figure 3.1: Coordinate system for (100) Silicon.

The drain current of a Metal-Oxide Semiconductor Field-Effect Transistor (MOSFET) in the saturation region can be described by the following well-known equation [2]:

$$I_D = \frac{1}{2}\mu C_{ox}\frac{W}{L}(V_{GS} - V_{TH})^2 \tag{3.5}$$

where:
V_{GS} – voltage between gate and source;
V_{TH} – threshold voltage of MOSFET transistor;
μ - mobility of electrical carriers in transistor channels;
C_{ox} – capacitance of the oxide layer;
W – width of the MOSFET channel; and
L – length of the MOSFET channel.

It is worth mentioning that the deformation of a silicon chip is small because of its large Young's modulus, even when it is subjected to relatively high stresses. Therefore, dimensional changes caused by mechanical stresses can be ignored in the above equation.

It has been proven that the threshold voltage is independent of mechanical stresses [2]. Thus, a small change in the drain current induced by mechanical stresses mainly depends on mobility changes. This can be described as [2]:

$$\frac{\Delta I_D}{I_D} = \frac{\Delta\mu}{\mu} \tag{3.6}$$

Mobility of electrical carriers is directly related to the resistivity of silicon [30]. Thus, the relationship can be written as:

$$\frac{\Delta\rho}{\rho} = -\frac{\Delta\mu}{\mu} \tag{3.7}$$

Combining 3.6 and 3.7 yields:

$$\frac{\Delta I_D}{I_D} = -\frac{\Delta\rho}{\rho} \tag{3.8}$$

The measured current values can be expressed in an incremental form as:

$$I_D = I_{D0} + \Delta I_D = I_{D0}\left(1 - \frac{\Delta\rho}{\rho}\right) \tag{3.9}$$

where I_{D0} is the reference current measured in the absence of mechanical stresses. Substituting Eqs. 6.1,6.2,4.3,6.4 into 3.9 yields [2]:

$$I_D\Big|_{0^\circ} = I_{D0}\left[1 - \frac{\pi_S^p}{2}(\sigma_{11} + \sigma_{22}) - \frac{\pi_{44}^p}{2}(\sigma_{11} - \sigma_{22}) - \pi_{12}^p\sigma_{33} + f_p(\Delta T)\right] \tag{3.10}$$

$$I_D\Big|_{90^\circ} = I_{D0}\left[1 - \frac{\pi_S^p}{2}(\sigma_{11}+\sigma_{22}) + \frac{\pi_{44}^p}{2}(\sigma_{11}-\sigma_{22}) - \pi_{12}^p\sigma_{33} + f_p(\Delta T)\right] \tag{3.11}$$

$$I_D\Big|_{45^\circ} = I_{D0}\left[1 - \frac{\pi_S^n}{2}(\sigma_{11}+\sigma_{22}) - \pi_D^n\sigma_{12} - \pi_{12}^n\sigma_{33} + f_p(\Delta T)\right] \tag{3.12}$$

$$I_D\Big|_{-45^\circ} = I_{D0}\left[1 - \frac{\pi_S^n}{2}(\sigma_{11}+\sigma_{22}) + \pi_D^n\sigma_{12} - \pi_{12}^n\sigma_{33} + f_p(\Delta T)\right] \tag{3.13}$$

where Π is the effective piezoresistive constants that are influenced by a circuit.

The above equations are combined to produce the following relationships that do not contain the reference current:

$$\frac{I_D\Big|_{0^\circ} - I_D\Big|_{90^\circ}}{I_D\Big|_{0^\circ} + I_D\Big|_{90^\circ}} = \frac{1}{2}\frac{-\pi_{44}^p(\sigma_{11}-\sigma_{22})}{1-\pi_S^p\left(\frac{\sigma_{11}+\sigma_{22}}{2}\right) - \pi_{12}^p\sigma_{33} + f(\Delta T)} \tag{3.14}$$

$$\frac{I_D\Big|_{+45^\circ} - I_D\Big|_{-45^\circ}}{I_D\Big|_{+45^\circ} + I_D\Big|_{-45^\circ}} = \frac{-\pi_D^n\sigma_{12}}{1-\pi_S^n\left(\frac{\sigma_{11}+\sigma_{22}}{2}\right) - \pi_{12}^n\sigma_{33} + f(\Delta T)} \tag{3.15}$$

The normal stress difference, $D(\sigma) = \sigma_{11} - \sigma_{22}$, and the in-plane shear stress, σ_{12}, then, can be expressed as:

$$\sigma_{11}-\sigma_{22} = D(\sigma) = -\frac{2}{\pi_{44}^p(T)}\left(1-\pi_S^p\left(\frac{\sigma_{11}+\sigma_{22}}{2}\right) - \pi_{12}^p\sigma_{33}\right)\left(\frac{I_D\Big|_{0^\circ} - I_D\Big|_{90^\circ}}{I_D\Big|_{0^\circ} + I_D\Big|_{90^\circ}}\right) \tag{3.16}$$

$$\sigma_{12} = \frac{-1}{\pi_D^n(T)}\left(1-\pi_S^n\left(\frac{\sigma_{11}+\sigma_{22}}{2}\right) - \pi_{12}^n\sigma_{33}\right)\left(\frac{I_D\Big|_{+45^\circ} - I_D\Big|_{-45^\circ}}{I_D\Big|_{+45^\circ} + I_D\Big|_{-45^\circ}}\right) \tag{3.17}$$

It is important to note that the temperature term, $f(\Delta T)$, can be incorporated into the above governing equations by introducing the temperature-dependent piezoresistive coefficients, $\pi_{44}^p(T)$ and $\pi_D^n(T)$.

It is often assumed that the contributions of the sum of in-plane normal stresses, $\sigma_{11}+\sigma_{22}$, and the out-of-plane stress, σ_{33}, are negligible [2]; i.e.,

$$D^p = 1-\pi_S^p\left(\frac{\sigma_{11}+\sigma_{22}}{2}\right) - \pi_{12}^p\sigma_{33} \approx 1 \tag{3.18}$$

$$D^n = 1 - \pi_S^n \left(\frac{\sigma_{11} + \sigma_{22}}{2} \right) - \pi_{12}^n \sigma_{33} \approx 1 \tag{3.19}$$

Then, Eqs. 3.16 and 3.17 can take the following forms [32]:

$$\sigma_{11} - \sigma_{22} = D(\sigma) \approx -\frac{2}{\pi_{44}^p(T)} \left(\frac{I_D\big|_{0^\circ} - I_D\big|_{90^\circ}}{I_D\big|_{0^\circ} + I_D\big|_{90^\circ}} \right) \tag{3.20}$$

$$\sigma_{12} \approx -\frac{1}{\pi_D^n(T)} \left(\frac{I_D\big|_{+45^\circ} - I_D\big|_{-45^\circ}}{I_D\big|_{+45^\circ} + I_D\big|_{-45^\circ}} \right) \tag{3.21}$$

In practice, current mirror circuits are utilized to measure the currents required in the above equations. Two current mirrors used in this study are shown in Figure 4.2, where a pair of MOS transistors is connected in each current mirror circuit. The branches of the current mirrors are oriented differently with respect to the crystallographic axes of silicon, which makes the transistors respond differently to applied mechanical stresses. The pMOS current mirror used for the normal stress difference measurement (Eq. 3.20) is shown in (a), and the nMOS current mirror used for the shear stress measurement (Eq. 3.21) is shown in (b).

The current mirror configuration is forcing the same current in both branches of the circuit if the parameters of both transistors are identical. When mechanical stresses are applied, the circuit becomes out of balance, and this effect is quantified by measuring the current differences in two branches of the current mirror. The applied stresses are determined from the measured current differences.

It is important to note that the current mirror device is not symmetrical. The input branches of the forward current mirrors contain pMOS oriented at 0° and nMOS oriented at -45°. In the reverse current mirrors, however, the input branches contain pMOS oriented at 90° and nMOS oriented at 45°. The effect of the inherently unsymmetrical configuration of current mirrors is canceled by averaging signals from the forward and reverse current mirrors.

3.3. Sensor Chip and Data Acquisition

This section describes the sensor chip and the data acquisition unit used in the experiment.

3.3.1. Sensor Chip Construction

The sensor chip consists of two sensors, as shown in Figure 4.3(a). Each sensor contains 12 measurement cells in a $4x4$ matrix format. Four cells in the corners are inactive, and they are used as bonding pads.

The temperature-dependent piezoresistive coefficients, $\pi_{44}^p(T)$ and $\pi_D^n(T)$ were measured using an input current of $1mA$ during device calibration. The same current was

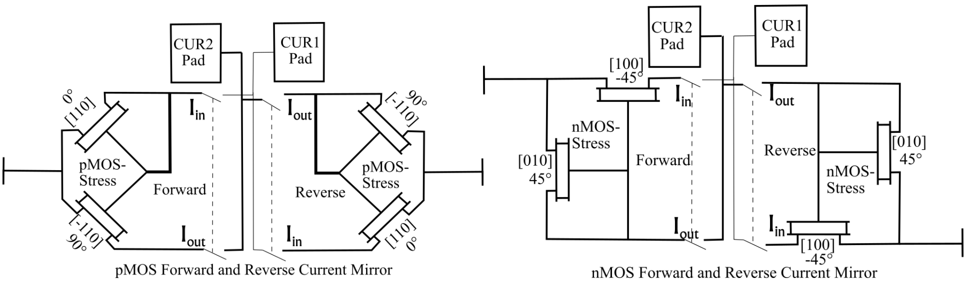

(a) (b)

Figure 3.2: Current mirror circuit used for stress measurement (a) pMOS current mirror used for the difference in normal in-plane stress measurement (b) nMOS current mirror used for the xy shear stress measurement.

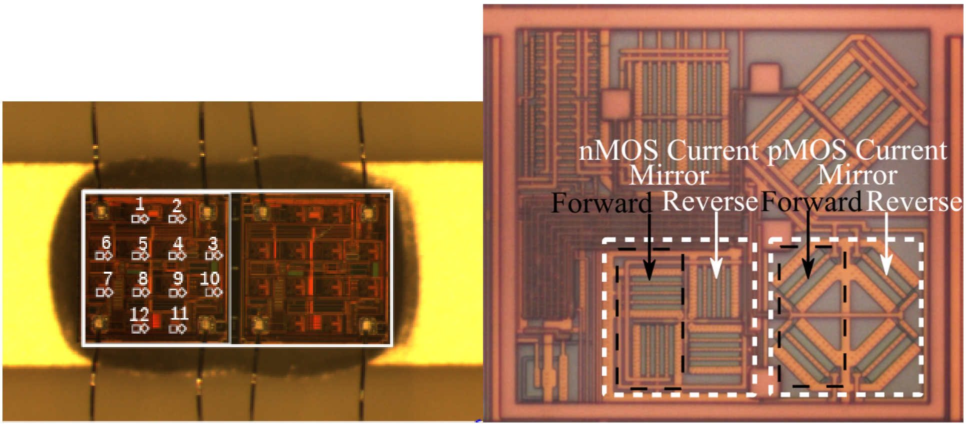

(a) (b)

Figure 3.3: Construction of a sensor (a) cells placed in a matrix and (b) single measurement cell containing two current mirrors in a forward and reverse arrangement.

used for measurements to avoid a potential error associated with the current-dependent piezoresistive constants. It was found that the coefficients have a linear relationship with temperature as [32]:

$$\pi_{44}^{p}(T) = \beta_{44}^{p} \cdot (T - 293) + \pi_{44}^{p}(293) = -1.33 \cdot 10^{-3} \cdot (T - 293) + 1.008 \tag{3.22}$$

$$\pi_{D}^{n}(T) = \beta_{D}^{n} \cdot (T - 293) + \pi_{D}^{n}(293) = 0.83 \cdot 10^{-3} \cdot (T - 293) + 0.78 \tag{3.23}$$

where the unit of the coefficients is K/GPa. As shown in Figure 4.3 (b), each cell contains two pairs of stress sensitive pMOS and nMOS transistors. The channels of current mirrors are selected to produce the most significant sensitivity to stresses. Each pair represents the forward and reverse current mirrors. The consecutive cells are measured in series. To switch between different devices within a cell and between different cells, a custom communication protocol was developed. The communication was done over power supply terminals to minimize the number of required pins, both by current and voltage modulation. Stress measurements were always made with the same highest power supply level.

3.3.2. Data Acquisition Unit

The data from the sensors were collected by a dedicated acquisition unit (Figure 4.5). The functional scheme of the solution is presented in Figure 4.4. A microcontroller took control over the whole process. All inputs of the sensors were controlled by a digital-to-analog converter (DAC). It includes a voltage generator, which supplies power to the chip as well as the current source. Both of them were designed to ensure good stability and accuracy. Outputs from the chip were digitalized by an analog-to-digital converter (ADC). The resolution of the current measurement was approximately 0.0625 μA, and the total error of conversion was below 2 Least Significant Bit (LSB) [31]. The acquisition unit measured eight sensors simultaneously, and the collected data was saved in a USB flash drive. The data is saved in an unprocessed way, which means that only the measured values of currents and voltages are saved.

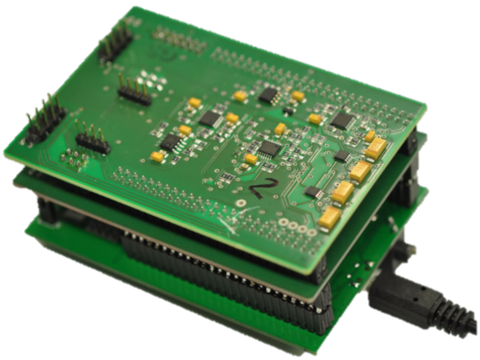

Figure 3.4: Data acquisition unit. The board consists of a microcontroller, power source and logic board.

3.4. Uncertainty of Sensor Signal

Free-standing sensor chips are prepared to investigate the uncertainty of sensor signals. The random noise of the measurement system is evaluated first from signals obtained at room temperature. Then, the free-standing sensor chips are subjected to a thermal cycle, and the systematic noise associated with the temperature is evaluated.

3.4.1. Random Measurement Uncertainties

The following procedure was used to fabricate a free-standing sensor chip shown in Figure 4.6: (1) a sensor chip is mounted on a low temperature co-fired ceramics (LTCC)

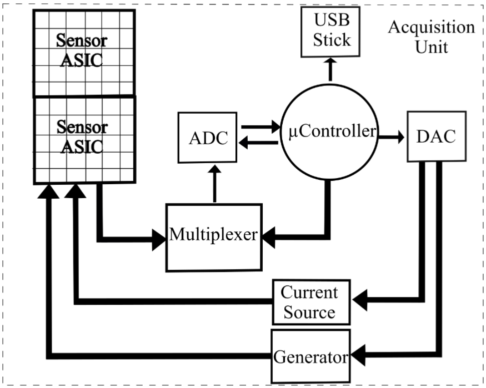

Figure 3.5: Functional scheme of the acquisition unit. The microcontroller first sends the signal to the DAC that regulates the sensor's current and voltage. Then an ADC reads out the sensor response. In addition, a multiplexer is used to switch between different sensors.

substrate with a high temperature curing non-conductive adhesive; (2) the sensor pads and the LTCC pads are connected by wire bonds; and (3) the chip is unglued from the LTCC surface by dissolving the glue using a solvent.

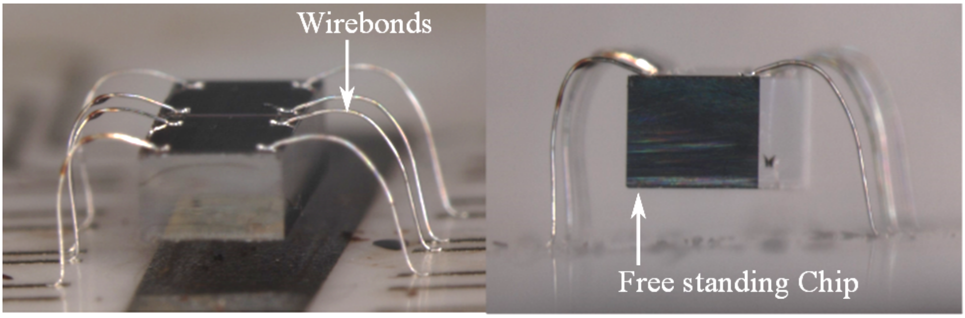

Figure 3.6: Free-standing chip electrical connections. Every each sensor needs four wire connections. The picture depicts two sensors.

Initial measurements were made at room temperature (20°C). The ADC had a sampling rate of 52,000 Samples per Second (SPS). During the Acquisition Unit (AU) development, a supplementary study was performed to examine how many samples would be required for a stable signal. The current and voltage values of each phase were measured 40 times and were averaged subsequently. The whole cycle of sensor phase, cell, and sensor switching take around 2 minutes.

The representative current values of four cells measured at room temperature are shown in Figure 4.7. They were obtained by averaging the current values of the forward and reverse modes. The average current of the pMOS current mirror (I_{0° and I_{+90°) and the average of the nMOS current mirror (I_{-45° and I_{+45°) are shown in (a) and (b), respectively. A total of 50 measurements were made, and some low level of random noise was observed.

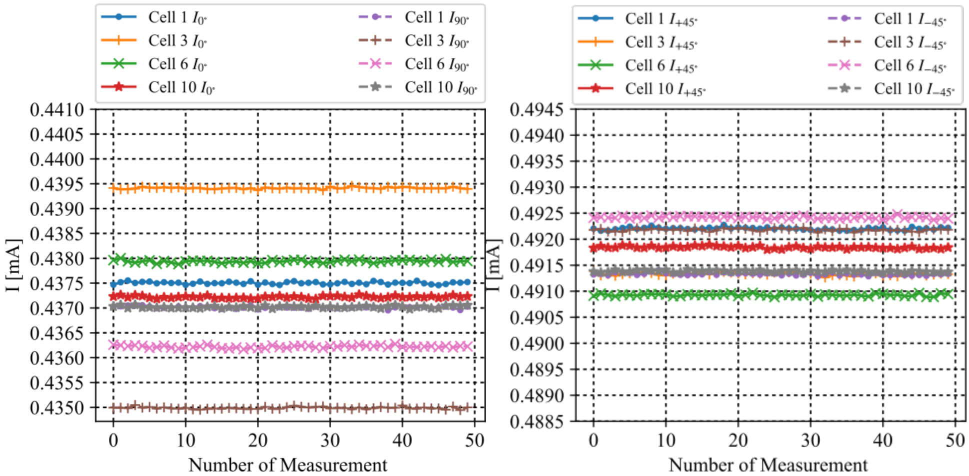

(a) (b)

Figure 3.7: Representative averaged current values obtained at room temperature: (a) the average of $I_{0°}$ and $I_{+90°}$ of the pMOS current mirror and (b) the average of $I_{-45°}$ and $I_{+45°}$ of the nMOS current mirror.

The effect of the random noise on the uncertainty in stress measurements was evaluated. Figure 4.8 shows the normal stress difference and the shear stress of each cell measured from a free standing sensor chip at room temperature, where the error bars indicate the random noise determined from 50 measurements. The results indicate that the effect of the random noise on the stress calculations was virtually negligible: the average random uncertainty is only 0.072 MPa (1.49%) and 0.044 MPa (2.28%) for the stress difference and the shear stress, respectively.

It is important to note that stress values are high in some cells and vary significantly from cell to cell, although the chip is not subject to any external loading (free-standing). This is attributed to the residual stresses of the chip produced by the manufacturing process, and this will be discussed in more detail later.

3.4.2. Systematic Uncertainty Associated with Residual Stresses

As observed earlier, the stress values of free-standing chips at room temperature are large and have significant cell-to-cell variations. These stresses are not associated with any intended loadings and should be negated for stress measurement applications. The stresses obtained from all 12 free-standing chips are summarized in Figure 4.10, where the stress difference and the shear stress of each cell are shown in (a) and (b), respectively. The results show significant chip-to-chip variations attributed to the residual stresses caused by the semiconductor manufacturing process. Consequently, it does not seem practical to use the absolute stress values for any quantitative analyses due to this uncertainty. Instead, it is recommended to use the changes of stresses between two loading states because this uncertainty is present in both loading states. The following

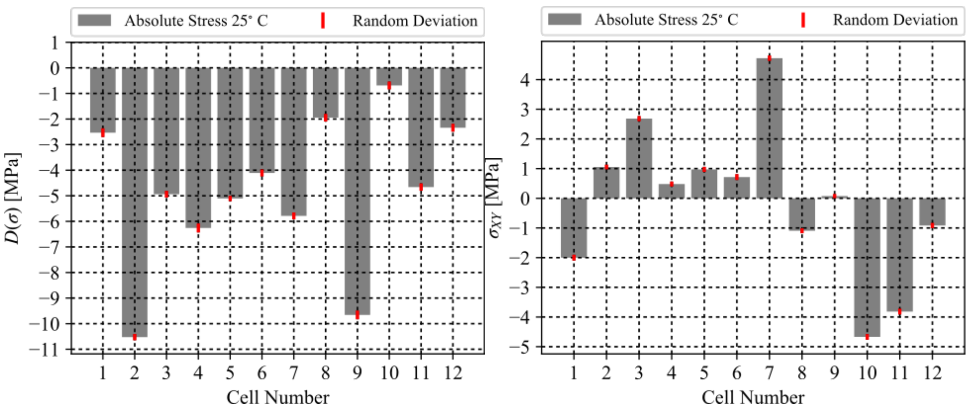

(a) (b)

Figure 3.8: (a) Normal stress difference and (b) shear stress obtained from a free standing chip at room temperature. The error bars indicate the random noise determined from 50 measurements.

experiment was conducted to illustrate this concept.

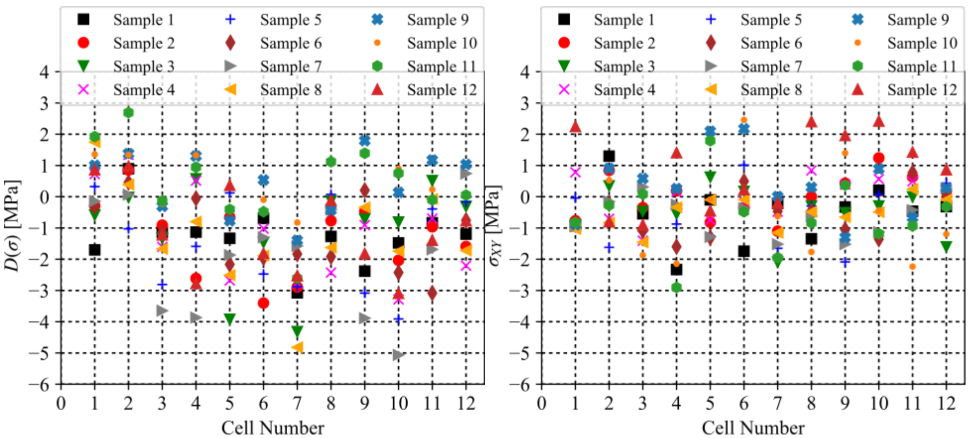

(a) (b)

Figure 3.9: (a) Normal stress difference and (b) shear stress obtained from 12 free standing chip at room temperature.

The 12 free-standing chips were subjected to thermal cycles of $-40°C$ and $125°C$, and the relative stress difference and the shear stress caused by the thermal excursion were determined by subtracting the values at $-40°C$ from the values at $125°C$. The results are shown in Figure 4.11, where the error bars show the chip-to-chip variations. The average uncertainty ranges from -4 to 2 MPa over 12 cells. These values represent the effect of residual stresses on each cell caused by cooling the free-standing chips from $125°C$ to

$-40°C$. The chip-to-chip variation is much smaller than that of the absolute stresses at room temperature (Figure 4.10). The values shown in Figure 4.11 can be used effectively to negate the systematic uncertainty associated with the residual stresses.

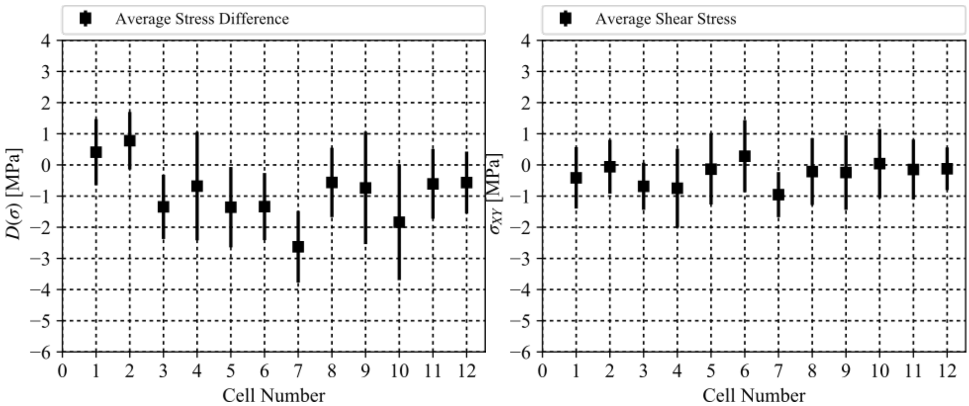

(a) (b)

Figure 3.10: Stresses of free standing chips, caused by cooling them from 125°C to $-40°C$: (a) the stress difference and (b) the shear stress. The error bars show the variations obtained from 12 independent measurements of free-standing chips.

3.5. ACCURACY OF LOAD-INDUCED STRESS MEASUREMENTS

The accuracy of the sensor to measure the stresses produced by a thermo-mechanical loading is evaluated. A numerical model is built and subsequently calibrated by an optical technique called moire interferometry. The stresses of the cells predicted by the calibrated model are compared with the experimental data to establish the accuracy while taking into consideration the uncertainties discussed in Section 3.4.

3.5.1. TEST VEHICLE AND NUMERICAL MODEL CONSTRUCTION

A test vehicle used in the study is shown schematically in Figure 4.12. The sensor chip was mounted on an LTCC substrate using a high temperature curing non-conductive adhesive. A set of wire bonds provided the electrical connection between the chips and the substrate.

3.5.2. NUMERICAL MODEL CONSTRUCTION

The model construction started with the preparation of the detailed geometry of the stress sensor. The geometrical model consisted of the important details of the construction, such as NiPdAu traces on the LTCC, detailed adhesive shape, and the exact geometry of the chip. All these properties were obtained from the cross-sections using an optical microscope. Figure 4.14 (a) shows the whole LTCC assembly, and Figure 4.14 (b) depicts the details of the chip area.

The full layout of the LTCC assembly has discretized on Figure 4.14 while considering

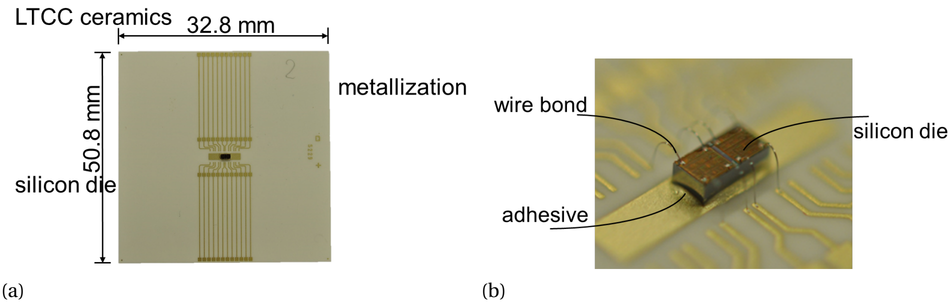

Figure 3.11: LTCC Test Vehicle. The two sensors in a single die is glued on top of an LTCC. The board consists of signal traces that connects the sensor to the exterior pads, on which solder wires are placed.

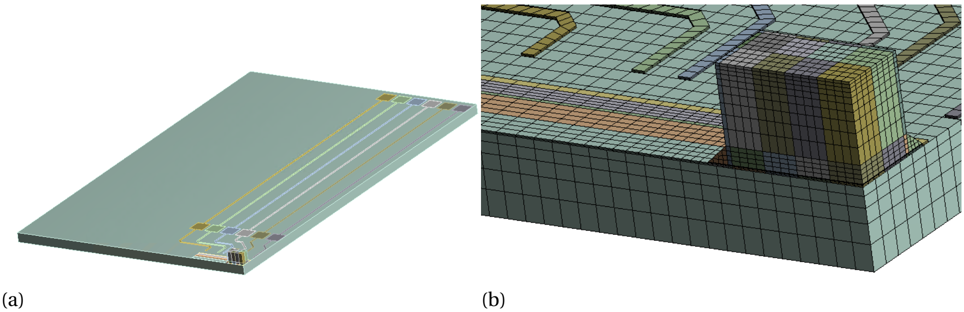

Figure 3.12: Mesh quality used in numerical model. The focus areas are identified by the fine mesh.

the half symmetry. A supplementary mesh sensitivity study was conducted, where mesh sizes were reduced until the stresses of the sensor remained constants. The element type was a higher order, 20 nodes hexahedral brick element with mid-side nodes. For the thin materials such as the die attach and the metal trace, a minimum of two elements were used through the thickness. Another critical task of the modeling was to produce a detailed representation of the stress sensing cells. The thickness of the MOSFET branch in the actual sensor chip, in which the calculation of the stress was performed, was approximately 10 μm thick. The sensor chip was discretized to produce the 10 μm thick top layer, as shown in Figure 4.16(a). In addition, each stress sensing cell was divided into 4 x 4 elements so that the elements matched to the geometry of current mirrors shown in Figure 4.3(b). The top view of the mesh is shown in Figure 4.16(b) to explain the mesh geometry more clearly. It shows the half of the sensor chip (half symmetry), where the elements corresponding to the current mirrors for the stress difference and the shear stress calculations are marked by the green and purple squares, respectively. The LTCC and the silicon die were modeled as isotropic elastic solid and orthotropic elastic solid, respectively. The properties of the die attach were measured by a dynamic mechanical analyzer (DMA) and thermomechanical analyzer (TMA). It was also modeled as an isotropic elastic solid with the temperature-dependent modulus of elasticity and coefficient of thermal expansion (CTE). The glass transition temperature of the die attach was 100°C. The total thickness of NiPdAu metal trace was 17 μm, while the thickness of Pd and Au was smaller than 1 μm. The effect of Pd and Au on the trace property was negligible, and the trace was modeled as pure Ni. Details of the material properties used in the numerical model are summarized in Table 3.1.

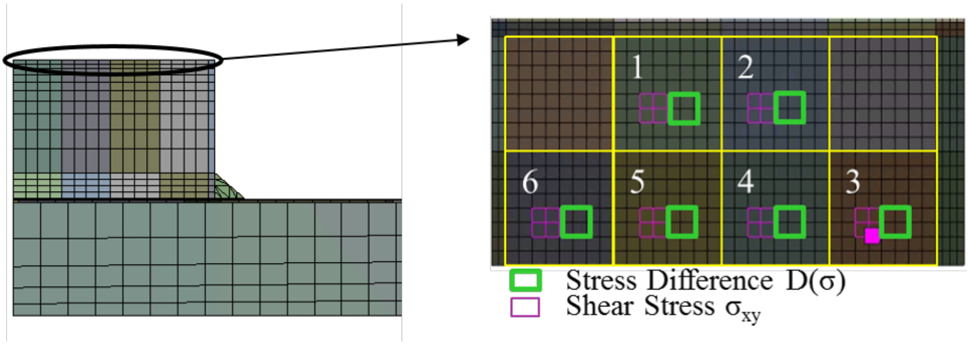

(a) (b)

Figure 3.13: Detailed mesh of the sensor chip: (a) side view and (b) top view where the elements used to extract stress are marked.

Material properties considered in the simulation	Modulus of elasticity [MPa]	CTE [ppm/K]	Material law
LTCC	128000	4.5	Linear-elastic
Silicon die	167000	2.8	Linear-elastic
Metallization	80000	17	Linear-elastic
Die attach	3940	40	Linear-elastic

Table 3.1: Material properties.

3.5.3. Model Validation by Moiré interferometry

Moiré interferometry is a full-field optical technique to measure the in-plane deformations with high sensitivity, high signal-to-noise ratio, and excellent clarity [33]. The outputs are the contour maps of in-plane displacements. It has been used widely for electronic packaging design, and reliability assessment [34]. The specimen used for moire experiments is shown in Figure 4.17. A cross-line high frequency diffraction grating, fs, of 1200 lines per mm was replicated on the specimen surface, and it deformed together with the underlying specimen.

In this work, an advanced moiré interferometry system was used to document the required deformation fields (Figure 4.18) [35]. The system consists of (1) a portable engineering moiré interferometer that provides two sets of virtual reference gratings, (2) a conduction chamber built on a high performance thermo-electric cooler that provides accurate temperature control, and (3) a high-resolution digital camera with an objective microscope lens. The thermal conduction chamber is mounted on an x-y-z translation stage, which allows positioning and focusing the specimen. More details of the

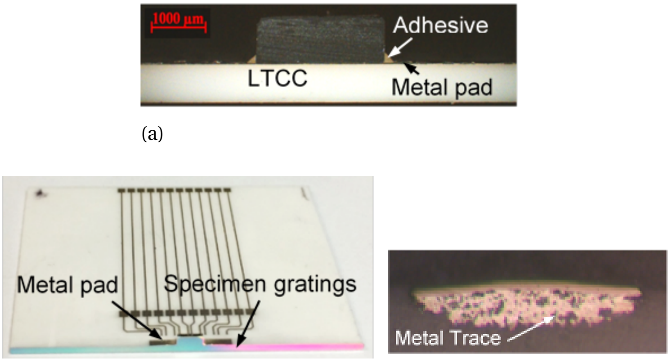

(a)

(b) (c)

Figure 3.14: (a) Specimen cross section, (b) the replicated specimen gratings and (c) the embedded metal trace.

system can be found in Ref. [35]. A virtual reference grating, f, was formed by two coherent beams of light provided by the interferometer. The deformed specimen grating and the uniform reference grating interacted to produce moiré patterns of in-plane displacements.

To obtain more detailed displacement fields around the chip, the measurement sensitivity was improved further by an image processing scheme called the optical/digital fringe multiplication method [33]. The final fringe patterns representing the thermally-induced displacements are shown in Figure 4.19, where the contour interval is 104 nm displacement per fringe order. It is to be noted that the fringe patterns represent the relative displacement along the x (or U) and y (or V) directions, caused by heating ($125°C$) or cooling ($-40°C$) the assembly from the reference temperature (room).

Detailed 3-D models whose dimensions were identical to the moire specimens were constructed for model calibration. A traction-free boundary condition was imposed on the cross sections to simulate the moiré experiments.

The displacements at $125°C$ and $-40°C$ were extracted from the fringe patterns, and the deformations caused by cooling the assembly from $125°C$ to $-40°C$ were compared with the modeling results. The results are shown in Figure 4.20, where the displacements along Lines 1 and 2 shown in the inset are compared. The data match each other very well, which verifies the validity of the numerical model.

It is worth mentioning that the initial comparison was not as good as shown in Figure 4.20. Several adjustments were made to achieve a high level of validity. The most critical adjustment was the position of the metal trace and metal pad layer. They were modeled as a separate layer on the top of the LTCC substrate in the initial attempt. It was found from a closer examination that they were embedded in the LTCC substrate (Figure 4.17(c)), and the model has corrected accordingly. This adjustment brought the agreement to the desired level. The result was attributed to the high modulus of the metal.

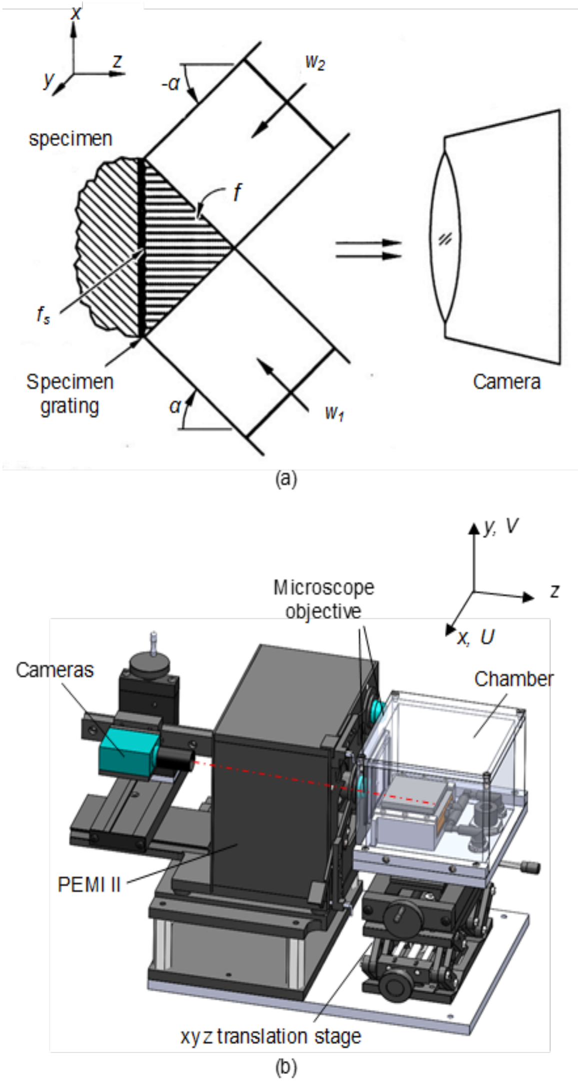

Figure 3.15: Schematic illustration of (a) the principle of moiré interferometry and (b) the optical/mechanical configuration of an advanced portable moiré system.

3.5.4. ACCURACY OF LOAD-INDUCED STRESS MEASUREMENTS

The predictive FEM model was used to evaluate the accuracy of the sensor measurements under an in-situ loading condition. The stress at each stress sensing element group was assessed using the stress averaged over the corresponding four elements.

Two LTCC assemblies (Figure 4.12) were subjected to the same thermal cycle used for the moire experiment. The stress signals were obtained at the peak temperatures (125°C and −40°C). The stress difference and the shear stresses at −40°C were then subtracted

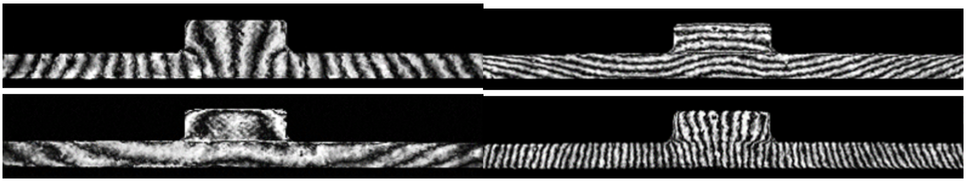

(a) (b)

Figure 3.16: Relative local in-plane displacement fringe patterns after apply O/DFM with $\beta = 4$ at (a)$-40°C$ (b)at $125°C$.

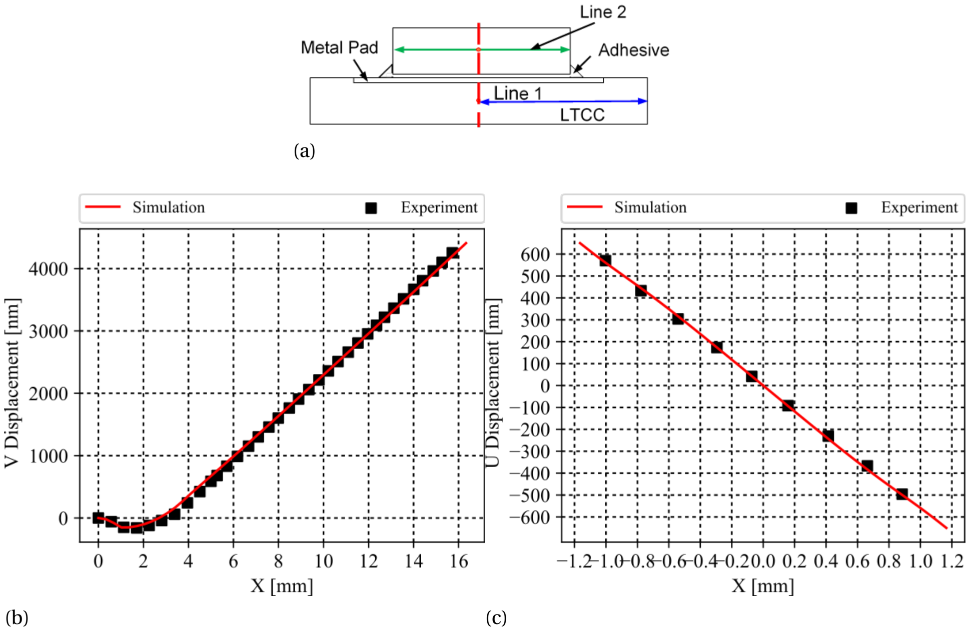

Figure 3.17: Relative local in-plane displacement fringe patterns after apply O/DFM with $\beta = 4$ at (a)$-40°C$ (b)at $125°C$.

from those at $125°C$.

The stress difference and the shear stress predicted by the model are compared with experimental data in Figure 4.23. It is important to note that the free-standing sensors' systematic uncertainty was subtracted from the experimental data. The error bars indicate the standard deviations of the systematic uncertainties.

The stress difference shows good agreement in the trend and in the magnitudes within the systematic uncertainty. This level of agreement is excellent for stress comparison, which is typically a lot more challenging than displacement or strain comparisons. However, the magnitude of the shear stress is very small and is even much smaller than the systematic uncertainty. The in-plane shear stress may not be useful for typical electronics packaging applications.

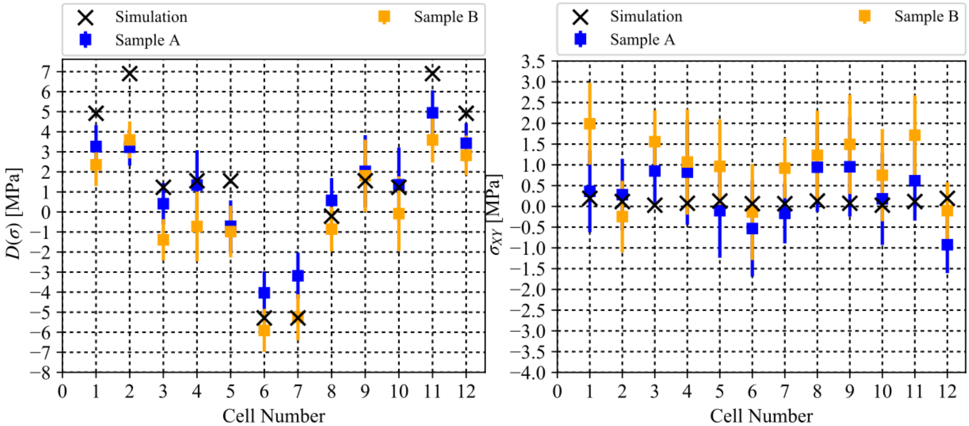

(a) (b)

Figure 3.18: Comparison of experimental data and numerical results: (a) the stress difference and (b) the shear stress.

3.6. CONCLUSION

The random and systematic measurement uncertainties of the CMOS-based piezoresistive stress sensor were evaluated. The random uncertainty associated with the data acquisition unit was evaluated first by measuring raw current data using uniquely fabricated free-standing sensor chips. The results obtained from 50 repetitions indicated that the random uncertainty was negligible. The stress measurements of the free-standing sensor chips proceeded to evaluate the systematic uncertainties associated with the manufacturing-induced residual stresses. The stresses obtained from the free-standing sensor chips indicated significant cell-to-cell as well as chip-to-chip variations. It was recommended that only the changes between two loading states be used for actual applications. A procedure to negate the systematic uncertainties was also proposed and implemented. Finally, the stress measurement accuracy of the sensor chip under an in-situ loading was quantified by a numerical model verified by a sub-micron sensitivity optical technique called moire interferometry. When the systematic uncertainty determined from the free-standing sensor chips were subtracted from the experimental data, the stress difference showed excellent agreement with the numerical prediction. However, the magnitudes of the shear stresses were so low that the systematic uncertainties dominated the shear stress signals. It was also recommended that only the stress difference be used for actual applications.

REFERENCES

[1] A. Prisacaru, A. Palczynska, P. Gromala, B. Wu, B. Han, and G. Zhang, *Accuracy of cmos-based piezoresistive stress sensor for engineering applications of thermal load-*

ing condition: Theoretical review and experimental validation, IEEE Sensors Journal **19**, 9139 (2019).

[2] W. G. Pfann and R. N. Thurston, *Semiconducting stress transducers utilizing the transverse and shear piezoresistance effects,* Journal of Applied Physics **32**, 2008 (1961), https://doi.org/10.1063/1.1728280 .

[3] R. Jaeger, J. Suhling, and R. Ramani, *Errors associated with the design, calibration and application of piezoresistive stress sensors in (100) silicon,* **17**, 97 ().

[4] J. Suhling and R. Jaeger, *Silicon piezoresistive stress sensors and their application in electronic packaging,* **1**, 14.

[5] A. P. Dorey, *A high sensitivity semiconductor strain sensitive circuit,* Solid-State Electronics **18**, 295 (1975).

[6] R. C. Jaeger, R. Ramani, J. C. Suhling, and Y. Kang, *Cmos stress sensor circuits using piezoresistive field-effect transistors (pifets),* in *Digest of Technical Papers., Symposium on VLSI Circuits.* (1995) pp. 43–44.

[7] R. Jaeger, J. Suhling, R. Ramani, A. Bradley, and Jianping Xu, *CMOS stress sensors on [100] silicon,* **35**, 85 ().

[8] Y. Chen, R. C. Jaeger, and J. C. Suhling, *Cmos sensor arrays for high resolution die stress mapping in packaged integrated circuits,* IEEE Sensors Journal **13**, 2066 (2013).

[9] T. Kaufmann, D. Kopp, F. Purkl, M. Baumann, P. Ruther, and O. Paul, *Piezoresistive response of five-contact vertical hall devices,* in *SENSORS, 2010 IEEE* (2010) pp. 562–565.

[10] B. Lemke, R. Baskaran, and O. Paul, *Piezoresistive cmos sensor for the localized measurement of five independent stress components,* in *2010 IEEE 23rd International Conference on Micro Electro Mechanical Systems (MEMS)* (2010) pp. 596–599.

[11] J. Bartholomeyczik, S. Brugger, P. Ruther, and O. Paul, *Multidimensional cmos in-plane stress sensor,* IEEE Sensors Journal **5**, 872 (2005).

[12] P. Gieschke, Y. Nurcahyo, M. Herrmann, M. Kuhl, P. Ruther, and O. Paul, *Cmos integrated stress mapping chips with 32 n-type or p-type piezoresistive field effect transistors,* in *2009 IEEE 22nd International Conference on Micro Electro Mechanical Systems* (2009) pp. 769–772.

[13] P. Gieschke, J. Held, M. Doelle, J. Bartholomeyczik, P. Ruther, and O. Paul, *Smart brush based on a high density cmos stress sensor array and su-8 microposts,* in *2007 IEEE 20th International Conference on Micro Electro Mechanical Systems (MEMS)* (2007) pp. 631–634.

[14] M. Doelle, C. Peters, P. Ruther, and O. Paul, *Piezo-fet stress-sensor arrays for wire-bonding characterization,* Journal of Microelectromechanical Systems **15**, 120 (2006).

[15] M. Doelle, C. Peters, P. Gieschke, P. Ruther, and O. Paul, *Two-dimensional high density piezo-fet stress sensor arrays for in-situ monitoring of wire bonding processes,* in *17th IEEE International Conference on Micro Electro Mechanical Systems. Maastricht MEMS 2004 Technical Digest* (2004) pp. 829–832.

[16] J. Roberts, S. Hussain, M. K. Rahim, M. Motalab, J. C. Suhling, R. C. Jaeger, P. Lall, and R. Zhang, *Characterization of microprocessor chip stress distributions during component packaging and thermal cycling,* in *2010 Proceedings 60th Electronic Components and Technology Conference (ECTC)* (2010) pp. 1281–1295.

[17] J. C. Roberts, M. K. Rahim, S. Hussain, J. C. Suhling, R. C. Jaeger, and P. Lall, *Die stress variation in area array components subjected to accelerated life testing,* in *2008 11th Intersociety Conference on Thermal and Thermomechanical Phenomena in Electronic Systems* (2008) pp. 705–713.

[18] J. Roberts, M. Motalab, S. Hussain, J. C. Suhling, R. C. Jaeger, and P. Lall, *Measurement of die stresses in microprocessor packaging due to thermal and power cycling,* in *2012 IEEE 62nd Electronic Components and Technology Conference* (IEEE) pp. 756–770.

[19] M. K. Rahim, J. Roberts, J. C. Suhling, R. C. Jaeger, and P. Lall, *Continuous in-situ die stress measurements during thermal cycling accelerated life testing,* in *2007 Proceedings 57th Electronic Components and Technology Conference* (2007) pp. 1478–1489.

[20] F. Schindler-Saefkow, F. Rost, A. Otto, W. Faust, B. Wunderle, B. Michel, and S. Rzepka, *Stress chip measurements of the internal package stress for process characterization and health monitoring,* in *2012 13th International Thermal, Mechanical and Multi-Physics Simulation and Experiments in Microelectronics and Microsystems* (2012) pp. 1/10–10/10.

[21] Y. Chang, H. Chung, B. Lwo, and K. Tseng, *In situ stress and reliability monitoring on plastic packaging through piezoresistive stress sensor,* IEEE Transactions on Components, Packaging and Manufacturing Technology **3**, 1358 (2013).

[22] Y. Chang, H. Chung, B. Lwo, R. Tan, and K. Tseng, *In-situ reliability monitoring on pbga packaging through piezoresistive stress sensor,* in *2010 5th International Microsystems Packaging Assembly and Circuits Technology Conference* (2010) pp. 1–4.

[23] P. Lall, M. N. Islam, M. K. Rahim, and J. C. Suhling, *Prognostics and health management of electronic packaging,* IEEE Transactions on Components and Packaging Technologies **29**, 666 (2006).

[24] P. Lall, N. Islam, K. Rahim, J. Suhling, and S. Gale, *Leading indicators-of-failure for prognosis of electronic and mems packaging,* in *2004 Proceedings. 54th Electronic Components and Technology Conference (IEEE Cat. No.04CH37546)*, Vol. 2 (2004) pp. 1570–1578 Vol.2.

[25] P. Gromala, S. Fischer, T. Zoller, A. Andreescu, J. Duerr, M. Rapp, and J. Wilde, *Internal stress state measurements of the large molded electronic control units,* in *2013*

14th International Conference on Thermal, Mechanical and Multi-Physics Simulation and Experiments in Microelectronics and Microsystems (EuroSimE) (2013) pp. 1–8.

[26] P. Gromala, A. Palczynska, and B. Han, *Prognostic approaches for the wirebond failure prediction in power semiconductors: A case study using dpak package,* in *2015 16th International Conference on Electronic Packaging Technology (ICEPT)* (2015) pp. 413–418.

[27] A. Palczynska, P. J. Gromala, D. Mayer, B. Han, and T. Melz, *In-situ investigation of emc relaxation behavior using piezoresistive stress sensor,* in *2015 16th International Conference on Thermal, Mechanical and Multi-Physics Simulation and Experiments in Microelectronics and Microsystems* (2015) pp. 1–5.

[28] A. Palczynska, A. Prisacaru, P. J. Gromala, B. Han, D. Mayer, and T. Melz, *Towards prognostics and health monitoring: The potential of fault detection by piezoresistive silicon stress sensor,* in *2016 17th International Conference on Thermal, Mechanical and Multi-Physics Simulation and Experiments in Microelectronics and Microsystems (EuroSimE)* (2016) pp. 1–8.

[29] B. Wu, D.-S. Kim, B. Han, A. Palczynska, A. Prisacaru, and P. J. Gromala, *Hybrid approach to conduct failure prognostics of automotive electronic control unit using stress sensor as in situ load counter,* , 1.

[30] A. Prisacaru, A. Palczynska, A. Theissler, P. Gromala, B. Han, and G. Q. Zhang, *$in\ situ$failure detection of electronic control units using piezoresistive stress sensor,* IEEE Transactions on Components, Packaging and Manufacturing Technology **8**, 750 (2018).

[31] A. Devices, *Quad, 12-/14-/16-bit nanodacs with 5 ppm/°c on-chip reference, i2c interface,* **Rev. D** (2007).

[32] G. Robert Bosch GmbH, *Entwicklung eines integrierten stressmesssystems zur quantifizierung der 3d-verformung von sensorbauelementen in abhängigkeit des verpackungsprozesses, Abschlussbericht zum Verbundvorhaben iForce-Sens : Entwicklung eines integrierten Stressmesssystems zur Quantifizierung der 3D-Verformung von Sensorbauelementen in Abhängigkeit des Verpackungsprozesses : Laufzeit des Vorhabens: 01.01.2005 - 30.06.2008,* (2008), https://doi.org/10.2314/GBV:606643435.

[33] D. Post, B. Han, and P. Ifju, in *High Sensitivity Moiré: Experimental Analysis for Mechanics and Materials, Mechanical Engineering Series* (Springer-Verlag, 1994).

[34] B. Han, *Thermal stresses in microelectronics subassemblies: Quantitative characterization using photomechanics methods,* Journal of Thermal Stresses **26**, 583 (2003), https://doi.org/10.1080/713855954 .

[35] B. Wu and B. Han, *Advanced mechanical/optical configuration of real-time moiré interferometry for thermal deformation analysis of fan-out wafer level package,* IEEE

3

Transactions on Components, Packaging and Manufacturing Technology **8**, 764 (2018).

3

4

IN-SITU FAILURE DETECTION OF ELECTRONIC CONTROL UNITS USING PIEZORESISTIVE STRESS SENSOR

Recent advancements in automotive technologies, most notably autonomous driving, require electronic systems much more complex than realized in the past. The automotive industry has been forced to adopt advanced consumer electronics to satisfy the demand, and thus it becomes more challenging to assess system reliability while embracing the new technologies. The system-level reliability can be enforced by implementing a process called condition monitoring. In this chapter, a piezoresistive silicon-based stress sensor is implemented to recognize in-situ failure in outer molded electronic control units (ECU) subjected to reliability testing conditions. The test vehicle consists of six DPAK power packages and three stress sensors mounted on a Printed Circuit Board (PCB). A unique algorithm is proposed and implemented to handle the data obtained from the piezoresistive stress sensing cells. The accuracy of measured data is examined by the Finite Element Method (FEM), and the physical changes are validated with Scanning Acoustic Microscope (SAM). One-class support vector machines are used to autonomously classify data based on a training set of measurements from a healthy state. The reported results confirm that robust classification is possible based on data from the silicon stress sensor.

Parts of this chapter have been published in IEEE Transactions on Components, Packaging and Manufacturing Technology (2018) [1].

Condition Monitoring (CM) is a process to monitor parameters of system conditions, which is a critical component in predictive maintenance. Condition monitoring techniques have been used extensively for large-scale machinery and structures. More recently, condition monitoring has been adopted for advanced electronic systems, most notably automotive electronics, including batteries. Conventional sensors (e.g., sensors for temperature, humidity, vibration, etc.) are not most adequate for the condition monitoring of complex electronic system as they only measure the loading conditions. The piezoresistive stress sensors were developed to cope with the problem. The sensor measures directly the stresses of a silicon chip, and it was utilized in several electronic packaging applications [2] [3][4][5][6][7][8][9][10]. It was also implemented successfully to monitor the stresses in advanced electronic control unit (ECU) subjected to reliability testing conditions [11][12].

In order to extend its applicability into the Prognostics and Health Management (PHM) domain, it is required to link the in-situ measured stress to the damage or fault of the ECU, as illustrated in Figure 4.1.

PHM is an algorithm or a set of algorithms based on measurements and models, which collect input known information about the system/structure and data from strategically positioned sensors. Then it subsequently provides an output on different levels of prognostics such as failure detection, diagnostics, and lifetime prediction. Various levels of prognostics require different strategies/algorithms for successful implementation.

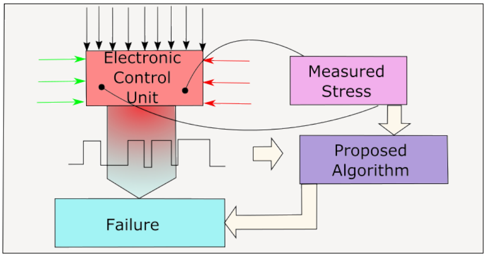

Figure 4.1: Stress Failure relationship. Various type of loads are causing ECU failures. The proposed algorithm is linking the measured stress with the failure.

As depicted in Figure 4.2, a well-implemented prognostic methodology should include the following items:

- Sensors for prognostics
- Data collection, processing, reduction, and feature extraction
- Data Security and integrity
- Identification and analyze precursors, Risk and uncertainty analysis
- Health assessment, anomaly detection, fault recognition, fault classification, fault propagation
- Physics-of-Failure (PoF), Damage Models, Reliability testing

- Model Order Reduction, Metamodels, Surrogate Models of Finite Element Methods (FEM) or any other Physical Model

Figure 4.2: Prognostics and Health Management main topics.

This chapter proposes unique algorithms to handle the stress sensor data obtained from the ECU to recognize in-situ failure. The proposed algorithms are presented after briefly describing the sensor, the raw data, and numerical simulation. The implementation results are followed using the data obtained from a test vehicle.

4.1. IFORCE SENSOR

The piezoresistive silicon-based stress sensor is constructed of MOSFET transistors in the current mirror configuration to measure the stress and the temperature locally. The measuring principle is based on measuring the resistance, which is a function of the electron's mobility inside the silicon crystal.

A more detailed working principle of the piezoresistive silicon-based stress sensor can be found in Refs. [2] and [13]. A land grid array (LGA) package used in this study is shown in Figure 4.3. It is a standard sensor package containing a pair of symmetrically located sensors with 12 sensing cells. Every cell is capable of measuring the in-plane shear stress, σ_{xy}, and the difference of in-plane normal stress components, $D(\sigma) = \sigma_{xx} - \sigma_{yy}$.

The relationship between the measured currents and the stresses are:

$$\sigma_{xx} - \sigma_{yy} = \frac{1}{\pi_{44}^{p}} \frac{I_{OUT} - I_{IN}}{I_{OUT} + I_{IN}} \tag{4.1}$$

$$\sigma_{xy} = \frac{1}{\pi_{11}^{n} - \pi_{12}^{n}} \frac{I_{OUT} - I_{IN}}{I_{OUT} + I_{IN}} \tag{4.2}$$

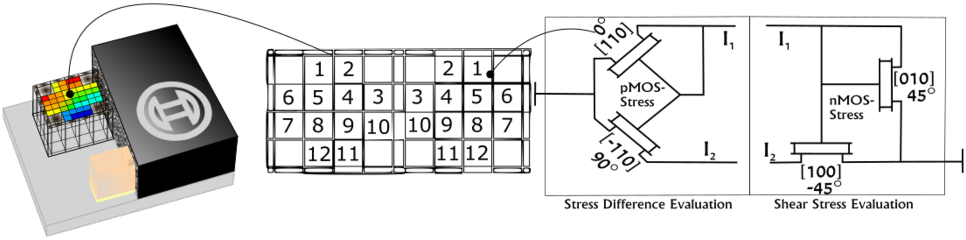

Figure 4.3: Sensor cell numbering in a LGA package. P-mos and n-mos MOSFET channels used to acquire the data.

where π_{11},π_{12},π_{44} are the piezoresistive coefficients of silicon; and I_{IN}, I_{OUT} are the currents measured at the input and output of the sensor, respectively. The stresses can be used to produce the maximum shear stress and the angle of principal stresses as:

$$\tau_{max} = \frac{\sigma_1 - \sigma_2}{2} = \sqrt{(\frac{\sigma_{xx} - \sigma_{yy}}{2})^2 + \tau_{xy}^2} \tag{4.3}$$

$$tan2\theta_p = \frac{2\tau_{xy}}{\sigma_{xx} - \sigma_{yy}} \tag{4.4}$$

Based on the stress equations, 2D Mohr Circle is erected, and the parameter relationship is depicted in Figure 4.4. Mohr circle is a graphical representation of all the stress components captured in one circle.

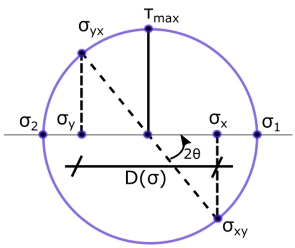

Figure 4.4: 2D Mohr Cicle. Describes the relationship between measured and calculated parameters.

The data collected from one cell during failure propagation represents raw data, two measured parameters, and two calculated parameters as shown in Figure 4.5.

The stress sensor is measuring the mechanical stresses as following :

- Absolute stresses corresponding to current stress of state;
- Relative stresses as a result effect of temperature change;

In this chapter, only the relative stresses are considered, and scaling is applied with zero mean and unit variance.

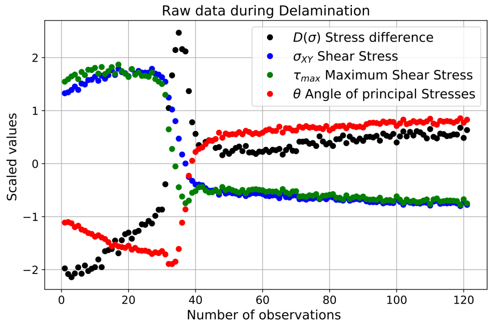

Figure 4.5: Raw data example at room temperature during delamination of the overmolded structure.

4.2. PROPOSED ALGORITHM

The ultimate goal is to develop and implement PHM for various application requirements. Usually, these requirements are projected into a PHM Framework. There are many PHM frameworks proposed in the literature for different applications [14][15]. The principles are, in general, the same for most of them, but for each particular application, PHM frameworks must be modified and optimized for specific requirements.

To successfully measure the stresses from the sensors, an acquisition unit (AU) is required. The designed AU can evaluate the stresses, pre-process the data, extract the features, and assess the health as shown in Figure 4.6. If a failure or anomaly is detected, the data is sent to the Central PHM ECU unit. The gateway can classify the data as being healthy or damaged, in which case resilient actions are taken. The workflow of such a system is presented below.

A typical health dataset, X, contains m rows and p columns, where m is the total number of observations before observing any anomalies and p the total number of the performance parameters. Each sensor output having 12 cells and four parameters can have up to 48 performance parameters. The first part of the algorithm starts with extracting and creating an initial healthy baseline and assessing the health at every measurement step. If no deviations are detected at that particular data point in time, the healthy baseline is updated as shown in Figure 4.7.

In this study, Mahalanobis Distance (MD)[11][16] is employed to assess the health or to detect any anomalies. It is also called quadratic distance, as it can measure the difference between two sets of data and the distance between a point and a set of data. Although effective, it could detect false signals (e.g., outliers, changes not associated with damage, etc.). An additional step that quantifies the damage is added to avoid false detection. Let us assume that an anomaly is detected at the nth observation. To assure that this detection point is not an outlier, another set of measurements should be conducted at $n+h$, where h depends on the number of performance parameters. A new dataset, Y, is created, containing h rows and p columns. On this newly created dataset h by p, a correlation matrix is constructed. This correlation matrix is assumed to be the failure correlation matrix, and it is compared with the healthy baseline correlation matrix used in the MD method. This is possible with Fisher $r-to-z$ transformation [17], which assesses the significance of the difference between two correlation coefficients.

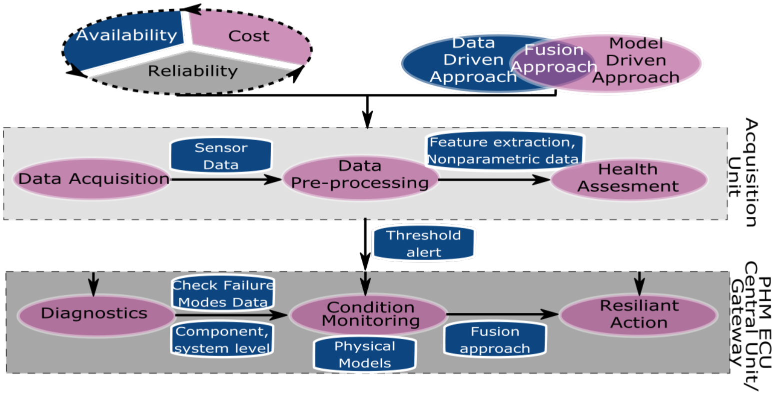

Figure 4.6: Prognostics and Health Monitoring framework.

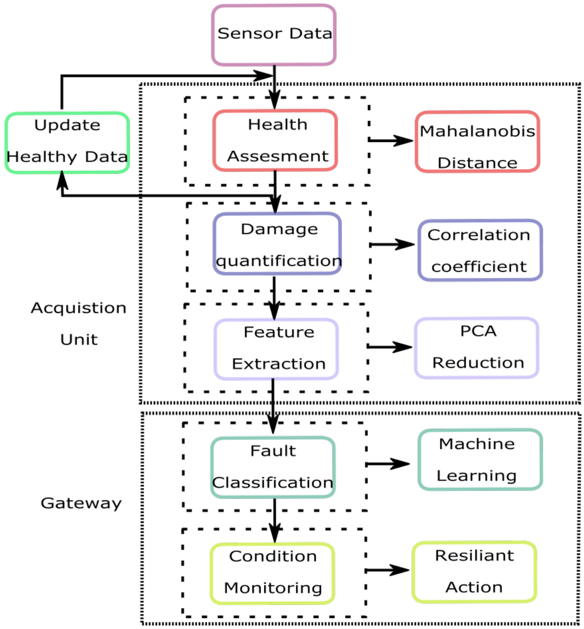

Figure 4.7: Algorithm flowchart.

If the significance of the difference is close to zero, the probability of two sets being similar is very high. If the z value is around one, the likelihood of these datasets being similar is less than 0.05. This additional step is checking if the data points are outliers, and it can quantify the damage by estimating the $z-scores$ of the performance parameters.

As an intermediate step, PCA (Principal Component Analysis) is used for the data reduction to facilitate cheaper and faster transmission [18]. Another main advantage of PCA is that it is used to extract features by highlighting the patterns from the data. This step is performed only if MD detects any anomaly and if the significance of the difference between two correlation coefficients is at least equal to one. In this way, indeed, the detection point is not an outlier but an entire dataset different from the healthy baseline.

The extracted features are then used to classify the data by using Support Vector Machines (SVM). The data is divided into training, and testing datasets in about 70/30% used to validate the classification model.

4.3. IMPLEMENTATION

4.3.1. TEST VEHICLE

The test vehicle used in the study is shown in Figure 4.8, and it represents an Outer molded ECU.

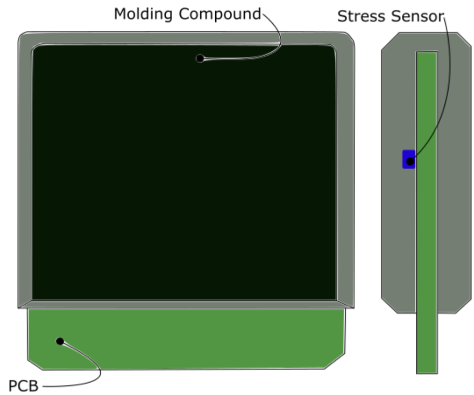

Figure 4.8: Geometry representation of the Outer molded electronic control unit.

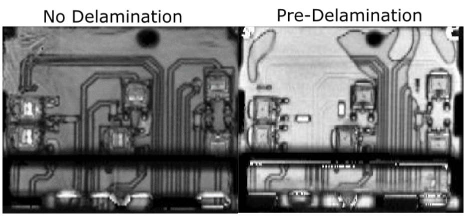

Figure 4.9: Process intended pre-delamination. The left sample follows a standard packaging process, whereas the right sample has delamination created before the injection molding process.

It consists of six DPAK's and three stress sensors mounted on the top and bottom sides of a PCB as shown in Figure 4.10. An injection molding process molded this assembly. The location of the sensors was chosen to capture the maximum stress. Every sensor package contains two symmetrical sensors. Their locations and their arbitrary numbering are presented in Figure 4.10.

The study was performed on ten samples, but the results are shown from the most significant two samples considering a large amount of data. The most probable failure

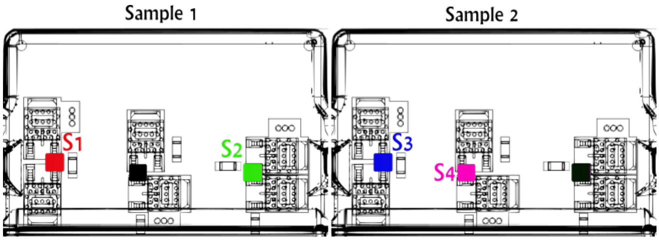

Figure 4.10: The position of each sensor on the Outer molded electronic control unit.

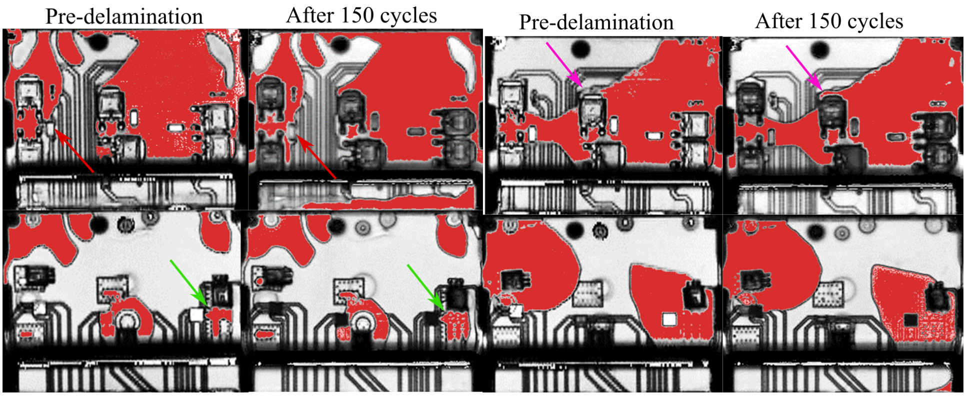

(a) Sample 1. The red and green arrows indicates the areas where there are changes in the delamination.

(b) Sample 2. The magenta arrow indicates the area where there are changes in the delamination area.

Figure 4.11: SAM images of the initial delamination and the delamination propagation after 150 cycles.

is located at the interface between the molding compound and the PCB. Therefore some initial delamination was created on the samples during the injection molding process as shown in Figure 4.9. The pre-delamination areas are visible in the initial SAM images as shown in Figure 4.11. The locations of delamination are randomly distributed. The delamination is present in the vicinity of sensor 3 (S3) on both sides of the PCB of Sample 2. Thus, as expected, the most damage should be recorded by sensor S3 of Sample 2.

The delamination is represented by the area in red color and the lack of visibility of the circuit board footprint, as shown in Figure 4.11.

4.3.2. Initial Data

Data was recorded through an acquisition system during the experiments. The samples were placed in a temperature chamber, and they were exposed to a passive cycling loading condition of -40° C to 125° C with a dwelling time of 15 minutes as shown in Figure 4.12. The dwelling time was predetermined to provide a condition where all components reach the uniform distribution at target temperatures. SAM images of the samples were recorded before and after every 150 cycles.

A predictive FEM model investigated the sensor signal. The geometry and the load-

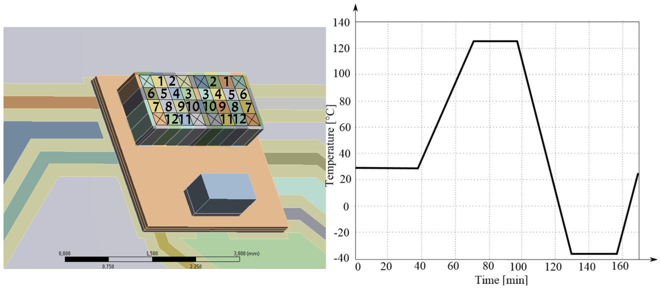

Figure 4.12: Stress sensing cells FEM simulation and the loading conditions.

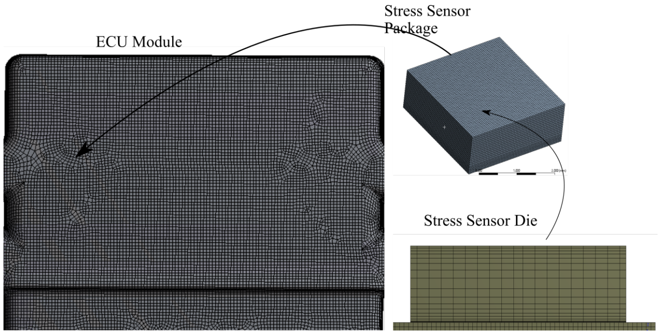

Figure 4.13: Numerical Simulation mesh.

ing conditions are identical to the experiment, as shown in Figure 4.12. The stress difference and the shear stress are evaluated at the exact location as in the experimental case. The process to validate the model can be found in Ref. [19].

The simulation material models used are linear elastic and linear viscoelastic, with their properties shown in Table 6.1. The stresses are the derivative of the load; therefore, reaching a good agreement between numerical simulation and experiment is very sensitive. Accurate material models and material properties are the keys to getting such an agreement. Except for this and the geometry itself, an essential part of the FEM modeling is the discretization.

A mesh study is performed, in which the desired stress locations mesh are not influenced by the size anymore. The element type is a higher-order with middle nodes. Thin elements with ratio aspects considered are distributed on the top and bottom of the die to reduce the mesh dependency on the evaluated values. Also, for the die attach, three mesh partitions are considered in the out-of-plane direction. The final mesh used for numerical simulation is shown in Figure 4.13.

The modeling predictions are compared with the experimental data in Figure 4.14. The results show very good agreement. The slight deviations are attributed to the uncertainties of the stress sensor [20] and the material properties used in the simulation.

The repeatability of measurements is known to be 0.3 MPa, and sample-to-sample variations are 2 ... 6 MPa. From these graphs, it is identified the sensitivity of each cell

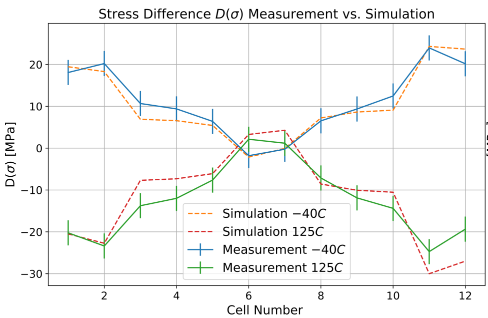

(a) Stress Difference $D(\sigma)$ Measurement vs. Simulation.

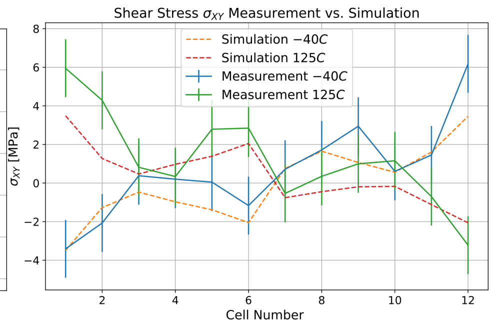

(b) Shear Stress σ_{XY} Measurement vs. Simulation.

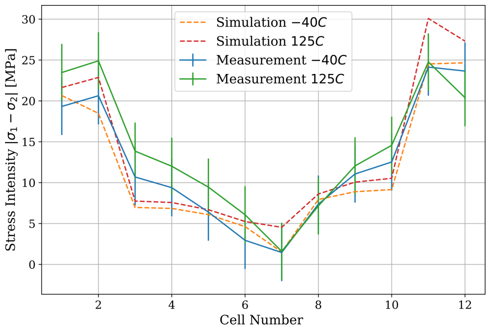

(c) Maximum Shear Stress τ_{max} Measurement vs. Simulation.

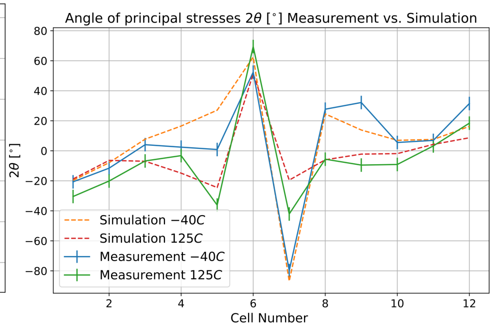

(d) Angle of principal stresses $2\theta[^\circ]$ Measurement vs. Simulation.

Figure 4.14: FEM examination of the test vehicle. The measurement stress corresponds to relative stress.

in the healthy stress state. It is clear that from all the parameters, cells 1, 2, 11, and 12 have the highest deviation between different loading conditions. The higher stress state is located in the outer areas of the chip. This observation is essential for further development of the stress sensor and also for data reduction strategies.

The simulation data is used to examine the measurements. It provides a better understanding of the mechanical processes and ultimately helps develop a prognostics physical model. Simulation data can further be used for model-based fault detection by considering the residuals, which can be utilized to classify different failure mode's behavior.

4.3.3. Data from Thermal Cycling Data

Between the first and the 50th cycle (between 0 and 1800 measured points), changes in the stress difference and shear stress were observed as shown in Figure 4.15 followed by constant values. Some of these changes are recorded till around the 50th cycle, and the results are depicted in Figure 4.17. There are changes in stress difference in both sensors S1 and S2 from Sample 1. The sample and the red circle corresponding to the

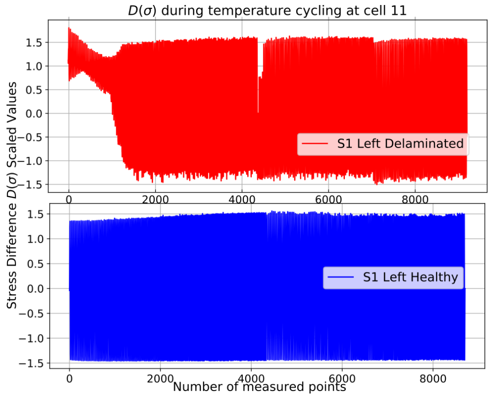

Figure 4.15: Stress evolution of the delamination during temperature cycling of the Sample 1 S1 cell 11 in comparison of the same sensor in a healthy ECU with the same conditions.

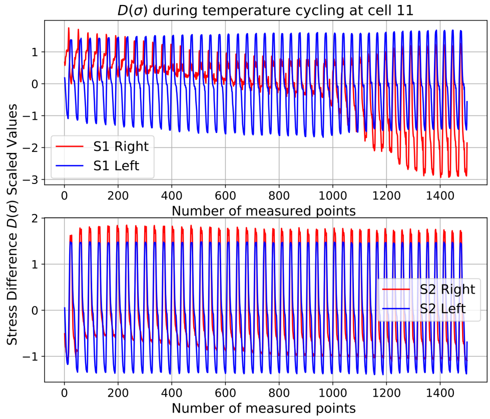

Figure 4.16: Stress evolution of the delamination during temperature cycling of the Sample 1.

delamination propagation can be visualized in Figure 4.11.

From the same interval of cycles, it can also be observed a change in the difference of stress for sensor S4 from Sample 2 as depicted in Figure 4.17. The sample and the magenta circle representing the delamination propagation can be visualized in Figure 4.11.

The corresponding shear stress from the interval of cycles described above it can also be observed a change for sensor S1 and S2 from Sample 1 as depicted in Figure 4.18. The sample, the red arrow, and the green arrow representing the delamination propagation can be visualized in Figure 4.11.

Due to the complexity of the structure and a large amount of data, it is challenging to interpret it quantitatively. Several algorithms, such as statistical pattern recognition methods and machine learning techniques, are considered to analyze the data.

The corresponding shear stress of Sample 2 is depicted in Figure 4.19. In both sam-

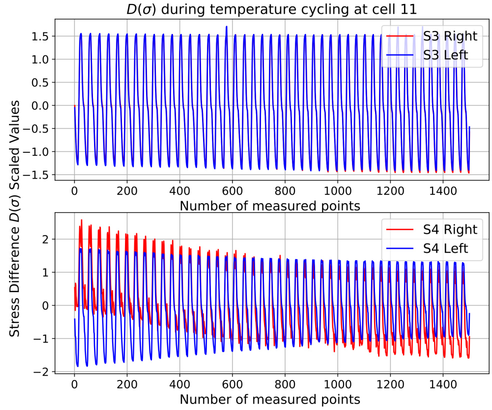

Figure 4.17: Stress difference evolution of the delamination during temperature cycling of the Sample 2.

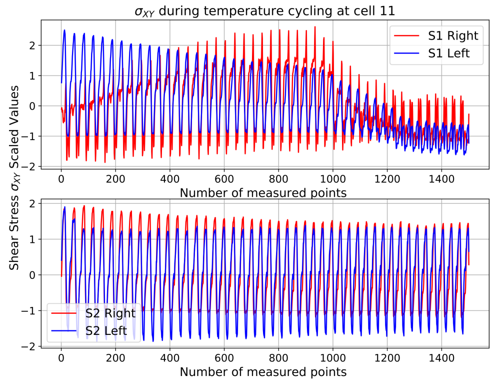

Figure 4.18: Shear Stress evolution of the delamination during temperature cycling of the Sample 1.

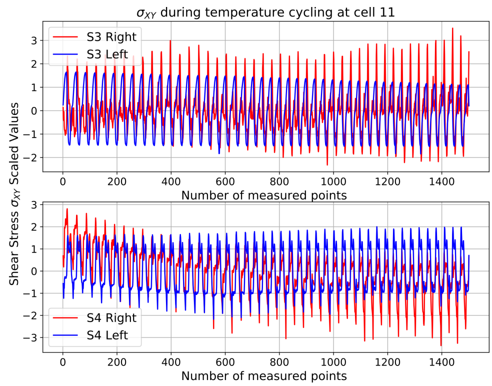

Figure 4.19: Shear Stress evolution of the delamination during temperature cycling of the Sample 2.

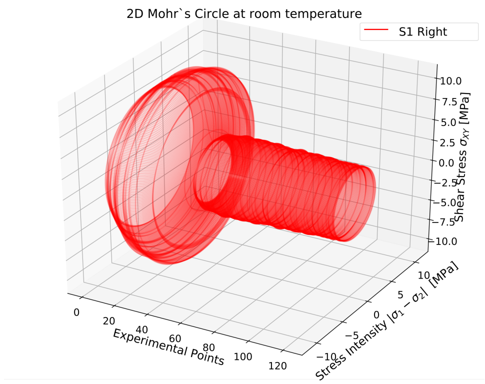

Figure 4.20: This is a representation of the 2D Mohr‘s Circle of the data acquired during the experiments at cell 2 Sample 1 during delamination.

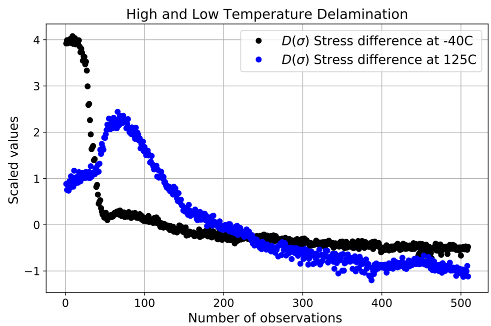

Figure 4.21: Stress Difference evolution during delamination at 125°C and -40°C. More visible changes in stress values are present at low temperature.

ples, there were changes in both components of stress. Therefore it is clear that the sensor is sensitive to physical changes in the vicinity material.

Mohr’s circle values were plotted during the delamination, to capture both parameters in one graph. The results are shown in Figure 4.20, where the radius and the diameter represent the maximum shear stress and the difference of the principal stresses, respectively.

It is clear from Figure 4.20 that the diameter increases first and decreases rapidly after approximately 30 cycles. In the author’s opinion, the energy release associated with crack propagation may be attributed to the diameter reduction.

At low temperatures (in this case -40°C), the stress state is higher because of the large ΔT from the stress-free point temperature (180°C). Therefore, any change in stress state can be more visible. In addition, the brittle behavior at low temperatures can accelerate the delamination. One such example can be observed in Figure 4.21.

4.3.4. Failure Analysis by SAM

As shown in Figure 4.11, changes in the delamination area were observed after 150 cycles. The pictures shown reveal two essential properties which should be contained in the data as well. The first property is represented by the fact that the samples have an a priori delamination. The second property by the change in the delamination area due to the damage progress.

These properties correspond to the data by the stress value differences from the healthy samples and the ongoing stress change after the cycle 35-50.

4.3.5. Data understanding using visual analytics

A crucial step is to understand which readings of the sensor cells in the sensor package are most relevant to capture the damages. To do so, techniques from the field of visual analytics [21] were used to visualize the different effects of measurements from healthy and damaged states.

For this purpose, parallel coordinates [22] were used, which was previously used for fault detection, e.g., in Relating n dimensions is done by drawing n parallel vertical axes. Each dimension's value is mapped to its axis, where low values are at the bottom. These values on the axes are then connected by line segments resulting in m lines, where m is the number of readings.

Using parallel coordinates, the readings from the 12 sensing cells of the sensor package (see Figure 4.3) were correlated. In addition, the x-axis holds an index, and the y axis holds the information of whether the damage was present, where damages are shown in red, and measurements from the normal mode in green. The visualization is shown in Figure 4.22.

From the plot, it can be deduced which features capture the damages. The measurements of the different damages are spread over most of the features. However, it can be seen that some individual dimensions are clearly affected by the damages: A clear separation between normal and damage is possible based on the sensor cells V1, V2, V11, V12, with stress difference values, i.e., these sensor cells captured the effect of the damages.

4.4. Data Analysis by the Proposed Algorithm

4.4.1. Health Assessment

For computing MD, the sets of compared data do not need to have the same rows. In this study, rows refer to the number of observations and create the possibility of comparing the healthy dataset with just one failure measurement point. This is convenient in health monitoring, considering that many other methods require specific observation points.

In this approach a healthy baseline and a threshold are needed to classify the product states (healthy or unhealthy). Several steps are required to calculate MD as follows:

- Step 1. Calculate the average of each column

$$\bar{x}_i = \frac{1}{m}\sum_{j=1}^{m} x_{ij} \tag{4.5}$$

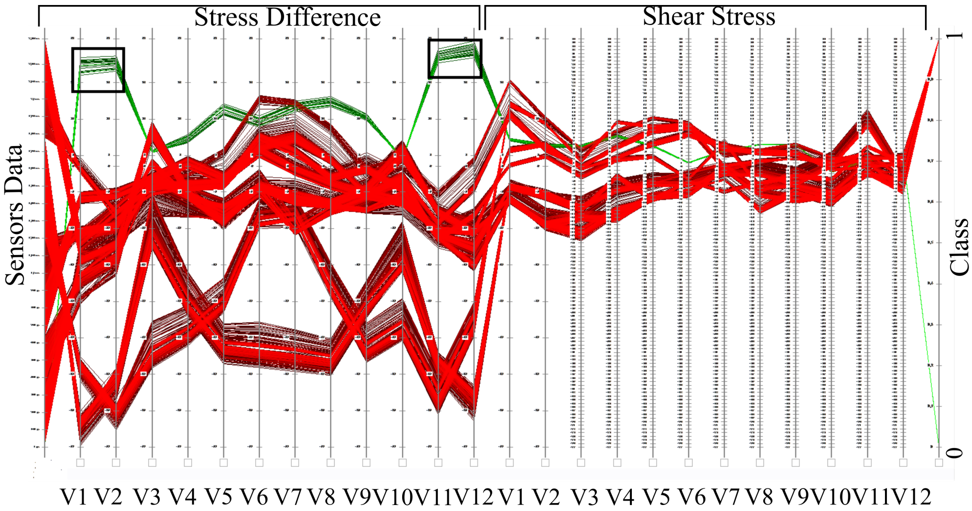

Figure 4.22: The effect of damages on the different sensor readings is shown with parallel coordinates, where the readings of 12 sensor cells are related. It can be seen that the sensor cells V1, V2, V11, V12 with stress difference values capture the effect of the damages (marked with two rectangles).

- Step 2. Calculate the standard deviation

$$S_i = \sqrt{\frac{\sum_{j=1}^{m}(x_{ij} - \bar{x}_i)^2}{m-1}} \tag{4.6}$$

- Step 3. Normalize the values

$$Z_{ij} = \frac{x_{ij} - \bar{x}_i}{S_i} \tag{4.7}$$

- Step 4. Correlation matrix

$$C = \frac{1}{m-1}\sum_{j=1}^{m} z_j z_j^T \tag{4.8}$$

- Step 5. Mahalanobis Distance

$$MD_j = \frac{1}{p} z_j^T C^{-1} z_j \tag{4.9}$$

The next step is to add the subsequent measurement's normalized values and compute the MD keeping the same correlation matrix from the healthy baseline. If the measurement point does not exceed the threshold, it is added to the healthy correlation matrix.

For threshold determination, a probabilistic approach is used. Since the MD are not normally distributed, a Box-Cox transformation [14] is used to convert the data into a

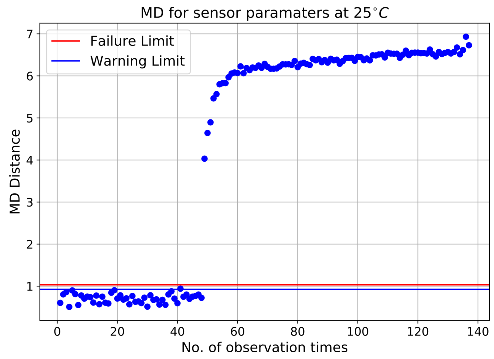

Figure 4.23: Mahalanobis Distance calculated over the 12 cells of the Sample 1 S1. The healthy base is established on the first measurements and every point in measurement is calculated. In this graph there is changes due to the delamination showed in Figure 4.11.

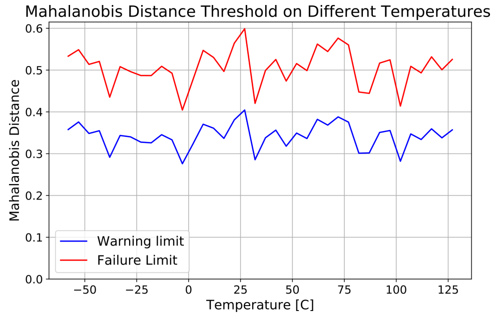

Figure 4.24: Threshold Evaluation performed at all temperatures. Based on this graph a mean can be computed to represent the temperature independent threshold.

normal distribution. A warning limit threshold is defined as $(\mu + 2\sigma)$ and a fault alarm threshold as $(\mu + 3\sigma)$, based on the normal distribution parameters.

The healthy baseline should have more rows than columns, considering that the rows represent the number of measurements and columns the number of parameters. For assuring good results, it is recommended that the ratio m/p should be as high as possible. Otherwise, the outliers can shift the sample mean and inflate the correlation matrix [23].

A representative MD for both stress components is shown in Figure 4.23. The healthy baseline is created on the first 35 measurement points. The data points exceeding the failure limit are seen in the MD results. The incidents are expected from the raw data (Figure 4.5). Still, the MD results provide a more definitive health state of the specimen through the multi-variate to uni-variate conversion.

The threshold at different temperatures is computed from the healthy data (i.e., no initial delamination), and the result is plotted in Figure 4.24. The threshold does not change with the temperature, implying that the healthy baseline can be created at any temperature.

MD method is preferred for fault/anomaly detection because of its advantages re-

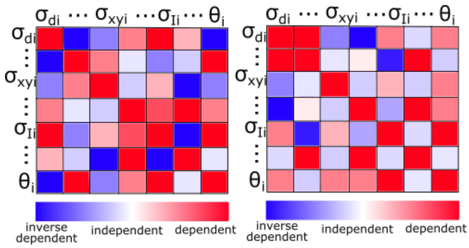

Figure 4.25: Healthy baseline Correlation Matrix vs. Outlier baseline Correlation Matrix.

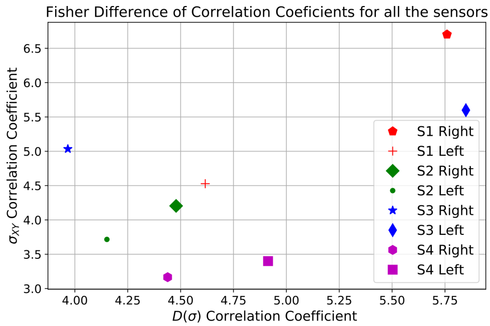

Figure 4.26: Fisher Correlation Coefficient Difference. This difference is performed by using Fisher method of comparing two correlation coefficients. In this case all the sensors correlation coefficient data have been compared with the correlation coefficient as healthy state. The values from the graph represents the z-score values.

lated to the requirements in health monitoring; they include fast calculation, no failure data required, single measurement point required, and temperature-independent threshold.

4.4.2. DAMAGE QUANTIFICATION

This step is necessary to overcome the possibility of detecting outliers or changes in stress values that are not associated with any damage.

In this subsection, the correlation matrix of the healthy baseline without initial delamination is compared with the correlation matrix of a potential failure dataset as shown in Figure 4.25. As previously mentioned, a new correlation matrix is calculated based on the measurement points after the threshold is exceeded.

The sampling distribution of the healthy and faulty correlation coefficient matrices does not follow a normal distribution. Fisher r-to-z transformation is used to convert these data sets into a normally distributed variable z. This transformation is made as follows:

$$z_r = \frac{1}{2} log\left(\frac{1+r}{1-r}\right) \tag{4.10}$$

This transformation is performed at a confidence value interval of 0.95. Each correla-

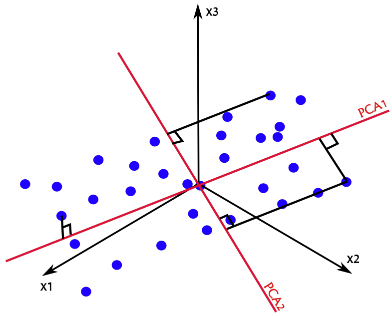

Figure 4.27: A simplified visual representation of the reduced space. Orthogonal projections on the new reduced principal components are depicted.

4

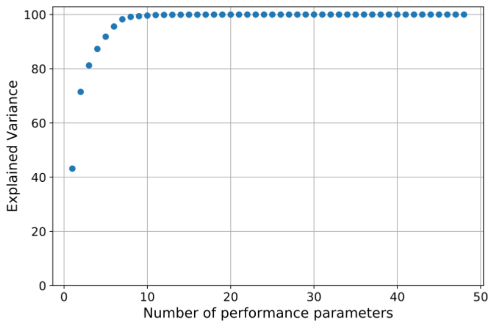

Figure 4.28: Explained variance. It measures the proportion to which PCA model accounts for the data variation.

tion coefficient parameter in the data is compared with the correspondent one, and then a mean is performed on the stress difference and shear stress performance parameters.

Plotting them against each other is depicted in Figure 4.26. From this graph, it is concluded that some sensor data is more damaged than others. The most damaged one is shown in blue representing the Sample 2 sensor S3. From Figure 4.11 it is observed that the outer molding compound is delaminated from the package of sensor S3.

4.4.3. Feature Extraction

PCA is used to identify patterns in data of high dimension and to express the data to highlight their similarities and differences [18]. Also, this last step is performed to reduce the data as much as possible, understand the data much better, and make the classification much easier to perform.

Another main advantage of PCA is finding the patterns in data by reducing the number of dimensions without much loss of information (see Figure 4.27). This technique is advantageous in the case of linking the stress sensor data to the failure.

The PCA analysis is performed on the data matrix, followed by extracting the explained variance as shown in Figure 4.28. Only the principal components exceeding 97% of the variance are kept. Therefore only six principal components are enough to perform

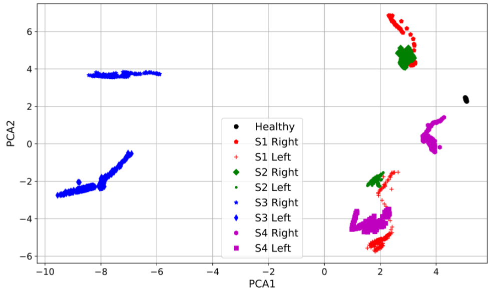

Figure 4.29: Principal components influence over the delamination areas.

PCA analysis, and the extracted results of each performance parameter influence on the principal components are shown in TABLE 5.1. It is observed that the weight of each parameter reveals that the first component takes the most influence from stress difference performance parameters, and the second component takes the effect from shear stress performance parameters.

The contribution of stress difference and shear stress in the delamination process is visualized in Figure 4.29. Again as previously observed, the blue markers representing sensor S3 from Sample 2 are the most damaged.

The sensor symmetry is identified from Figure 4.29 and Figure 4.30. The behavior of the sensors in both figures is quite similar but with opposite signs. A classification strategy can be implemented, considering the data from one sensor as training data and the data from the other sensor as validation. Briefly a PCA is performed as follows:

- Step 1. Subtract the mean

$$\bar{x_i} = \frac{1}{m}\sum_{j=1}^{m} x_{ij} \tag{4.11}$$

- Step 2. Calculate the covariance matrix

$$cov(x_i, x_j) = \frac{\sum_{i,j}^{n}(x_i - \bar{x})(x_j - \bar{x})}{n-1} \tag{4.12}$$

- Step 3. Calculate the eigenvectors and eigenvalues of the covariance matrix

- Step 4. Choosing the eigenvectors with the highest eigenvalue

- Step 5. Reconstructing the data matrix with the new set of parameters

With the data reduced to 6 performance parameters, it can be furthered used for transmitting the data. The transmitted data can be reconstructed in the initial number of parameters, or it can be used as it is. The classification methods can use both datasets.

In Figure 4.29 the most dominant principal components are depicted, reducing the high dimension of the data to these two components makes it easier to understand the

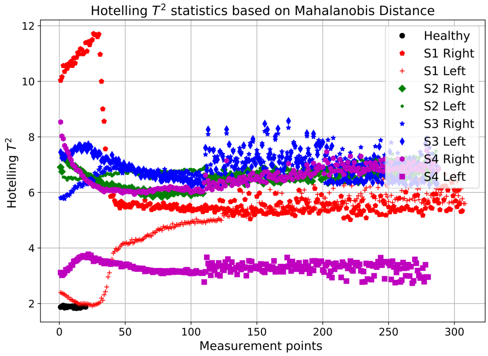

Figure 4.30: Hoteling T2 statistics in the reduced space at room temperature during delamination. The red line corresponding to the same sensor but mirrored can identify a similar behavior, but opposite sign.

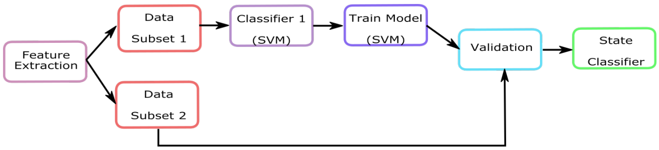

Figure 4.31: Classification Method. The data is divided into two datasets, one used for training and the other one for testing.

global influence of different delamination areas on the stress difference and shear stress components.

As expected, the S3 left and right data from Sample 2 shows the most significant distance from the healthy baseline at least in the first component axis, represented in most part by the stress difference component.

Based on the reduced space Hoteling T2 statistics is performed and is depicted in Figure 4.30. In this graph, the stresses reach a high peak. Then there is a drop, which confirms our previous observations that there is an increase in the stress state before the delamination, followed by a decline representing the physical delamination.

4.4.4. FAULT CLASSIFICATION

For the discussed research to be put into practice, an autonomous approach is required to classify new data as "healthy" or "damaged" and hence resilient actions, e.g., during life-cycle. For that purpose, machine learning techniques are used, i.e., data-driven approaches that learn from a training set. In the following sections, one-class support vector machines are discussed, and the experimental results are reported.

ONE-CLASS SUPPORT VECTOR MACHINES

Support vector machines (SVM) are a set of machine learning methods that can be applied to structural damage detection due to their ability to form an accurate boundary from a small amount of training data [24]. SVM is a technique of finding a plane separating two classes in a data set by maximizing the distance between the separating hy-

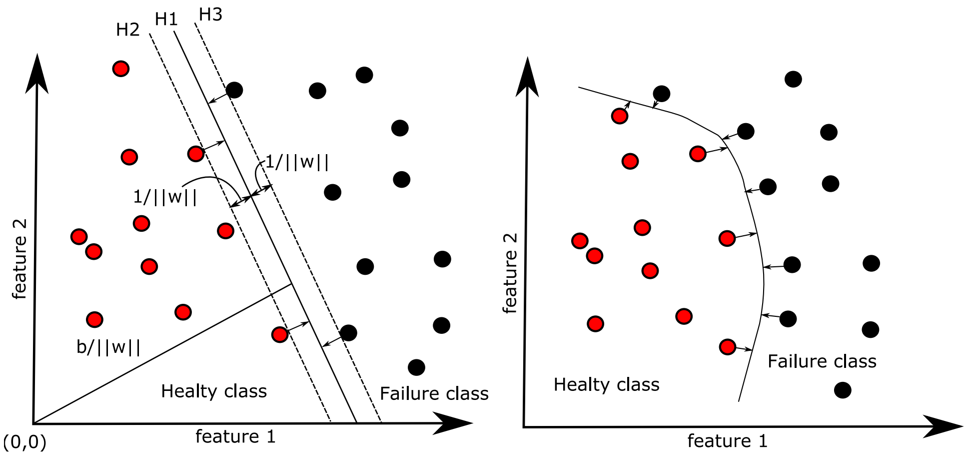

Figure 4.32: Illustration of a linear and a non-linear decision boundary of a one-class support vector machine.

perplane and the classes. During the training, the best hyperplane in the given feature space is determined, which maximizes the distances between classes.

Essentially SVMs are two-class classifiers, i.e., they need samples from two classes. For this work, this would be samples from a healthy state and damaged ones. Damage classification can be done in a two-class classification setup, i.e., a training set from the healthy and damaged state is required. However, this assumes knowledge about all potential damages, which is unlikely to exist in practice. So in case of an unrepresentative set of damages in the training set, the classifier will have a bias towards detecting these damages that it was trained on. So in this work, a one-class classification setup was used, where solely data from the healthy state is used to train the classifier, and test data deviating from the training set is reported as an anomaly, i.e., potential damage.

This can be achieved with a special case of an SVM, a one-class support vector machine (OC-SVM). There are two major variants of OC-SVMs: ν-SVM proposed in [25] and support vector data description (SVDD) proposed in [26].

The ν-SVM uses a hyperplane to separate normal samples and outliers, where the position of the hyperplane is controlled by the parameter ν. One example of a linear hyperplane is depicted in Figure 4.32 a.

In general, SVMs classify by considering the hyperplane $H1$ written as $wx + b = 0$, where w is normal to the hyperplane and x are the points which lie on the hyperplane. All samples in the training set must satisfy the following constraints, where y_i is the class label and b is a bias:

$$x_i w + b \geq +1 \quad for \quad y_i = +1 \tag{4.13}$$

$$x_i w + b \leq -1 \quad for \quad y_i = -1 \tag{4.14}$$

These constraints are combined into one inequality:

$$y_i(x_i w + b) - 1 \geq 0 \tag{4.15}$$

The distance between $H1$ and $H2$ is $d_+ = 1/||w||$ and the margin is simply $2/||w||$. Considering that $H2$ and $H3$ are parallel, the optimization problem needs to minimize $||w||^2$, which is subject to constraints.

While two-class support vector machines and ν-SVM [25] separate the data by a hyperplane, SVDD [26] finds a hypersphere around the normal samples in the training set. SVDD was used for fault detection in the automotive domain in [27, 28].

The hypersphere is described by its radius R and its center a and is found by solving the optimization problem of minimizing

1. the error on the normal class, i.e. on samples from healthy state
2. the probability of misclassifying measurements from damages

Minimizing the error on data from the normal class is achieved by tuning R and a in a way that all samples of the training data set are contained in the hypersphere. With no data from damages present in the training data, the probability of misclassifying measurements from damages cannot be directly minimized. This is implicitly achieved by minimizing the hypersphere's volume, assuming this reduces the risk of misclassification.

This trade-off between the number of misclassified samples from a healthy state and the volume of the hypersphere is optimized by minimizing

$$F(R, a) = R^2 \tag{4.16}$$

subject to

$$\|x_i - a\|^2 \leq R^2 \quad \forall i \qquad i = 1, .., N \tag{4.17}$$

where x_i denotes the samples and N the number of samples in the training set, a is the center of the hypersphere, and $\|x_i - a\|$ is the distance between x_i and a.

Selected samples describe the found hypersphere from the training set, the so-called support vectors. The remaining samples are discarded.

To make SVDD more robust against undesired outliers in the training set, slack variables ξ_i are introduced, which allow for some samples of the training set to be outside the hypersphere. The parameter C controls the influence of these slack variables and thereby the error on the healthy data. Introducing the slack variable turns eq. 4.16 and eq. 4.17 into minimising

$$F(R, a, \xi_i) = R^2 + C \sum_{i=1}^{M} \xi_i \tag{4.18}$$

subject to

$$\|x_i - a\|^2 \leq R^2 + \xi_i \quad \forall i \tag{4.19}$$

and

classifier	bal. acc.	d_{damage}	p_{damage}
linear ν-SVM	70.0 %	87.0 %	84.2 %
ν-SVM RBF	99.6 %	100 %	99.7 %
SVDD	99.8 %	100 %	99.8 %

Table 4.1: Results for one-class classification with different types of one-class support vector machines.

$$\xi_i \geq 0 \quad \forall i \tag{4.20}$$

This constrained optimization problem is transformed using the method of Lagrange [26] and then solved as a convex optimization problem. In this form, SVDD is only capable of separating the data by a true hypersphere. Analogous to standard SVMs, SVDD, as well as ν-SVM, uses the kernel trick [29] to overcome this inflexibility, i.e. the data is transformed to a higher-dimensional space where it can be surrounded by a hypersphere, using a mapping function $\phi()$. An illustration of a hypothetical non-linear decision boundary is shown in Figure 4.32 b. Instead of actually mapping each instance to a higher-dimensional space, the kernel trick is to replace the inner products of the mapped feature vectors $\phi(x_i)\cdot\phi(x_j)$ by a kernel function $K(x_i, x_j)$ and then applying this kernel function. In this work, the radial basis function (RBF) kernel is used, which introduces the kernel width σ as an additional hyperparameter:

$$K(x_i, x_j) = e^{-\frac{\|x_i - x_j\|^2}{\sigma^2}} \tag{4.21}$$

EXPERIMENTAL RESULTS

For the experiments, the following variants of one-class SVMs are used: linear ν-SVM, ν-SVM with RBF kernel, and SVDD with RBF kernel. It has been shown in [26] that for the RBF kernel, SVDD and ν-SVM yield equivalent solutions. Different hyperparameters cause minor differences in the results. While one-class SVM can yield good classification results for the optimal parameter set, poorly chosen parameters massively decrease the classification accuracy.

For the linear and the kernel-variant of ν-SVM, the parameter ν was set to $\frac{1}{N}$, where N is the number of samples in the training set. For SVDD the parameter C is set to 1, which is a good starting point when no outliers are expected in the training set [30]. The RBF kernel parameter σ is set to $\sqrt{D}$ for SVDD and ν-SVM with RBF kernel, where D is the number of features.

Training the SVMs is solely done on a training set of data from a healthy state. Prior to training, the input features are normalized using a z-score. The normalization factors are applied to the test set, i.e., the test data is not used in any step of pre-processing the data. The test set contains data from healthy states and damages.

The classification results are reported in Table 4.1, where the following measures are reported: the balanced accuracy which is the overall accuracy considering the ratio of the classes, the damage detection rate d_{damage} which is the percentage of samples correctly classified as damage and the precision p_{nov} which shows the percentage of true damages in the subset of samples reported as damages, i.e. $p_{damage} = \frac{\text{true damages}}{\text{reported damages}}$.

It should be noted that the classification problem is not as trivial as it seems in Figure 4.29, since for the PCA, data from healthy and damaged units are used. Classification is done by solely considering data from a healthy state. Otherwise, the solution would be biased towards the sample damages.

As can be seen in Table 4.1, the linear ν-SVM detects 87 % of the damages at a precision rate of 84 %. The two non-linear one-class SVMs detect all damages while misclassifying a low number of normal data as damage, as can be seen by the precision of 99.7 % and 99.8 %, where SVDD has a slightly better classification rate. Conclusively, the results indicate that such an approach can be put into place in various setups in automotive and other industry sectors.

4.5. CONCLUSION

It has been demonstrated that the piezoresistive silicon-based stress sensor can detect, quantify, and classify delamination. Also, the resulting data shows the symmetry of the sensors. The algorithms applied to the sensor data revealed valuable information that can be furthered studied.

A proposed condition monitoring is successfully developed to recognize in-situ failure in order to trigger resilient actions. The results of the machine learning approach show a robust detection rate, indicating that the proposed approach can be put into practice in industrial applications. Using a data-driven approach can be quickly adapted to new setups.

Due to the complexity of how the data collected from the stress sensors are changing during a delamination process, it remains a challenge to interpret the raw data. Further research studies will be performed on the importance of the new parameters and their connection to the failure, the slope registered at the temperature cycling during delamination and the possibility to build a prognostic model based on the damage quantification parameter. Also, a controlled delamination process is needed to create a clear correlation with the collected data.

REFERENCES

[1] A. Prisacaru, A. Palczynska, A. Theissler, P. Gromala, B. Han, and G. Q. Zhang, *in situ failure detection of electronic control units using piezoresistive stress sensor,* IEEE Transactions on Components, Packaging and Manufacturing Technology **8**, 750 (2018).

[2] J. C. Suhling, R. C. Jaeger, and others, *Silicon piezoresistive stress sensors and their application in electronic packaging,* **1**, 14.

[3] P. Gromala, S. Fischer, T. Zoller, A. Andreescu, J. Duerr, M. Rapp, and J. Wilde, *Internal stress state measurements of the large molded electronic control units,* in *Thermal, Mechanical and Multi-Physics Simulation and Experiments in Microelectronics and Microsystems (EuroSimE), 2013 14th International Conference on* (IEEE) pp. 1–8.

[4] T. Schreier-Alt, K. Unterhofer, F. Ansorge, and K.-D. Lang, *Stress analysis dur-*

ing assembly and packaging, in *Electronic Components and Technology Conference (ECTC), 2011 IEEE 61st* (IEEE) pp. 1684–1690.

[5] A. R. Adli and K. Jansen, *Numerical investigation and experimental validation of residual stresses building up in microelectronics packaging,* **62**, 26.

[6] T. Schreier-Alt, G. Chmiel, F. Ansorge, and K.-D. Lang, *Piezoresistive stress sensor for inline monitoring during assembly and packaging of QFN,* in *Electronic Components and Technology Conference (ECTC), 2013 IEEE 63rd* (IEEE) pp. 2126–2131.

[7] F. Schindler-Saefkow, F. Rost, A. Rezaie-Adli, K. M. B. Jansen, B. Wunderle, J. Keller, S. Rzepka, and B. Michel, *Measuring the mechanical relevant shrinkage during in-mold and post-mold cure with the stress chip,* in *Thermal, mechanical and multi-physics simulation and experiments in microelectronics and microsystems (eurosime), 2014 15th international conference on* (IEEE) pp. 1–5.

[8] Y. Kim, H. Lee, S. Park, and X. Zhang, *Stress relaxation test of molding compound for MEMS packaging,* in *Thermal and Thermomechanical Phenomena in Electronic Systems (ITherm), 2012 13th IEEE Intersociety Conference on* (IEEE) pp. 290–296.

[9] A. Palczynska, P. J. Gromala, D. Mayer, B. Han, and T. Melz, *In-situ investigation of EMC relaxation behavior using piezoresistive stress sensor,* **62**, 58 ().

[10] M. K. Rahim, J. Roberts, J. C. Suhling, R. C. Jaeger, and P. Lall, *MEASUREMENT OF DIE STRESSES DURING THERMAL CYCLING,* .

[11] A. Palczynska, A. Prisacaru, P. J. Gromala, B. Han, D. Mayer, and T. Melz, *Towards prognostics and health monitoring: The potential of fault detection by piezoresistive silicon stress sensor,* in *2016 17th International Conference on Thermal, Mechanical and Multi-Physics Simulation and Experiments in Microelectronics and Microsystems (EuroSimE)* (IEEE) pp. 1–8.

[12] B. Wu, D.-S. Kim, B. Han, A. Palczynska, and P. J. Gromala, *Thermal deformation analysis of automotive electronic control units subjected to passive and active thermal conditions,* in *Thermal, Mechanical and Multi-Physics Simulation and Experiments in Microelectronics and Microsystems (EuroSimE), 2015 16th International Conference on* (IEEE) pp. 1–6.

[13] A. Palczynska, F. Pesth, P. J. Gromala, T. Melz, and D. Mayer, *Acquisition unit for in-situ stress measurements in smart electronic systems,* in *Thermal, mechanical and multi-physics simulation and experiments in microelectronics and microsystems (eurosime), 2014 15th international conference on* (IEEE) pp. 1–4.

[14] M. Pecht, *Prognostics and health monitoring of electronics,* in *Electronic Materials and Packaging, 2006. EMAP 2006. International Conference on* (IEEE) pp. 1–10.

[15] P. Lall, P. Gupta, D. Panchagade, M. Kulkarni, J. Suhling, and J. Hofmeister, *Prognostics and condition monitoring of electronics,* (IEEE) pp. 1–14.

4

[16] S. Kumar, V. Sotiris, and M. Pecht, *Health assessment of electronic products using mahalanobis distance and projection pursuit analysis,* **2**, 242 ().

[17] R. A. Fisher, *Biological monographs and manuals vol-5,* .

[18] H. Anton, *Elementary linear algebra* (Wiley) OCLC: 13580207.

[19] D.-S. Kim, B. Han, A. Yadur, and P. J. Gromala, *Electronic control package model calibration using moiré interferometry,* in *Thermal, mechanical and multi-physics simulation and experiments in microelectronics and microsystems (eurosime), 2014 15th international conference on* (IEEE) pp. 1–5.

[20] A. Palczynska, F. Schindler-Saefkow, P. Gromala, K. Kreyßig, S. Rzepka, D. Mayer, and T. Melz, *Investigation of uncertainty sources of piezoresistive silicon based stress sensor,* **807**, 45 ().

[21] D. Keim, G. Andrienko, J.-D. Fekete, C. Görg, J. Kohlhammer, and G. Melançon, *Visual analytics: Definition, process, and challenges,* in *Information Visualization*, Vol. 4950, edited by A. Kerren, J. T. Stasko, J.-D. Fekete, and C. North (Springer Berlin Heidelberg) pp. 154–175, DOI: 10.1007/978-3-540-70956-5_7.

[22] A. Inselberg, *The plane with parallel coordinates,* The Visual Computer **1**, 69 (1985).

[23] S. Kumar, T. W. S. Chow, and M. Pecht, *Approach to fault identification for electronic products using mahalanobis distance,* **59**, 2055 ().

[24] C. J. Burges, *A Tutorial on Support Vector Machines for Pattern Recognition*, 2nd ed., Vol. pp. 121-167 (Data Mining and Knowledge Discovery, 1998).

[25] B. Schölkopf, J. C. Platt, J. C. Shawe-Taylor, A. J. Smola, and R. C. Williamson, *Estimating the support of a high-dimensional distribution,* Neural Computation **13**, 1443 (2001).

[26] D. M. Tax, *One-class classification. Concept-learning in the absence of counter-examples,* Ph.D. thesis, Delft University of Technology (2001).

[27] A. Theissler, *Detecting anomalies in multivariate time series from automotive systems*, Ph.D. thesis, Brunel University London (2013).

[28] A. Theissler, *Multi-class novelty detection in diagnostic trouble codes from repair shops,* in *In Proc. The 15th IEEE International Conference on Industrial Informatics (INDIN 2017)* (2017).

[29] S. Theodoridis and K. Koutroumbas, *Pattern Recognition, Fourth Edition*, 4th ed. (Academic Press, 2009).

[30] D. Tax and R. Duin, *Support vector data description,* Machine Learning **54**, 45 (2004).

5

Degradation Prediction of Electronic Packages using Data-driven Approach

Recent trends in automotive electronics, such as automated driving, will increase the number and complexity of electronics used in safety-relevant applications. Applications in logistics or ridesharing will require a specific year of service rather than the conventional mileage usage. Reliable operations of the electronic systems must be assured at all times, regardless of the usage condition. A more dynamic and on-demand way of ensuring system availability will have to be developed. This chapter proposes a thermo-mechanical stress-based prognostics method as a potential solution. Several novel advancements achieve the goal. A key microelectronics package is developed on the experimental front to directly apply the prognostics and health management (PHM) concept using a piezoresistive silicon-based stress sensor. Additional hardware for safe and secure data transmission and data processing is also developed, critically required for recording in situ and real-time data. On the data-management front, proper data-driven approaches must be identified to handle the unique data set from the stress sensor employed in the study. The approaches effectively manage the massive amount of data that reveal the important information and automation of the predictive process and thus to be able to detect, classify, locate and predict the failure. The statistical techniques for diagnostics and the machine learning (ML) algorithms for health assessment and prognostics are also determined to implement the approaches in a simple, fast but accurate way within the capacity of limited computing power. The proposed prognostics approach is implemented with actual microelectronics packages subjected to harsh accelerated testing conditions. The results corroborate the validity of the proposed prognostics approach.

Parts of this chapter have been published in IEEE Transaction Industrial Electronics (2021) [1].

5.1. Introduction

Microelectronics packages are composed of multi-layer dissimilar materials with complex geometries. These composite interfaces, corners, and edges are subjected to various loading conditions during manufacturing as well as operation [2]. The packaging technologies protect sensitive electronic components for multiple applications such as telecommunication, automotive, and aerospace.

During operation, the internal stress state changes due to the coefficient of thermal expansion (CTE) mismatch among the materials used in the package and the stress concentrations at material discontinuities, which can cause thermo-mechanical related failures. According to [3] these failures account for more than 65% of the total failures in electronics.

Prognostics is the process of predicting a future state (of reliability) based on current and historical conditions. Prognostics and health management (PHM) is a method that permits the reliability of a system to be evaluated in its actual life-cycle conditions, to determine the advent of failure, and mitigate the system risks [4]. One of the ways to perform prognostics is to measure the mechanical stresses directly using a stress sensor. Such sensor was developed originally to measure the manufacturing stresses [5], but was extended successfully to various applications including transfer molding [6], packaging [7], molding relaxation [8], prognostics [9][10] and condition monitoring [11][12]. In [13] the sensor packaged in a QFN, and the stress field has been recorded after the damage. Although the damage was observed in the stress field, the limitation is that the delamination is imposed apriori. Delamination was also reported in [14]. A flip-chip as an application was used during the reliability testing. While the delamination was successfully monitored, the delamination happened exactly at the sensor interface, and only 11 measuring cells were used.

In the previous related paper, [9], delamination was successfully detected in an overmolded electronic unit test vehicle using such a stress sensor. The propagation of the delamination was also successfully monitored. Yet, the available experimental data was limited (the delamination was apriori imposed), and delamination was correlated with stress data only qualitatively. This is the motivation of the current chapter. Algorithms and techniques for automated degradation estimation and prediction for electronic packages using mechanical stress are not yet reported.

Significantly more data are required to predict the health condition quantitatively. They should be collected from multiple samples, and each sample should provide continuous stress signals from the healthy state to the state of complete failure. The previous approach by which the data is handled manually using a degradation model becomes simply unfeasible for such a large amount of data [9]. For example, raw data for each sample goes up to 2.5 GB for 2500 Cycles. A Finite Element Method validation of the current experiments used in this chapter was performed in [15]. A classical backpropagation neural network was used to estimate the degradation. The results showed that an improved model is needed.

In this chapter, the stress-based PHM capability is extended into a quantitative domain where accurate prediction of remaining useful life (RUL) becomes possible. Several major novel advancements achieve the goal:

- Non-destructive and in-situ detection of the delamination during accelerated testing

- Successful classification of the data obtained from two different failure modes
- Quantitative estimation of delamination location, state of health and degradation of automotive electronic packages using Machine Learning

. An essential microelectronics package to which the PHM concept can be directly applied is developed on the experimental front. Additional hardware for safe and secure data transmission and data processing is also developed, critically required for recording in situ and real-time data. On the data-management front, proper data-driven approaches have to be identified, which fit ideally for a specific stress sensor employed in the study while being able to handle the massive amount of data that reveals the important information and automation of the prognostic process and thus to be able to detect, classify, locate and predict the failure. The statistical techniques for diagnostics and the machine learning (ML) algorithms for health assessment and prognostics are then determined to implement the approaches in a simple, fast but accurate way within the capacity of limited computing power.

In section II, the general PHM framework adopted in this study is introduced. An experimental setup and a test vehicle are described in Section III. Results from actual tests and various strategies for evaluation and processing the data are presented in Section IV. Diagnostics by means of failure detection, location, and classification is shown in Section V. Section VI presents the Health Assessment and Prognostics.

5.2. METHODOLOGY

In this section, the PHM framework is presented. The fundamentals of the methods used in the methodology are also discussed. The workflow of the PHM methodology is described in Figure 5.1.

One of the most important aspects of PHM is sensor data selection, as it has to be sensitive to the damage of interest. A piezoresistive silicon-based stress sensor was employed in this study due to its direct connection to any physical changes in the package [16]. The stresses are calculated based on the two measured quantities: (1) the stresses determined from pMOS and nMOS current values and (2) the temperature determined from the voltages. Both pMOS and nMOS (p and n channel MOSFETs) transistors are used for the stress difference $D(\sigma) = \sigma_{XX} - \sigma_{YY}$ calculation and shear stress σ_{XY}, respectively. These values are calculated from the following relationship:

$$D(\sigma) = \sigma_{xx} - \sigma_{yy} = \frac{1}{\pi_{44}^{p}} \frac{I_{OUT} - I_{IN}}{I_{OUT} + I_{IN}} \tag{5.1}$$

$$\sigma_{xy} = \frac{1}{\pi_{11}^{n} - \pi_{12}^{n}} \frac{I_{OUT} - I_{IN}}{I_{OUT} + I_{IN}} \tag{5.2}$$

where π_{11}, π_{12},π_{44} are the piezoresistive coefficients of silicon; and I_{IN}, I_{OUT} are the currents measured at the input and output of the sensor, respectively. This data is then passed through a preprocessing step that removes outliers, smoothens the data, and extracts the relative stresses caused by the temperature change. More details about the

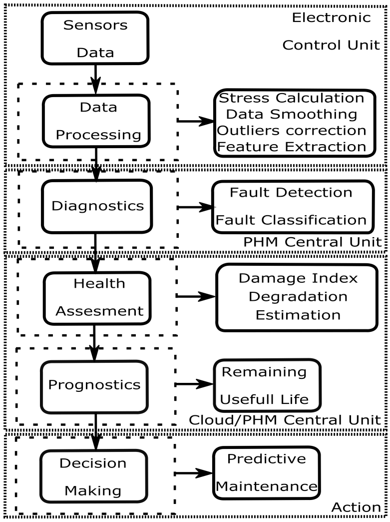

Figure 5.1: Algorithm flowchart that depicts the workflow of the PHM methodology and the corresponding hardware.

theoretical background of the stress sensor can be found in [17] and the fundamentals of how to use such sensor in reliability are described in detail in [16].

An acquisition unit (AU) is utilized to acquire the sensor signals, and the second unit is to process and transmit the data (PHM Central Unit). Through this platform, the data from the sensors are collected, processed, and transmitted to a cloud/database server.

A visualization metric is used to observe any change in the sensor data that might indicate a shift from the normal operation. A failure detection algorithm is used in parallel to check if the stress data is within the threshold to automate this process. Most of the failure detection algorithms can be easily biased by some unknown operating conditions or other unexpected events. Therefore, a visualization metric is necessary as a robust measure. After the failure is recognized, a diagnostic tool is used to classify the data in groups, which are subsequently assigned to a specific physical quantity. An algorithm for degradation estimation and prediction is then applied to assess the failure quantitatively.

Simple, fast, and accurate models are chosen in this methodology. The process of selecting the algorithms is made based on the performance evaluation compared to the failure analysis. Scanning Acoustic Microscope (SAM) and cross-sectioning are used collectively for the required detailed failure analysis.

5.2.1. ACQUISITION UNIT AND CENTRAL PHM UNIT

As mentioned earlier, the piezoresistive silicon-based stress sensor was developed originally for measuring stresses during the manufacturing processes [18]. A dedicated AU is required to steer the sensor and record the data successfully. The first AU was developed together with the sensor [19], but its large size and the small number of sensors for simultaneous measurements made it impractical for in-situ applications. The second

AU developed by Palczynska [20] made the in-situ measurements possible by scaling down the unit with a 12V power source. In addition, a multiplexer was added to increase the maximum number of sensors. More advancements are required to cope with other challenging issues encountered in actual applications: a large amount of data, further miniaturization, data remote access, computing power, and long-running experiments. Such a system is depicted in Figure 5.2.

The newly developed AU consists of an Arduino Yun Mini board as well as a custom-designed board. The former is used to control and readout the sensor and the latter to power and steer the sensor. The Arduino board is equipped with a μcontroller and a μprocessor that sustains the Wi-Fi shield.

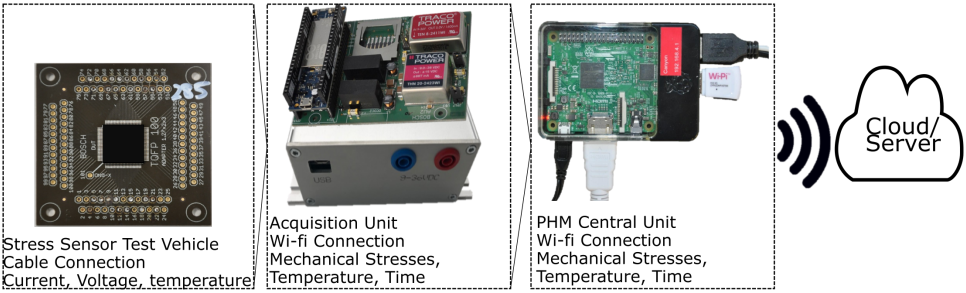

Figure 5.2: Data Flow representation. On each chart is described the electronic unit, the connection, and the data output. Each Test Vehicle is connected to an AU by wires that are able to read out the data from all eight sensors. Up to 5-6 AUs are connected through Wi-Fi to the Raspberry Pi. The cloud or the server collects the data from the Raspberry Pi through a data pipeline.

The advancements are summarized below:

- Centralized local data: A Raspberry Pi is added in the construction as a centralized data server to collect the data from multiple Arduinos through a safe Wi-Fi connection.
- Stability and reliability: The stability of the whole network connection is crucial to maintaining a continuous stream of data.
- Connectivity: The Arduino Yun Mini Wi-Fi shield is connected to the Raspberry Pi access point.
- Automation: The stress calculation, data processing, and transmission are done automatically.
- Safety of the data: The data is to be secured from online hacking and the loss of data due to bugs and networking errors.
- Usability: The control logic should be readily programmable whenever needed.

5

5.3. EXPERIMENTAL SETUP AND TEST VEHICLE

One critical failure mechanism of semiconductor packages is the loss of adhesion at interfaces, causing delamination. Failure modes caused by delamination are passivation damage, wire-bond degradation, intermittent electrical failure, and popcorn cracking.

5.3.1. TEST VEHICLE

The test vehicle (TV) used in this study is a Thin-Quad Flat Package (TQFP) mounted on a Printed Circuit Board (PCB). A TQFP encapsulates eight sensors on a single die, as depicted in Figure 5.3. Each sensor consists of 60 measurement cells in a 6x10 matrix, and every each cell contains the pMOS and nMOS transistor, as shown in Figure 5.3. Seven TVs fabricated from 2 different molding compounds are used in the experiment. The TVs are numbered as:

MCi_j, where i is the molding compound, and j is the sample number.

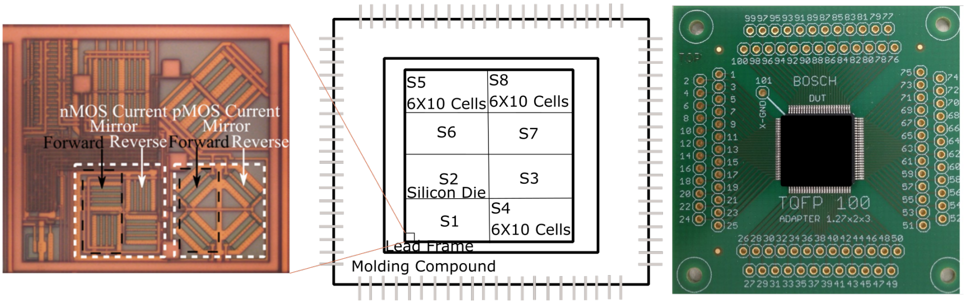

Figure 5.3: Test Vehicle. 8 stress sensors encapsulated in a TQFP package mounted on a PCB. It indicates the sensor location, definition and the number of measuring cells.

The TVs use a pre-oxidized leadframe, which significantly reduces the interface strength between the molding compound and the copper pad. It is expected that the delamination process starts at different times for $MC1$ and $MC2$.

Temperature shock (TS) testing is used for damage acceleration in the study. The TS equipment used in the experiment contains two separate chambers, which are preset at different temperatures. The temperatures profile consists of $-40°C$ and $150°C$, as shown in Figure 5.4. Considering the amount of time needed for the AU to acquire one measurement point (MP), every cycle produces two or three measurement points. Several samples are placed on the basket, and the signal wires are taken out through the middle hollow cylinder, which is used for basket movement. The transition between temperatures is short due to the mobility of the basket (according to Figure 5.4). The stresses inflicted on the samples in this chamber are larger than in a regular thermal chamber due to the fast transition. The temperature difference between the test vehicle and the chamber is initially high, imposing extra stresses.

5.4. EXPERIMENTAL RESULTS

Repeated loading causes accumulated fatigue damage, leading to cracks and rupture. It is generally understood that exposing surface-mount plastic parts to high-temperature

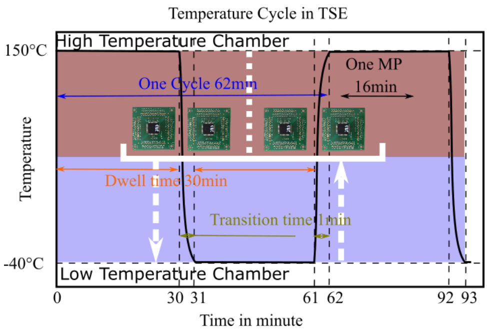

Figure 5.4: Temperature cycle duration. Transition time and the dwell time is briefly specified. The high temperature chamber is shown in red and the low temperature chamber is shown in blue. The transition basket is described in white arrows.

reflow profiles can generate package failures if delamination is present. Figure 5.5 depicts where the delamination occurs and where the stresses are measured in a typical package.

5

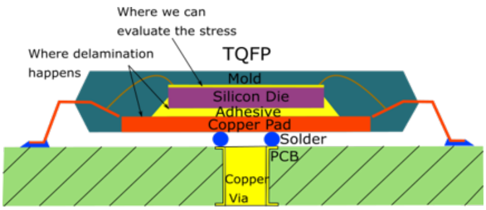

Figure 5.5: Package on PCB cross-section. It shows the main elements of the package and illustrates where the stresses are measured. At the same time, where the delamination usually occurs.

Two experiments were performed in two separate TS chambers. The temperature profile used in the experiment is described in Figure 5.4. In the first experiment, the test vehicles were cycled for 750 TS cycles with 30 minutes dwell time, and in the second experiment, for 1600 TS cycles with 40 minutes dwell time. The stress data were continuously recorded during TS cycling. The data from the TV stress sensor was captured with the AU by a cable connection, which was placed outside the chamber. The AU sent the data to the Wi-Fi Console, followed by the Raspberry Pi to collect this data from the Console and save it. A simple graphical interface was used in Raspberry Pi to check the status of the experiments and the stresses in real-time. At every 50 MPs, the data was sent to the cloud server. The possibility of accessing the Raspberry Pi with a monitor, remote access, or a smartphone, provides flexibility and better control over the experiments.

The raw data gathered from the experiment was composed of the high-precision physical measures of voltages and currents from each cell of the TV and the times when the measurements were performed. By themselves, these measures do not provide any valuable insight into the matter of this study. All this data is contained in a single data set.

5.4.1. Data Preprocessing.

The stress difference is computed using equations 5.1 and 5.2, with the corresponding currents values from the raw data set. The temperatures are calculated from the measured voltages, and the time for measurements is extracted from raw data. All calculation steps are described in Table 5.1.

In the current data-rich environment, vast amounts of data are often automatically collected in a short time period. Data preprocessing and feature extraction procedures become standard in many complex systems to improve data quality, reduce data redundancy, and boost analysis efficiency.

Data Preprocessing is defined as all the actions taken before the actual data analysis process starts. It is essentially a transformation T that transforms raw real-world data set X to a set of new data set Y such that:

(i) Y preserves the valuable information contained in X

(ii) Y eliminates at least one of the problems in X

(iii) Y is more useful than X

In general, preprocessing will reduce the number of features. What is called valuable information includes components of knowledge that exist in the data (e.g., meaningful patterns). It is essential to emphasize the importance of preprocessing. ML and data analysis is not an exception to the principle of Computer Science: *Garbage in garbage out(GIGO)*. This means that, without regard to the algorithm's performance at hand, if the input is of low quality, it is to expect that the output will be of low quality. Consequently, the preprocessing stage must be performed with high attention to detail, as the success of the whole process depends on it. Real-world data tends to be noisy, inaccurate, inconsistent, and often incomplete, mainly due to its vast size, multiple resources, and gathering methods. Therefore, applying preprocessing techniques such as data filtering, filling missing attributes, and feature extraction becomes mandatory.

Each step is summarized below:

Step 1. DIF stores the stress difference values of each cell per MP, TEM stores the temperature values of each cell per MP, and $TIME$ stores the time at the beginning of the recording of each MP. Step 2.Data cleaning techniques usually include detecting N/A values, outliers, and gaps in the data. It is always the first step in data preprocessing [21],[22]. These values are shown in Figure 5.6. Step 3. Handling of outliers on the temperature feature is straightforward as the final distribution along the NAT-axis is known. All values of NAT must fall around +1 and -1 after normalization. Values exceeding these thresholds are data transmission errors and are taken out. Step 4. DIF must pass now through a filtering process to reduce sources of noise [22]. Not all data will be relevant later, so only data points classified as 'high' and 'low' will be filtered for speeding up the process. A window filter of three data points. The average of its sides replaces the value of the data point at the center of the window if the standard deviation surpasses a fixed threshold of 1.1. Step 5. After the filtering process, 2 or 3 measures on each peak or dwell time of the temperature cycle are kept. A transformation is performed, reducing every sequence of MPs to just one point whose value is the average of the original points.

The sensor data set has finally been reduced to an understandable form. The dimensions have been reduced to include one unique signal per cell on the sensor that shows the stress difference variation between the low peak temperature and the high peak tem-

Table 5.1: Data Processing

Input: Sensors Data $I_{OUT}, I_{IN}, V, Time$
Output: Relative stress difference, Temp, Time per Cycle:
$D(\sigma)_{ij} = (\sigma_{xx} - \sigma_{yy})^{ij}_{T=-40°C} - (\sigma_{xx} - \sigma_{yy})^{ij}_{T=150°C}$

1. Stress Difference, temperature and time calculation: DIF_{ik}, TEM_{ik} and TIME_k
2. Data cleaning: Calibration of temperatures and outliers correction: $NAT \in [-1, 1]$, $N/A = 0$
3. Labeling: Temperature classification.
$TemCat_k = "high(150°)"\ \forall NAT_k \in [1.00, 0.98]$
$TempCat_k = "low(-40°)"\ \forall NAT_k \in [-0.98, 1.00]$
$TempCat_k = "undefined"\ \forall NAT_k \in [0.98, -0.98]$
4. Smoothing: Sliding Window
$DIF_{ik} = \sqrt{\frac{1}{w} \sum_{k=1}^{k=w} (DIF_k - \overline{DIF})^2}$
5. Space Transformation: Cycle space; One value per cycle
$(\sigma_{xx} - \sigma_{yy})^{ij} = T_j[(DIF_{ik})]$

*$i = 1, 2, ..., n$ and n = total number of cells
*$j = 1, 2, ..., m$ and m = number of cycles
*$k = 1, 2, ..., p$ and p = total number of measurement points

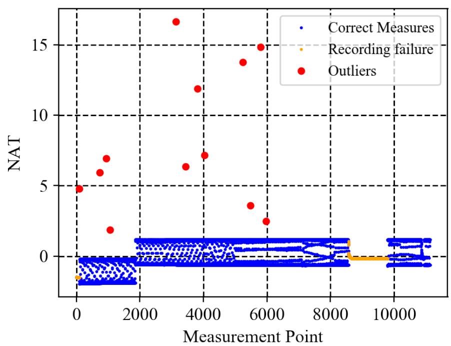

Figure 5.6: Normalized average temperature (NAT) of sensor 3. The temperature is calculated at each cell position and then averaged in one value. The jump in the scaling data is represented by the stop and start of the experiment. A pause explains the orange data in the chamber operation.

perature of each of the temperature shock cycles the TV was exposed to. Figure 5.7 depicts such a unique signal per cell of all 480 measuring locations. After applying the data processing to the datasets obtained from the experiment, the visualization of one single signal per cell is possible, representing the relative values of stresses by subtracting the residual stresses. These new values are representing the stress given by the temperature change $\Delta T = 190°C$.

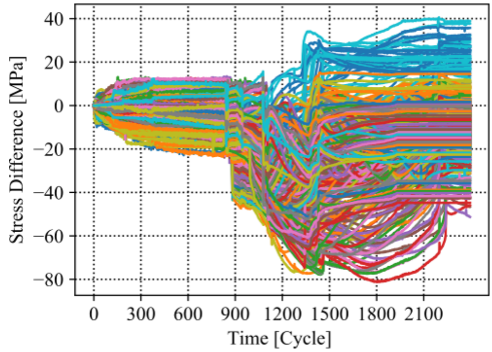

Figure 5.7: $MC1\_1$ TV 480 stress difference sensing cells representation during the experiment. This graph shows the complexity of the stress change during the temperature cycling.

5.4.2. VISUALIZATION METRIC

5

It is reasonable to assume that the delamination processes at both the molding compound and copper pad interface and silicon die and die attach interface can alter the stress distribution over the surface of the silicon die. Even after the stress transformation into one single value per cell and cycle, it is still challenging to analyze the data in the form of 480 cells, see Figure 5.7. A specific load metric, which well represents the effect of CTE mismatch and integrates data from the 480 cells, is required to represent the applied loading [23].

A load metric can be defined using the stress signals from all 480 cells as:

$$\sigma^* = \frac{\sum_{i=1}^{480} |D(\sigma)_i|}{480} \tag{5.3}$$

In this manner, the data from 480 parameters was reduced to a single value, which makes analyzing the stress feasible. Using this procedure, the stress response for the whole die can be visualized, as depicted in Figure 5.8. Sudden increases or sudden drops in stress indicate delamination initiation and propagation in the package. It is important to recall that the crack propagation rate is inversely proportional to the rate of the interface stiffness change, i.e., the stress rate changes with the crack propagation rate.

Visualizing the data from the TV $MC1\_1$ on Figure 5.8, the following observations are made:

- Between 0 and 750 TS cycles, the stresses have a relatively constant value. Small changes are observed due to the moisture release and relaxation effects. This can also be attributed to the effect of aging-induced oxidization on the package stress that has been reported recently [24].
- Around a TS cycle of 850, a small drop is followed by a sudden large increase of the stress, indicating a significant change in the package structure.
- Afterwards, the stresses change at a slow rate but still follow the same trend of increasing for approximately additional 500 cycles until reaching the maximum value. This indicates further changes in the structure.

- From the 1350 TS cycle onwards, the stresses increase initially at a fast rate, but the rate becomes slow. This is an indication that the changes inside the package reach the ending phase.

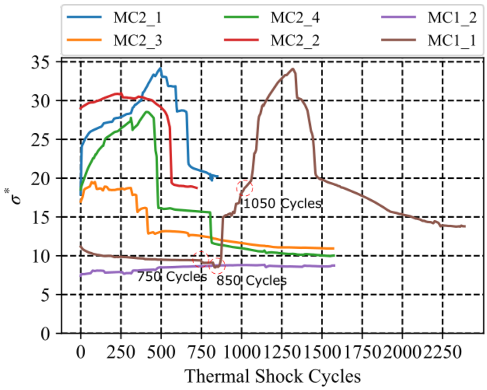

Figure 5.8: Visualization Metric. The sum of absolute stress value change divided by the number of cells in cycle time for $MC1$ and $MC2$. In all samples a stress increase is observed followed by a decrease. Only one sample $MC1_2$ showed constant sum of absolute stress.

The overall behavior of the stresses in $MC1\_2$ TV is constant during the TS, indicating no changes in the package structure. Compared with the $MC1\_1$ stress, behavior does not show any initial changes linked to the moisture and no sudden drops. There are only a few small changes caused by the interruption of the experiment. The visualization metric of all samples is depicted in Figure 5.8. Based on these initial plots, it is observed that all other samples $MC2\_1$, $MC2\_2$, $MC2\_3$ and $MC2\_4$ have some initial delamination. It is speculated that the interface toughness between the molding compound and the copper pad in the case of $MC2$ is smaller than that in the case of $MC1$. The next subchapter explains how the changes shown by the visualization metric are connected to the delamination.

5.4.3. FAILURE ANALYSIS

Using the visualization metric, a change in the sensor data was observed, indicating a shift from the normal conditions. These observations are confirmed by the physical failure and the location documented by scanning acoustic microscope images and cross-section images.

The relative stress difference was correlated with delamination using Scanning Acoustic Microscope (SAM) images. The SAM images taken at various stages are shown in Figure 5.9. The samples were taken out from the TS chamber for taking SAM images. The cables were removed for SAM imaging, and they were re-soldered to the samples before placing them back in the TS chambers. The state of the package $MC1\_1$ before and after 750 TS does not show any delamination (Figure 5.9). A significant change in the stress is observed around 850 Cycles. A SAM analysis was performed again at 850 cycles, and the image is shown in Figure 5.9. The image clearly shows that delamination started at the

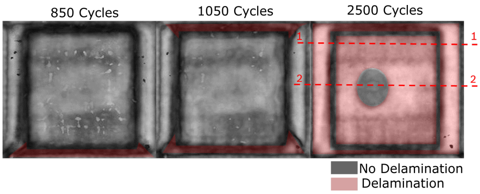

Figure 5.9: SAM of $MC1\_1$ during and after the experiment. Delamination is detected and is depicted in red areas. Two cross-section are performed at the end of the experiment, after 2500 Cycles.

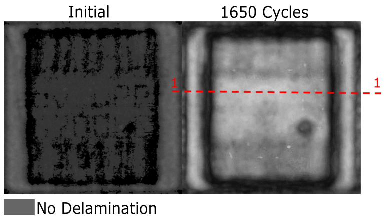

Figure 5.10: SAM of $MC1\_2$ in discrete time. No delamination is present and one cross-section is performed at the end of the experiment, after 1650 Cycles.

bottom of the package, which correlates well with the sudden increase in stress shown in Figure 5.8 for $MC1\_1$.

The same sample was tested again by SAM after additional 200 TS cycles. The image shows that new delamination started on the other side while the first delamination propagated. The SAM image confirmed the crack growth. The stress history in Figure 5.8 (the maximum stress levels at that specific point in time) also corroborates this.

At the end of the experiment, at around 2500 TS cycles, another SAM analysis was performed. The image clearly shows that delamination occurred everywhere except for a small area at the center (Figure 5.9). To further validate the correlation, a destructive failure analysis was performed after the TS cycling. The cross-section images along Line 1-1 of $MC1\_1$ are shown in Figure 5.11. The images clearly show cracks at all three interfaces (molding compound/copper pad, silicon die/die attach, and die attach/copper pad), which validates the SAM investigation. The cross-section images along Line 2-2 of

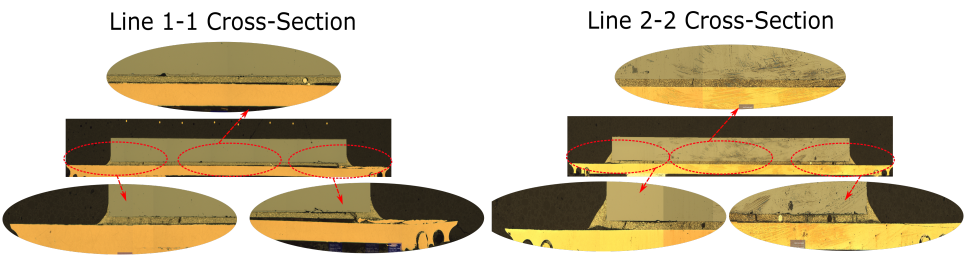

Figure 5.11: Cross-section Failure Analysis of $MC1\_1$ along Line 1-1 and Line 2-2. Crack is present at the interface between molding compound/copperpad and die attach/copper pad along the entire cross-section for Line 1-1, except the middle part in Line 2-2.

$MC1\_1$ are shown in Figure 5.11. The images indicate the presence of cracks at all three interfaces. The images also confirm the interface with no delamination that the SAM images were able to identify.

In TV $MC1\_2$, there was no significant change in stresses during the experiment, indicating that no delamination occurred. This is confirmed by the SAM images obtained after the experiment (Figure 5.10). The cross-section images further corroborated it.

5.5. DIAGNOSTICS

Diagnostics consists of two steps: fault detection by Mahalanobis Distance (MD) and fault clarification by a clustering technique.

5.5.1. FAULT DETECTION

Fault detection by MD was described in details for fault classification in [9] and for fault detection in [11] [25]. Mahalonobis distance is the distance between a point and a distribution. And not between two distinct points, like Euclidean distance. It is effectively a multivariate equivalent of the Euclidean distance. Is the normalized distance between the test point from the sample mean over the standard deviation. A healthy baseline and a threshold are needed to classify the product states (healthy or unhealthy). They are determined by the well-known Mahalanobis Distance (MD). The methodology begins with gathering the sensor data, i.e., the values of stress difference at the 480 sensor cells. These values are referred to as performance parameters. They are stored in a matrix X_{ij} with elements denoted as xij, where $i = 1, 2, ..., p$ and p is the total number of performance parameters (here $p = 480$) and $j = 1, 2, ..., m$ where m is the total number of measurement points. A representative MD applied to the stress sensor cells is shown in Figure 5.12. The healthy baseline is created on the first 800 measurement points of no delamination. The data points exceeding the failure limit are seen in the MD results after 850 Cycles, where delamination occurred. The failure detection point is defined. The threshold was computed from the healthy data (i.e., no initial delamination). The result is also plotted in Figure 5.12.

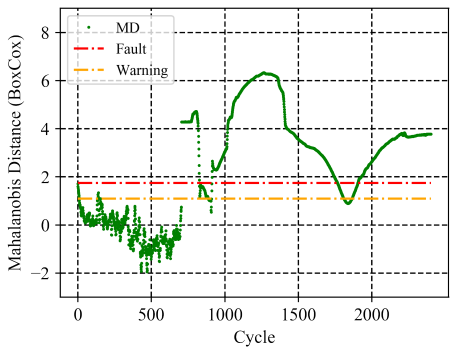

Figure 5.12: Classic threshold MD applied to TQFP stress sensor data. The fault is detected around 850 Cycles.

Since the MD are not normally distributed, a Box-Cox transformation [26] is used to convert the data into a normal distribution. A warning limit threshold is defined as $(\mu + 2\sigma)$ and a fault alarm threshold as $(\mu + 3\sigma)$, based on the normal distribution parameters. A limitation of the Mahalanobis distance is found that the healthy baseline cannot be updated.

5.5.2. Fault Classification

One way of classifying the data is *clustering*, which is a common unsupervised ML technique. It aims to divide objects into groups according to distance-based similarity measure [27]. This method is chosen because of its computational effectiveness amongst other unsupervised ML methods. A clustering technique is used to classify the data. To reveal hidden information such as the necessary number of clusters, the Elbow method, described in [27] is used. All the 480 stress sensing cells are used in the algorithm. Based on the elbow method, only three clusters are needed to split the data correctly. Three subgroups are identified based on the number of prediction class output and the previous knowledge from failure analysis. This can be visualized in Figure 5.13, as follows: the first subgroup is the healthy class 2 until 880 TS cycle; the second subgroup is the data associated with the delaminated copper pad/molding compound interface; the third subgroup contains the data obtained after 1450 cycles onwards attributed to the delamination at the adhesive/silicon die interface.

5

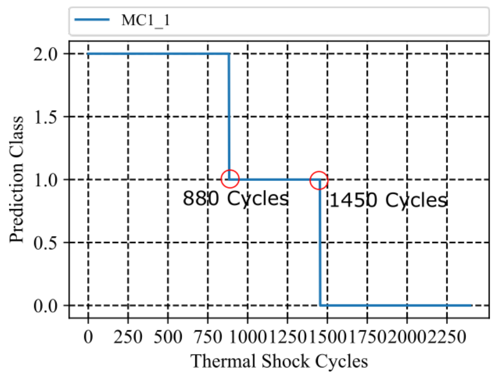

Figure 5.13: Prediction Class with K-Means Clustering method. 2 - represents the health state; 1 - the delamination between molding compound and copper pad; 0 - delamination between the adhesive and silicon die.

The results from the clustering are an indirect validation of the assumption in section 5.4 that delamination starts at the outer areas of the silicon die, increasing the stress difference.

5.5.3. Fault Location

As depicted in Figure 5.3 the silicon die consists of 20 sensing cells on x direction and 24 cells on y, respectively. The high value of the Standard Deviation (SD) per each r number of interval cycles corresponds to the crack tip location in the adhesive layer. The steps followed in the calculation of the *SD* are described in Table 5.2.

Table 5.2: Contour plot standard deviation.

Input: Stress Difference $D(\sigma)_{ijk}$, Cycle Interval
Output: Standard Deviation SD_{ijl} per Interval

Step 1. Calculate the average of each column:
$\bar{x_{ij}} = \frac{1}{r}\sum_{l=1}^{r} D(\sigma)_{ij}$
Step 2. Calculate the standard deviation:
$SD_{ij} = \sqrt{\frac{\sum_{l=1}^{r}(D(\sigma)_{ij} - \bar{x_{ij}})^2}{r-1}}$
Step 3. Plot the contour matrix SD_{20x24}.
Step 4. Evaluate the crack tip on the contour plot.

$*i = 1,2,...,n$ and $n = 20$ number of cells in x direction
$*j = 1,2,...,m$ and $m = 24$ number of cells in y direction
$*k = 1,2,...,p$ and $p =$ number of cycles
$*l = 2,...,r$ and $r =$ Cycle Interval where standard deviation is calculated

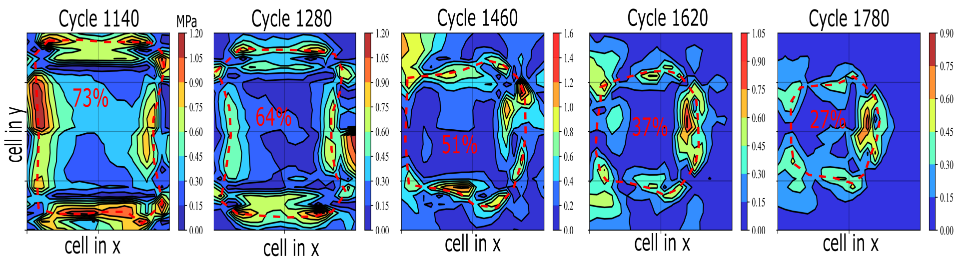

Figure 5.14: Stress Difference SD every 20 Cycles plotted on a contour image for $MC1\_1$. The crack tip is given by the high SD.

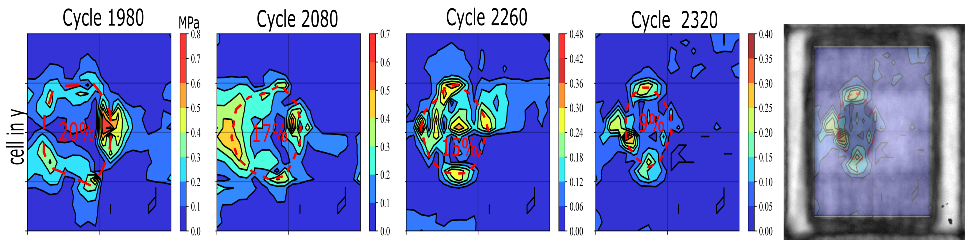

Figure 5.15: Stress Difference SD every 20 Cycles plotted on a contour image for $MC1\_1$. The crack tip is given by the high standard deviation. This is validated over the SAM images on this TV, but also on the other TVs.

For this case, an interval of 20 cycles is chosen to evaluate the standard deviation. This value is chosen to have an effective number of pictures that need to be manually evaluated. Some of them are depicted in Figure 5.14 and 5.15. The high values of standard deviation in the contour plot are clearly shown to correspond to the crack tip in the adhesive layer. This way, it is possible to follow the crack tip delamination area at least every 2 cycle.

In Figure 5.15 an *SD* contour plot image is overlaid over the SAM image. This corroborates our observation that the high values of *SD* indicate the location of the crack tip. This validation is performed on all the other SAM images available and validates our observations.

Every image is then manually evaluated, and a red dotted path is drawn over the high values of the *SD*. The area formed inside the path is then divided by the total area of the sensor area and transformed into a percentage. Therefore, at least every 2 cycles, an estimated remaining not delaminated area can be manually evaluated.

5.6. Health Assessment and Prognostics

5.6.1. Degradation estimation

ESN is a new type of Recurrent Neural Network (RNN) proposed in recent years and was developed by Jaeger [28]. The training process of ESN is more accessible and less computationally intensive than regular RNN, which has the same size [29].

The remaining useful life (RUL) is the amount of time left before a system fails to operate within acceptable limits. RUL calculation is similar to Time-to-Failure (TTF) calculation, except that an upper operating limit threshold is used instead of a failure threshold [30]. Defining a degradation threshold for RUL is a challenging task as it strictly depends on applications. Various application-specific integrated circuits (ASICs) can be packaged in the same type of housing, such as TQFP. For an application with relatively small power dissipation (below 1 W), only 10% of the die attach contact area can still provide good functionality of the ASIC. In contrast, for other applications with larger power dissipation, even 20% of the contact area can bring the device to an end of life. Our study assumed that 10% of the contact area as a threshold for an end of life, i.e., a good connection between the silicon die and die paddle, is assumed to be provided even after 90% of the die attach is delaminated. It is to be noted that the threshold value should be adjusted for different applications.

In this chapter, the ESN method is used to estimate and predict degradation based on incremental stress values. The RUL is predicted by extrapolation from the degradation estimation. For the purpose RUL calculation, the degradation grades of "complete delamination" and "no delamination" are set to be 0% and 100%, respectively. Half of the TVs data $MC1\_1$, $M2\_1$ and $M2\_4$ is used for both training set and testing set. The data from $M1\_2$, ,$M2\_2$ and $M2\_3$ are used for the analysis. In a real time prognosis, the inputs are the stress difference of that specific point in time, and the output will be the degradation estimation percentage. The input of ESN is defined as all relative stresses $D(\sigma)$ of all valid measurement points in all sensors as:

$$u = D(\sigma)_{ij} \tag{5.4}$$

,where $i = 1,2,...,n$ and n = total number of cells (480 in this case) and $j = 1,2,...,m$ and m = number of cycles.

The output of ESN defined as the degradation grade, is a function, from 100% to 0% created based on the *SD* values. This evaluation is performed manually on the contour

Parameter	Commonly used range
Reservoir size	[50,800]
Spectral radius	[0.1,1)
Input scaling	[0,1]
Input shift	[0,max$_{input}$]
Output scaling	[0,1]
Output shift	[0,max$_{output}$]

Table 5.3: Range of parameters of RNN [31].

plot image every 20 cycle. This is a time-consuming task and therefore needs to be automated. Traning half of the TVs data is an attempt to generalize the model. The rest of TVs data is evaluated by the model without manually evaluating the delamination area based on the fault location.

$$y = \begin{pmatrix} 100\% \\ \frac{R_1}{N} \times 100\% \\ \frac{R_2}{N} \times 100\% \\ \vdots \\ \frac{R_n}{N} \times 100\% \\ 0\% \end{pmatrix} \tag{5.5}$$

,where R is the area evaluated by manually drawing a red dotted path and N is the total area of the physical sensor.

Data from three TVs $MC1\_1$, $M2\_1$ and $M2\_4$ were used to train the network. Cross-validation was used in the training process that involved the separation of data into k folds. In this study $k = 10$ was used. After the division, the model was trained on 9 of these folds and then validated using the remaining fold. The average of the ten measures mean square error (MSE) was the metric used to improve the model.

Up to the point where there is a failure detected, the output is considered 100% as no delamination is present. Afterwards, a manually created function is used to describe the degradation (equation 5.5).

The parameter size of dynamic reservoir n, the desired spectral radius of dynamic reservoir r, the input shift, and scaling, and the output shift and scaling have to be optimized. The commonly used range of parameters is shown in Table 5.3.

The optimization strategy used in this case is a conservative one. Changing one parameter with a certain step, keep others unchanged, train the ESN using the cross-validation to get the lowest MSE.

During optimization, the ESN was trained and tested for 10^6 times. The minimum MSE was then found, and its combination of the parameter was recorded. The optimization process took about 5 hours. This optimization shows that the reservoir size and the spectral radius are two main factors influencing MSE. A very good practical guideline can be found in [32]. The execution time of the model is 659ms for fitting and 745ms for prediction on a regular office laptop. Degradation prediction in percentage for all the testing modules are shown in Figure 5.16. Degradation percentages here refer to the

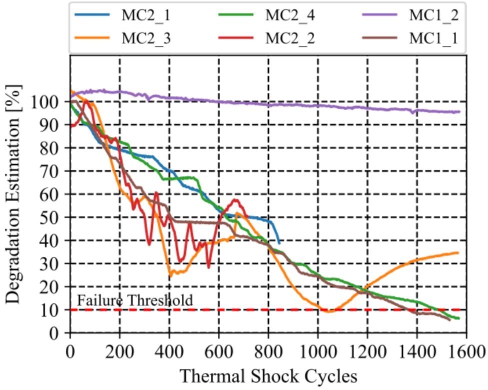

Figure 5.16: Degradation estimation ESN Output for $MC1$ and $MC2$.

delamination area. Comparing the results from the ESN prediction and the SAM images from Figure 5.17 the following can be stated:

- For TV $MC2\_1$ and $MC2\_2$ a 30% delamination area remaining is predicted by the ESN. The SAM images validate this.
- For TV $MC2\_3$ and $MC2\_4$, the model predicts an almost full delamination percentage close to few percentages. The SAM images also confirm this.
- As expected for TV $MC1\_2$ no degradation is predicted.

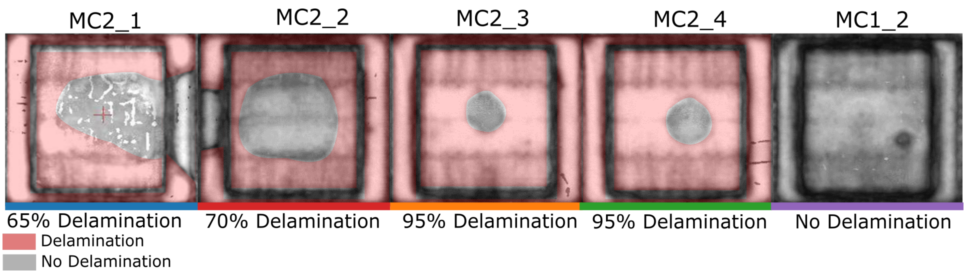

Figure 5.17: SAM Images at the end of the experiments for $MC1$ and $MC2$.

Following the same methodology from the fault location section, the degradation estimation for the other TVs was also evaluated and is depicted in Figure 5.18. A comparison between the ESN model and SD methodology is shown. The results show good accuracy in the generalization of the ESN model. The model can be, of course, improved by including more sample data into the training data.

Based on the neural network model, RUL estimation can be extrapolated. However, extrapolating RUL from this model under real operating conditions remains a challenge that must be addressed in future studies. It is observed that the RUL for all the modules strongly depends on the failure detection point, the loading conditions, and material properties.

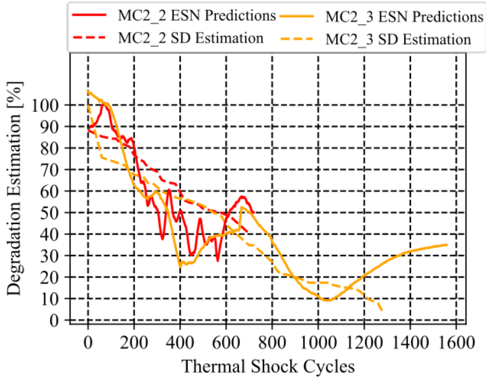

Figure 5.18: Degradation estimation ESN Output vs SD Estimation.

5.7. CONCLUSION

The thermo-mechanical stress-based prognostics approach was developed to extend the stress-based PHM capability into a quantitative domain where accurate prediction of remaining useful life (RUL) became possible. The approach was implemented with actual microelectronics packages subjected to harsh accelerated testing conditions. Piezoresistive stress sensors were employed to measure the internal stresses of microelectronic packages. An Acquisition Unit (AU) and a Raspberry Pi were used for sensor data readout, collection, and evaluation. Accelerated tests in a thermal convection chamber were performed, and the resultant failure data were utilized to conduct data processing. The statistical techniques for diagnostics and the machine learning (ML) algorithms for health assessment and prognostics were then implemented to estimate and predict the degradation state.

The neural network model used in the chapter was built and tested by using one-half of TVs as a training set and the other half of TVs as a testing set. The network parameters were optimized only for these datasets. More data sets must be obtained to train and test the network to create a more generalized model. Nevertheless, the results show that the proposed framework and approach outperform the conventional failure analysis approach (e.g., SAM analysis). The results also confirm that data-driven approaches provide the opportunity to monitor the asset during operation and understand the asset behavior based on its current design. This can lead to a better product in the future and further optimize resources and expenditures.

REFERENCES

[1] A. Prisacaru, P. J. Gromala, B. Han, and G. Zhang, *Degradation estimation and prediction of electronic packages using data driven approach,* IEEE Transactions on Industrial Electronics , 1 (2021).

[2] W.-S. Lei and A. Kumar, *Delamination and reliability issues in packaged devices,* in *Adhesion in Microelectronics*, edited by K. Mittal and T. Ahsan (John Wiley & Sons, Inc.) pp. 267–312.

[3] G. Q. Zhang, W. D. v. Driel, and X. J. Fan, *Mechanics of microelectronics*, Solid mechanics and its applications No. v. 141 (Springer) OCLC: ocm70268148.

[4] N. Vichare and M. Pecht, *Prognostics and health management of electronics,* **29**, 222.

[5] Y. Zou, J. C. Suhling, R. W. Johnson, and R. C. Jaeger, *Complete stress state measurements in chip on board packages,* in *Multichip Modules and High Density Packaging, 1998. Proceedings. 1998 International Conference on* (IEEE) pp. 405–415.

[6] A. R. R. Adli, K. M. B. Jansen, F. Schindler-Saefkow, and F. Rost, *Experimental investigation and interpretation of the real time, in situ stress measurement during transfer molding using the piezoresistive stress chips,* in *Thermal, mechanical and multi-physics simulation and experiments in microelectronics and microsystems (eurosime), 2014 15th international conference on* (IEEE) pp. 1–4.

[7] Y. Zou, J. C. Suhling, R. W. Johnson, R. C. Jaeger, and A. K. M. Mian, *In-situ stress state measurements during chip-on-board assembly,* **22**, 38 ().

[8] A. Palczynska, P. J. Gromala, D. Mayer, B. Han, and T. Melz, *In-situ investigation of EMC relaxation behavior using piezoresistive stress sensor,* **62**, 58 ().

[9] A. Prisacaru, A. Palczynska, A. Theissler, P. Gromala, B. Han, and G. Q. Zhang, *$in\ situ$ failure detection of electronic control units using piezoresistive stress sensor,* **8**, 750 ().

[10] B. Wu, D.-S. Kim, B. Han, A. Palczynska, A. Prisacaru, and P. J. Gromala, *Hybrid approach to conduct failure prognostics of automotive electronic control unit using stress sensor as in situ load counter,* , 1.

[11] A. Palczynska, A. Prisacaru, P. J. Gromala, B. Han, D. Mayer, and T. Melz, *Towards prognostics and health monitoring: The potential of fault detection by piezoresistive silicon stress sensor,* in *Thermal, Mechanical and Multi-Physics Simulation and Experiments in Microelectronics and Microsystems (EuroSimE), 2016 17th International Conference on* (IEEE) pp. 1–8.

[12] A. Prisacaru, A. Palczynska, P. J. Gromala, B. Han, and G. Q. Zhang, *Condition monitoring algorithm for piezoresistive silicon-based stress sensor data obtained from electronic control units,* (IEEE) pp. 1119–1127.

[13] F. Schindler-Saefkow, F. Rost, A. Otto, W. Faust, B. Wunderle, B. Michel, and S. Rzepka, *Stress chip measurements of the internal package stress for process characterization and health monitoring,* in *2012 13th International Thermal, Mechanical and Multi-Physics Simulation and Experiments in Microelectronics and Microsystems* (2012) pp. 1/10–10/10.

[14] M. K. Rahim, J. C. Suhling, R. C. Jaeger, and P. Lall, *Fundamentals of delamination initiation and growth in flip chip assemblies,* in *Proceedings Electronic Components and Technology, 2005. ECTC '05.* (2005) pp. 1172–1186 Vol. 2.

[15] A. Prisacaru, E. O. Guerrero, P. J. Gromala, B. Han, and G. Q. Zhang, *Degradation prediction of electronic packages using machine learning,* in *2019 20th International Conference on Thermal, Mechanical and Multi-Physics Simulation and Experiments in Microelectronics and Microsystems (EuroSimE)* (2019) pp. 1–9.

[16] A. Prisacaru, A. Palczynska, P. Gromala, B. Wu, B. Han, and G. Zhang, *Accuracy of cmos-based piezoresistive stress sensor for engineering applications of thermal loading condition: Theoretical review and experimental validation,* IEEE Sensors Journal **19**, 9139 (2019).

[17] R. Jaeger, J. Suhling, R. Ramani, A. Bradley, and Jianping Xu, *CMOS stress sensors on [100] silicon,* **35**, 85.

[18] R. B. GmbH, *Abschlussbericht zum verbundvorhaben iforcesens: Entwicklung eines integrierten stressmesssystems zur quantifizierung der 3 d-v erformung von sensorbauelementen in abhangigkeit des verpackungsprozesses,* https://doi.org/10.2314/GBV:606643435.

[19] H. Kittel, S. Endler, H. Osterwinter, S. Oesterle, and F. Schindler-Saefkow, *Novel stress measurement system for evaluation of package induced stress,* in *Integration Issues of Miniaturized Systems-MOMS, MOEMS, ICS and Electronic Components (SSI), 2008 2nd European Conference & Exhibition on* (VDE) pp. 1–8.

[20] A. Palczynska, F. Pesth, P. J. Gromala, T. Melz, and D. Mayer, *Acquisition unit for in-situ stress measurements in smart electronic systems,* in *Thermal, mechanical and multi-physics simulation and experiments in microelectronics and microsystems (eurosime), 2014 15th international conference on* (IEEE) pp. 1–4.

[21] S. Naduvil-Vadukootu, R. Angryk, and P. Riley, *Evaluating preprocessing strategies for time series prediction using deep learning architectures,* (2017).

[22] S. A. Alasadi and W. S. Bhaya, *Review of data preprocessing techniques in data mining,* Journal of Engineering and Applied Sciences **12**, 4102 (2017).

[23] Y.-H. Yang, B. Han, A. Prisacaru, P. Gromala, S. Jiang, and A. Sarwar, *In-situ service load monitoring of automotive electronic systems using silicon-based piezoresistive stress sensor,* Microelectronics Reliability **110**, 113650 (2020).

[24] A. Inamdar, A. Prisacaru, M. Fleischman, E. Franieck, P. Gromala, A. Veres, C. Nemeth, Y. Yang, and B. Han, *Study of thermal aging behavior of epoxy molding compound for applications in harsh environments,* in *2019 IEEE 69th Electronic Components and Technology Conference (ECTC)* (2019) pp. 811–818.

[25] S. Kumar, V. Sotiris, and M. Pecht, *Health assessment of electronic products using mahalanobis distance and projection pursuit analysis,* **2**, 242.

[26] M. Pecht, *Prognostics and health monitoring of electronics,* in *Electronic Materials and Packaging, 2006. EMAP 2006. International Conference on* (IEEE) pp. 1–10.

[27] F. Pedregosa, G. Varoquaux, A. Gramfort, V. Michel, B. Thirion, O. Grisel, M. Blondel, P. Prettenhofer, R. Weiss, V. Dubourg, J. Vanderplas, A. Passos, D. Cournapeau, M. Brucher, M. Perrot, and E. Duchesnay, *Scikit-learn: Machine learning in Python,* Journal of Machine Learning Research **12**, 2825 (2011).

[28] H. Jaeger, *Harnessing nonlinearity: Predicting chaotic systems and saving energy in wireless communication,* Science **304**, 78 (2004).

[29] J. Dai, G. K. Venayagamoorthy, and R. G. Harley, *An introduction to the echo state network and its applications in power system,* in *2009 15th International Conference on Intelligent System Applications to Power Systems* (2009) pp. 1–7.

[30] D. Galar, U. Kumar, J. Lee, and W. Zhao, *Remaining useful life estimation using time trajectory tracking and support vector machines,* Journal of Physics: Conference Series **364**, 012063 (2012).

[31] E. Z. Marco Rigamonti, Piero Baraldi, *Echo State Network for the Remaining Useful Life Prediction of a Turbofan Engine* (European Conference of the Prognostics and Health Management Society, 2016).

[32] M. Lukosevicius, *A Practical Guide to Applying Echo State Networks* (Springer, 2012).

6

Towards Virtual Twin for Electronic Packages in Automotive Field

The piezoresistive silicon-based stress sensor can be part of the Digital Twin implementation in automotive electronics. One solution to enforce reliability in digital twins is the use of Machine Learning (ML). Physical parameters are being monitored, while other parameters are projected with surrogate models, just like virtual sensors. Piezoresistive stress sensors are employed to measure the internal stresses of electronic packages, an Acquisition Unit (AU) to read out sensor data, and a Raspberry Pi to perform the evaluation. Accelerated tests in the thermal air chamber are performed to get time series data of the stress sensor signals, with which we can know better about how delamination develops inside the package. In this study, stress measurements are performed in several electronic packages during the delamination. The stress sensor detects the delamination due to the continuous change of the stiffness and the local boundary conditions causing the stresses to change. Although the stress change in multiple cells can give enough information if delaminated or not, its delamination area location is unknown. Surrogate models built upon Neural Networks (NN) and Finite Element Method (FEM) are developed to predict the out-of-plane stresses at the delaminated layer. FEM simulation models are calibrated with Moiré measurements and validated at the component and PCB level with stress difference measurements. Simulation delamination areas are constructed based on the Scanning Acoustic Microscope (SAM) images and validated with equivalent stress measurements. In the end, the surrogate model is predicting the out-of-plane stress in the adhesive layer. The results show a good correlation when compared to the SAM images.

Parts of this chapter have been published in Microelectronics Reliability Journal (2021) [1].

6.1. Introduction

There are several definitions of Reliability[2, 3]. In engineering[3], it is set as the "ability of a system or component to perform its required functions under stated conditions for a specified period of time." These conditions refer to conditions like mechanical, thermal, electrical specifications. In this definition, a system[4] is "a combination of interacting elements (components) organized to achieve one or more stated purposes." Several modern products would classify as a component or system as a system of systems (SoS). SoS is defined [4] as: "Systems that are composed of independent constituent systems, which collaborate towards a common goal through the synergism between them." This definition would fit, e.g., a national power grid, a modern fighter aircraft, an oil refinery, etc.

Reliability prediction methods date 70 years into the past[5]. In that time, the concept of reliability has been extensively used on design, operation, and maintenance tasks. On the design stage of a product, the concept of Design for Reliability (DfR)[6] appears, in which a model of the product is developed. The manufacturer uses this model to define the working conditions and lifetime of its guarantee. A more reliable component (or system) works long hours on tougher conditions on the operation stage, saving with this maintenance, repairs, and replacement costs.

There are two main approaches in reliability: A statistic-based approach (like the Weibull model[7] or the fault tree analysis[8] that considers the reliability of each component to estimate the reliability of a system) or a physics-of-failure-based approach[6] (like the use of Finite Element Method (FEM) software to simulate loading conditions and ensure that the component will perform at its design capacity).

6

The problem with the statistical-based models is that they are created with failure data that is population-relevant. This is indeed a good approximation for simple non-critical cases in which the failure of an outlier component that doesn't stick to the expected probability distribution is not relevant. On the other hand, the physics-of-failure-based models rely on the computational modeling of the failure mechanisms working on the specific component.

Both models do not predict the *real* status of a singular component as neither monitors the real-time state of the component. Their assessments are of statistical relevance.

It is because of this that, for example, other techniques as redundancy are usually used to ensure zero Downtime (the period in which a system is unavailable) on relevant components. But this solution requires having another component identical in function as the original as backup, and this solution is not cost-effective.

With this new notion and the foreseeable advent of widespread complex consumer-grade systems as autonomous vehicles, it becomes evident that a new paradigm must be set to overcome the limitations of current reliability models.

This shift, the Digital Twin, integrates ultra-high fidelity simulations [9], historical data, and machine learning models to mirror the physical object. Because the Digital Twin term is developed for a complex system, we propose using the Virtual Twin term to represent the component part in this chapter.

Therefore, this chapter proposes the virtual twin of an electronic package using techniques like geometrical-based simulations, experimental data, and machine learning models.

6.1.1. AUTOMOTIVE ELECTRONICS

A recent report by PwC[10] predicts that by 2020 the % of total car cost used on automotive electronics will be 35%, and it will climb to 50% by 2030. The main reasons for this predicted increase are:

- An increment in electronic systems quantity on the vehicle required to keep and monitor the vehicle's efficiency required by regulation laws in the EU and the US.
- An increase in functionalities added by the manufacturers to improve the user experience. New electronic systems (including new sensors, control units, communication network, and power supply) are added to give the car new functions such as assisted parking, vehicle cruise speed control, infotainment, emergency braking, etc.).
- The push towards automotive driving adds new systems like radar, lidar, GPS location, and steering control that were not required on traditional autos.

The automotive industry is particular as consumer demands on its final product are higher than on other products. Car manufacturers must ensure that their electronic products last longer and ensure their functionality.

It comes to mind the case of Toyota between 2009-2011, in which 5.8 million vehicles were recalled due to an undetected error that would cause the vehicle to accelerate without forewarning.

With the industry moving forward towards offering consumer-grade autonomous driving vehicles, there have never been higher requirements to automotive electronics in terms of power efficiency, size, and weight, especially in reliability.

6.1.2. MACHINE LEARNING

ML should not be confused with Artificial Intelligence (AI). AI is the concept of a machine exhibiting intelligence similar to humans or animals[1] AI is divided into Weak and Strong AI. The former is an AI that can perform a narrowly defined set of tasks or just one task. The latter is an AI that is capable of applying intelligence to a problem and even showing consciousness. This means that the machine exhibiting Strong AI is not constrained to just one set of problems, as its knowledge and intelligence generalize to all sets of tasks.

Strong AIs do not exist up to date. All current AIs are Weak as they specialize in solving a set of constrained tasks and work using curated data sets[2], differing from the human learning experience.

For mentioning a set of examples:

- Google's search algorithm
- Google's image recognition algorithm
- A predictive keyboard algorithm

[1] This is what is called natural intelligence.

[2] is considered best practice to preprocess the data before feeding it to a learning algorithm to expedite the learning process. On occasions, it is mandatory to preprocess the data as learning would be impossible otherwise.

- An email spam filter
- AlphaGo[3][11]

Even though these AIs show a performance exceeding human capabilities in speed, efficiency, and accuracy, it is prudent to remind that they remain tightly constrained to their specified task. Hence, Google's search algorithm will not play Go as AlphaGo, and AlphaGo will never get good search results as Google's search algorithm. This would not be a problem for a Strong AI, as the task change would be seamless. For this AI, it would be an easy task as would be for a human who knows how to play chess to learn to play checkers.

ML is a subset of artificial intelligence (AI) that creates systems to learn and predict outcomes without manually programming a computer and is also known as predictive analytics or statistical learning"[12]. It is a set of algorithms and techniques focused on learning from data. Here, data is an organized collection of measures and/or classes, and learning means the ability to get information from data that would generalize to other data sets. This last is what differences ML techniques from other statistical tools. They focus on the generalization aspect of the data analysis and create a model that works with the data at hand. An ML model is *general*, it is valid for new data points the model has never been exposed to.

ML is not a recent research field. One of the first steps in this direction is considered to be taken by Thomas Bayes[13] with "An Essay towards solving a Problem in the Doctrine of Chances" in 1763, where he stated the bases for Bayesian Statistics, a statistical theory in which the evidence about the real state of the world is expressed in terms of the degree of belief. Scattered advances were performed in the early 18th century as the prolific mathematician Adrien-Marie Legendre published the Least Squares method in 1805. Pierre-Simon Laplace formalizes what is known today, Baye's Theorem, in 1812. No more significant progress would be made until mid 19th century.

The context of the mid-19th century contemplates the beginning of the Digital Revolution[4] that was triggered by the invention of the transistor in 1947 by John Bardeen, Walter Brattain, and William Shockley at AT&T's Bell Labs in the US. This invention will allow the miniaturization of contemporary computers, which are relayed on vacuum tubes, and solve two of its biggest problems: Size and power consumption. In a few years, a computer passed from using a whole room's space to fit in a suitcase, then fit on a desk, be the size of a notebook, and so on. The miniaturization process mostly followed a linear pattern defined in 1965 by Gordon Moore[5] Current computers have transistors in their architecture whose size is 7nm.

The miniaturization of computers carried an exponential growth in computational power that allowed ML models to be applicable. In the later decades, to become mainstream with open source projects as Scikit-learn, TensorFlow, and PyTorch.

The Digital Revolution gave another vital asset required for applying ML algorithms: Data. As DOMO's reports on Data usage, details[14, 15] 2.5 quintillions of bytes were

[3] AlphaGo is an AI developed by Google's DeepMind to play the board game Go. It's the first AI to beat a Go's professional player without the use of handicaps on a 19x19 board.

[4] Also called the Third Industrial Revolution.

[5] Moore proposed in 1965 that the number of transistors in microprocessor doubles each year, he would later correct it to defend that said doubling will happen every two years. For over 50 years, this law has prevailed.

generated every minute of the year 2017. During this same year, 90% of all the Data humankind has ever produced was generated. It is estimated that in the year 2020, a new 1.7MB will be generated every second *per person living*.

This joint context of easily available computational power and colossal quantities of Data drove the Machine Learning explosion at the beginning of the 21st century. Soon, ML models outmatched humans in tasks as song recognition[16], handwriting recognition[6], face recognition[17], etc.

There are three big tasks groups for ML:

- Classification: These tasks consist of the differentiation of two or more distinct, discreet classes. Some methods for the task are Support Vector Classification (SVC), Stochastic Gradient Descent Classifier (SGD Classifier), and KNeighbors Classifier.
- Regression: These tasks consist of the finding of a continuous value. Some methods used for this task are Support Vector Regressor (SVR), Ridge Regression, Artificial Neural Networks (ANN), and Stochastic Gradient Regressor (SGD Regressor).
- Clustering: These tasks consist of grouping data points into a finite number of classes. One of the most used methods for this task is called KMeans.

In this chapter, an AU can record stress measurements during reliability tests capable of sending the data to a centralized data unit through a Wi-Fi connection. Data stored in the Raspberry Pi is then sent to a server where data is processed. The data is transformed by removing the outliers, filtering, labeling, and scaling. An ML regression technique is then applied to create a model to predict the out-of-plane stresses in the adhesive layer by feeding different delamination profiles simulation data. The model is then used to assess the out-of-plane stresses in the adhesive layer from the stress difference measurement data. It is known that out-of-plane stresses are a direct indication of where the delamination area is located. Therefore, this model's goal is to indicate where the delamination in the adhesive is located, not the magnitude of the stress values.

6.2. EXPERIMENT

Accelerated reliability testing is used to stress the Test Vehicles (TV). In this study, an air thermal shock chamber was used, which consists of two separate chambers with constant temperature, one at 150° and the other one at −40° as shown in Figure 6.1. The basket containing the TVs is moving up and down between chambers. The transition time between chambers is relatively short, making the experiment suitable to accelerate the degradation of the electronic packages.

The dwelling time was predetermined to provide a condition where all components reach the uniform distribution at target temperatures.

6.2.1. TEST VEHICLE

Thin Quad Flat Packages (TQFP) 100x100 pins with encapsulated piezoresistive silicon-based stress sensors are mounted on a PCB. TQFP is a standard package for the automotive industry in application-specific integrated circuits (ASICs). They are mostly used

[6]Software that solve this task are called OCR, that stands for Optical Character Recognition.

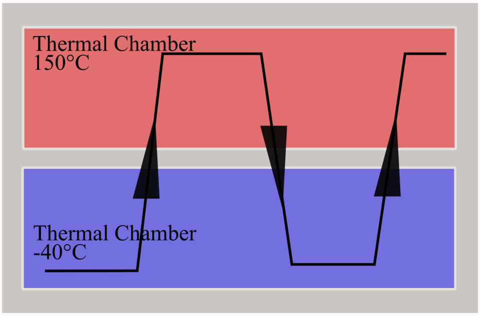

Figure 6.1: Thermal Chamber procedure description.

for vehicle airbags, engine management, transmission control system, advanced driver assistance systems, in-vehicle communication, and alternator electronics. As shown in Figure 6.2 the functional die is replaced by the stress sensor die.

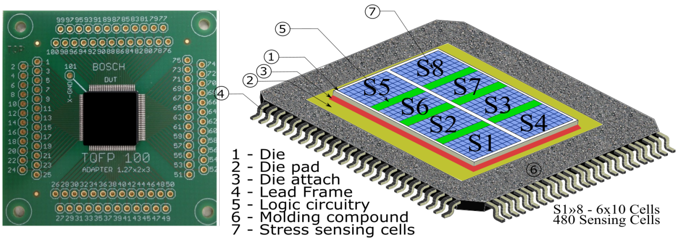

Figure 6.2: TQFP Mounted on a PCB Test Vehicle.

The packaged silicon die consists of 8 sensors, with 60 stress measuring cells each, having 480 stress sensing cells. The packages were specially designed to have low adhesion strength between the leadframe and the molding compound. One of the ways to do this was to use oxidized leadframes in the packaging process. Also, two molding compounds were used for packaging MC1 and MC2. In total, six TVs were tested by performing two separate experiments. Two TV are of type 1 molding compound $MC1\_1$, $MC1\_2$ and another four of type 2 molding compound $MC2\_1 ... MC2\_4$, respectively. In this chapter, the $MC1\_1$ sample shows the stress difference, simulation out of plane stress distribution, and the SAM images in case of delamination.

6.2.2. Stress Evaluation

In TQFP, stress sensors are encapsulated as a regular die to record the mechanical stresses during reliability tests. In this chapter, TQFP contains eight sensors, with each 6 by 10 stress sensing cells. The stresses are calculated with the following formulas.

The relationship between measured currents and stresses are :

$$D(\sigma) = \sigma_{xx} - \sigma_{yy} = \frac{1}{\pi_{44}^{p}} \frac{I_{OUT} - I_{IN}}{I_{OUT} + I_{IN}} \tag{6.1}$$

$$\sigma_{xy} = \frac{1}{\pi_{11}^{n} - \pi_{12}^{n}} \frac{I_{OUT} - I_{IN}}{I_{OUT} + I_{IN}} \tag{6.2}$$

where π_{11},π_{12},π_{44} are the piezoresistive coefficients of silicon; and I_{IN}, I_{OUT} are the currents measured at the input and output of the sensor, respectively. More details can be found in Ref. [18], [19], [20].

After the experiments were performed, data was processed, and only one measurement point per cycle is extracted at the dwell time. Then the stress values at −40° are extracted from the values at 150° as follows:

$$D(\sigma)_{ij}^{rel} = (\sigma_{xx} - \sigma_{yy})^{-40^\circ C} - (\sigma_{xx} - \sigma_{yy})^{150^\circ C} \tag{6.3}$$

,where $i = 1,..,n$ is the number of measurement points, $j = 1,...,480$ is the number of sensing cells and $D(\sigma)_{ij}$ are the relative stress difference.

6.2.3. ACQUISITION UNIT

A dedicated acquisition unit was used to power, steer and acquire data from the stress sensor. Additional improvements have been made to the AU to facilitate efficient experiments. The former AU consists of three boards in terms of dimension and weight, and it is 110 x 66 x 45 mm in size. The new AU has only one board, and its size is 90 x 71 x 20 mm. Shown in Figure 6.3.

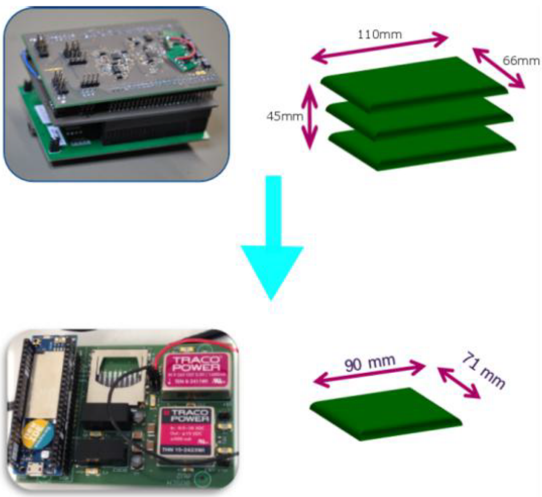

Figure 6.3: Acquisition unit downsize. The three boards from the previous AU are compressed in a single board.

The former acquisition unit consumes several minutes to collect data from 480 cells (8 sensor x 60 cells/sensor) at 12-bit accuracy in terms of speed. The new acquisition unit has two ADCs, ADS1115 and ADS1015; by changing the I2C slave address value in the I2C library, one can choose between two ADC. When ADS1115 is chosen, we can get 16-bit accuracy, but it requires more time to go through all 480 cells; When we choose ADS1015, we still have 12-bit accuracy data but faster measurements. As for other functions, the new one has a built-in WIFI module that facilitates the connection with Raspberry Pi, and the wireless data transmission through WIFI is realized; Pi was also added because stress value calculation method, stress prediction algorithms based on Neural

Network (NN), are all coded in Python and can run on Raspberry Pi. That is to say, Pi is a microcomputer that can afford all the functions in this task, and it is, of course, lighter, cheaper, more convenient, and mobile than a PC. Meanwhile, real-time data processing becomes possible because a Wi-Fi connection can realize real-time data transmission between Pi and Arduino.

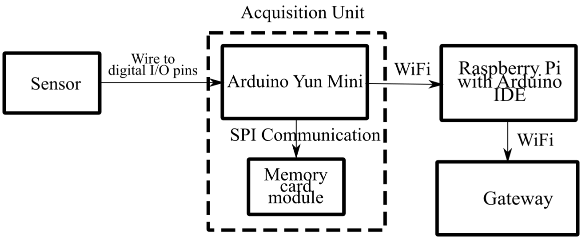

Figure 6.4: Data flow. Arduino Yun Mini collects the data from the sensors, saves the data to a memory card and also sends the data to the Raspberry Pi.

By realizing a wireless Wi-Fi connection between Arduino and Pi (see Figure 6.4), we can imagine that Pi can communicate with multiple Arduinos at the same time. Pi can generate its network as a hot spot, and Arduinos can access the hot spot, thus building the grid that multiple Arduino transmit data to a common central process Pi. So we can realize the in-situ stress monitoring on multiple sensors and AU by one Pi.

6.2.4. Delamination validation through SAM images

SAM image of the sample was recorded at 0 cycles, 1170 Cycles, and at the end. This can help in correlating between the stress difference values and delamination. In Figure 6.5 SAM images of the TQFP package targeting the interface between copper pad/molding compound, die attach/copper pad and die/die attach are shown. One image was performed at the beginning of the test, showing no initial delamination. An intermediate picture at 1170 Cycles, where initial delamination is detected, was performed. The third picture was performed after 2500 temperature cycles, and more than 80% of delamination is found.

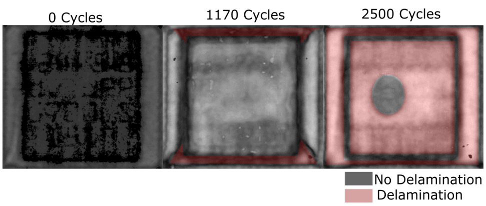

Figure 6.5: MC1_1 TV SAM image before and after the reliability test. The delamination area is shown in red color.

6.2.5. Data from Thermal Cycling Data

The in-plane mechanical stresses were recorded during the entire test for all the 480 measuring cells. The AUs were placed outside the chamber with a wire connection with the samples inside. For visualization purposes average relative stress changes are calculated by averaging over 480 cells as follows:

$$D(\sigma)_j^{average} = \sum_1^{480} D(\sigma)_{ij}^{rel} \tag{6.4}$$

The influence of delamination in the die attach over the stress difference on top of the die is shown in Figure 6.6. An average value of stress per cycle is depicted by using equation 6.4. The first observation is that the stress values completely change after the 900 cycle reaching a maximum change at 1300 cycle. The stress variation corresponds to the local boundary condition changes. The high absolute values of stress are driven by the high stresses in the region close to the crack. The delamination is confirmed by the SAM image taken at the 1170 cycle. For a better understanding of the stress signal given by the delamination, a FEM model is constructed.

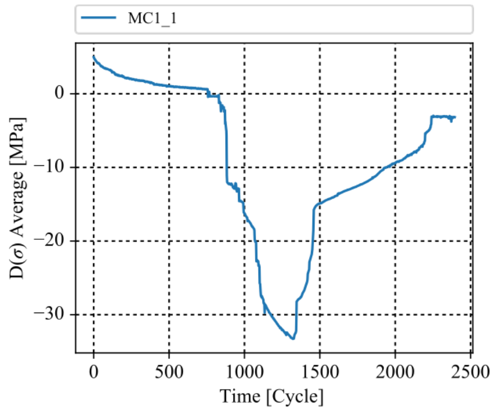

Figure 6.6: Normal in-plane relative stress difference average along all 480 Cells for MC1_1 Sample.

6.2.6. THERMAL DEFORMATION WITH MOIRÉ INTERFEROMETRY

Real-Moiré interferometry was utilized to improve the prediction accuracy of FEM simulation. The method is a full-field optical technique to measure the in-plane deformations with high sensitivity, high signal-to-noise ratio, and excellent clarity [21]. The outputs are the contour maps of in-plane displacements. It has been used widely for electronic packaging design, and reliability assessment [22]. The optical/mechanical configuration used in the study consists of (1) a portable engineering moiré interferometer that provides two sets of virtual reference gratings and (2) a conduction chamber built on a high-performance thermoelectric cooler that provides accurate temperature control. More details about the test setup can be found in [23].

A cross-line diffraction grating with a frequency of 1200 lines/mm was replicated on the specimen surface at room temperature (20°). The specimen was placed inside the thermal chamber and was subjected to a thermal excursion. The specimen grating deformed together with the specimen to produce two orthogonal in-plane displacement fields. The details about the grating and replication procedures can be found in [21] and [24]. The in-plane Ux and Uz displacement fields, obtained at 0° and 150°, are shown in Figure 6.7, where the top figure shows the left-half of the TQFP on which the grating was replicated.

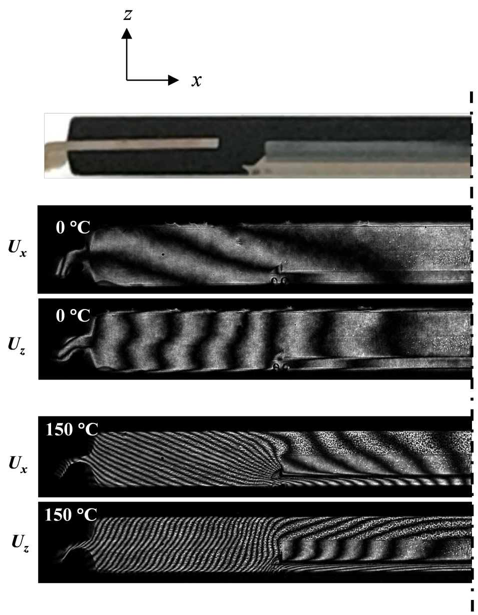

Figure 6.7: Ux and Uz displacement fields of the left-half of the TQFP obtained at 0° and 150°.

6.3. SIMULATION DATA

A simulation data set is extracted from Finite Element Method (FEM) simulations. It is composed of 21 different thermo-mechanical simulations considering different delamination profiles constructed based on the SAM images. The FEM model simulations are performed using ANSYS.

Detail on the model is shown in Fig. 6.8. On the zoom image to the right, can be seen:

- On the lower side of the beige color its located the copper heat dissipator.
- On top of the heat dissipator in orange color, there is the silicon die. On the top face of the die is where the sensing cells are located.
- Between the heat dissipator and the silicon die, there is glue on magenta color.
- On the side, the connection terminals are shown in beige color. These are connected with wires to the sensors on top of the silicon die.
- On the four sides of the die, additional glue can be seen in the color blue.
- Around the die, and containing one end of the connection terminals, it is the molding compound on cyan color.

A visualization of the mesh of the model is shown in Fig. 6.8. The molding compound is modeled using second-order solid tetrahedral elements. All other regions are modeled using second-order solid hexahedral elements.

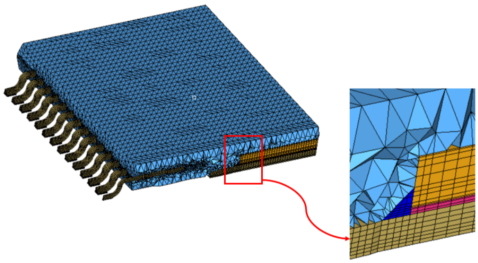

Figure 6.8: Detail on FEM mesh of a quarter model TV TQFP.

Component	Young's [GPa]	Poisson's ratio Modulus	CTE below T_g [ppm/K]	T_g [$^\circ C$]
Outer Mold	22ö32	below T_g : 0.25ö0.3 above T_g : 0.4ö0.46	8ö11E-06 2.3ö3.2E-05	90ö110
Lead Frame	75000	0.343	1.7E-05	-
Stress Sensor	x:168.9E+03 y:168.9E+03 z:130.2E+03	ν_{xz} : 0.064 ν_{xy} : 0.361 ν_{yz} : 0.361	2.8E-06	-
Die attach	7632	below T_g : 0.35 above T_g : 0.45	5.10E-05 1.71E-04	37.55

Table 6.1: Material properties.

Moiré measurements are used to calibrate the component simulation model. Optislang software is used to run an optimization task to minimize the root mean square error between the moiré measurements and simulation. Ranges in values of Young's Modulus, Poisson's ratio, coefficient of thermal expansion, and glass transition temperature of the molding compound are therefore chosen as shown in Figure 6.1. Displacements extracted on x and z direction along a horizontal line in the simulation are extracted and can be depicted in Figure 6.9a, 6.9b. A good agreement between simulation and measurements can be seen after the optimization task is performed. A quarter model is built with half symmetry along one direction and free surface along the other direction as boundary conditions. The moiré data is extracted along the free surface, which corresponds to the cut in the TQFP. Simulation results are extracted at 0řC and 150řC with the corresponding room temperature reference.

A second validation is performed on a component level TQFP to establish the agreement between stress measurements and simulation. This is also a reference for how the stress distribution looks like in the healthy samples. Then the simulation is updated with the printed circuit board (PCB) to mimic the reliable TV.

The values of relative stress along the x and y direction on top of the die and the stress difference calculation for the TQFP component alone from the simulation are shown in Figure 6.10. This gives us a better understanding of what the sensor can measure, which is the stress difference.

The modeling predictions are compared with the measured stress difference data from a component alone in Figure 6.11. The results show good agreement. The deviations are attributed to the uncertainties of the stress sensor, geometry imperfections

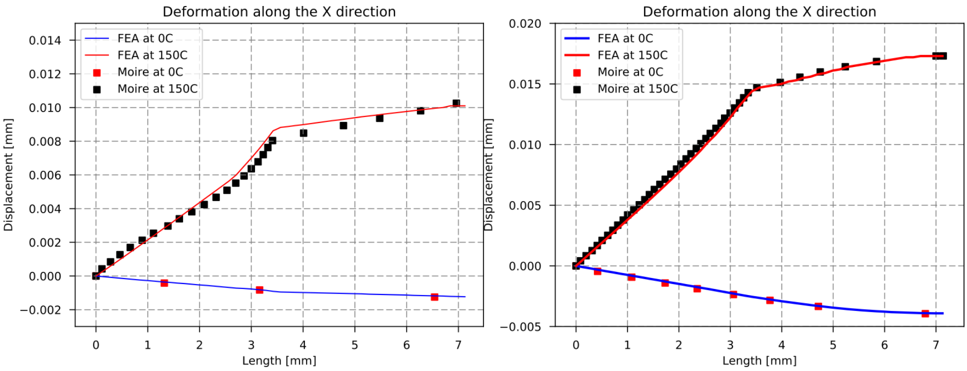

(a) Ux displacement along x direction. Simulations vs. Moiré measurements.

(b) Uz displacement along z direction. Simulations vs. Moiré measurements.

Figure 6.9: FEM ETV model.

(variations), and the material properties used in the simulation. It is worth mentioning that the minimum and maximum values of stress difference are located near the edges.

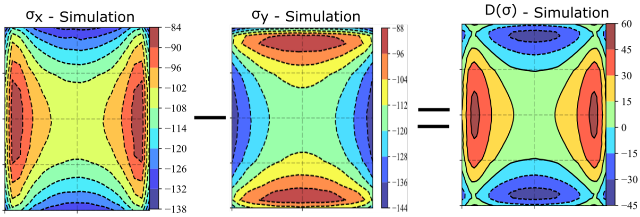

Figure 6.10: TQFP component level mechanical stress at the top of the die. Loading condition used in the simulation is an environmental temperature of −40° and 150°. The stress values at −40° are extracted from 150° stress values.

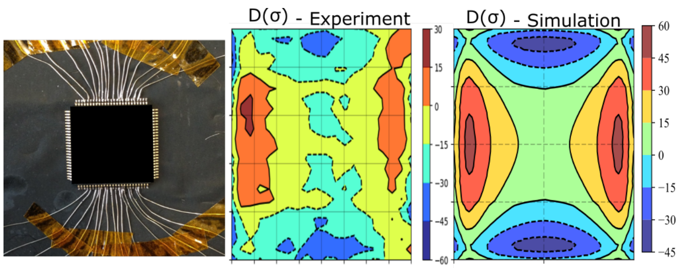

Figure 6.11: TQFP component level mechanical stress at the top of the die measured vs. simulation. Loading condition used in the simulation and measurement is an environmental temperature of −40° and 150°. The stress values at −40° are extracted from 150° stress values.

PCB level delaminated TQFP simulation is constructed based on the SAM image shown in Figure 6.5. The stress values along the x and y direction when the delamination is present are depicted in Figure 6.12. This visualization has the purpose of showing the link between delamination, the stresses along the x and y direction, and the stress difference. Also, this is an efficient indication that the stress difference values can capture the delamination.

The exact amount of contact area shown in the SAM image (Figure 6.5) is used for modeling the delamination in the simulation. The interface mesh node is divided into two mesh nodes with no connection in the area where delamination is considered. In the other areas, node to node connectivity is maintained.

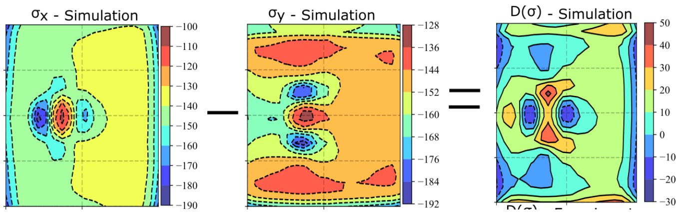

Figure 6.12: Simulation mechanical stress at the top of the die of the delaminated $MC1\_1$ TV. Loading condition used in the simulation is an environmental temperature of $-40°$ and $150°$. The stress values at $-40°$ are extracted from $150°$ stress values.

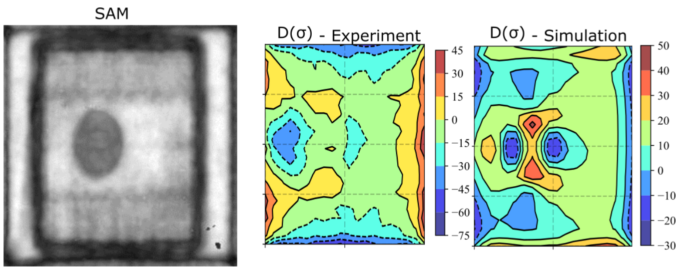

Figure 6.13: Simulation and measured mechanical stress difference at the top of the die of the delaminated $MC1\_1$ TV. Loading condition used in the simulation is an environmental temperature of $-40°$ and $150°$. The stress values at $-40°$ are extracted from $150°$ stress values.

Figure 6.13 shows the contour plot of the relative stress difference from both simulation and measurement with the designated delamination area shown in the SAM image. Even in this case, the agreement is good between the measurement and the simulation in the undelaminated area, despite the limitation of the method used in simulating the delamination area. Both plots show similar stress distribution where the undelaminated area is present. The distribution near the undelaminated area is similar as in the case of Figure 6.11. Overlay pictures between the stress difference and SAM image of both simulation and measurement are shown in Figure 6.14. The top/bottom and left/right stress distribution of maximum and minimum values are exactly on top of the edge of the undelaminated area.

Although the stress difference gives an indication of where the delamination areas are present, these are visible only when the package is fully delaminated. When the delamination areas are closer to the edges of the adhesive layer, it is visually difficult to estimate where the delamination is located. One such examples is depicted in Figure 6.15. Therefore, one more intermediate step is needed to reveal the delamination areas.

From the FEM simulation is observed that σ_z extracted at the adhesive layer describes the delamination area much better, as depicted in Figure 6.16. The image shows a top view on the model, where the grey color represents the delaminated area and the

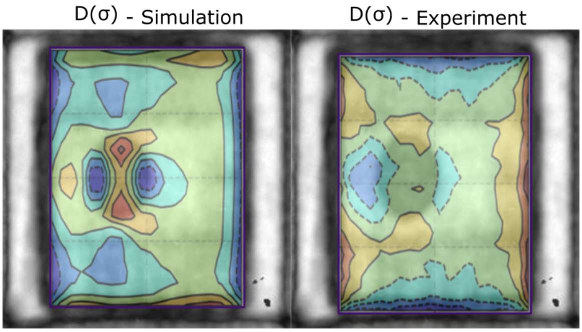

Figure 6.14: $MC1\_1$ TV overlay picture of stress difference on top of SAM image. Both simulation and experiment gives a very good indication where there is still contact underneath the die.

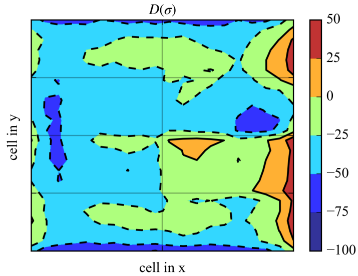

Figure 6.15: $MC1\_1$ TV stress difference at 1400 Cycle.

red undelaminated area, respectively.

The simulation dataset contains the values of $D(\sigma)_{ij}^{rel}$ on each element on the top face of the silicon die, where the sensing cells would be located, and σ_z of all elements on the lower side of the silicon die. The element geometry has been designed, so the top and lower faces contain a $2*3$ array of mesh elements. In total, 21 simulations are performed containing different delamination areas based on the SAM images taken during and at the reliability tests.

The simulation returns two types of data:

- $D(\sigma)_{ij}^{rel}$ on the top face of the silicon die: The simulation gives as output the relative stress difference between the peak low temperature and the peak high temperature. With this values per element, visualizations as in Fig. 6.13 can be created.

- σ_z on the lower face of the silicon die: The simulation calculates the σ_z. Visualization of one of these images is shown in Fig. 6.16.

As depicted in Figure 6.16, σ_z describes the delamination well in comparison to the $D(\sigma)_{ij}^{rel}$, where it is hard to make a visual correlation between the stress and delamination. Therefore, the values of predicted σ_z are chosen as a virtual sensor to show where the delamination area is located.

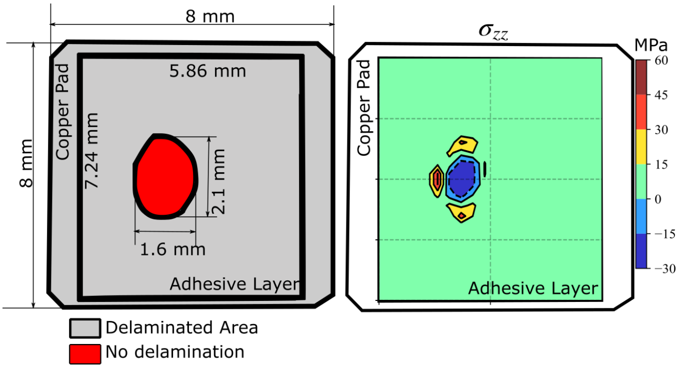

Figure 6.16: Delaminated area versus σ_z on simulation dataset. Grey area represents the delaminated area and in the simulation is given as a no contact interface. The red area represents no delaminated area and in the simulation is given as a bonded contact interface.

6.4. SURROGATE MODELLING

The amount of cells provides a very good resolution of the stress difference distribution over the surface of the silicon die. However, to predict the delamination by just looking at the stress difference is not trivial, as discussed in the previous section. Machine learning is used to cope with this problem. In this chapter, as an initial step, a model is trained with the 21 delaminated simulation data with the stress difference as the input and σ_z at the interface between glue and silicon die as the output. Virtual Twin by Surrogate modeling technique is shown in Figure 6.17. FEM simulation snapshots are used to train the correlation between the stress difference on top of the silicon die and the out-of-plane stresses on the adhesive layer. Further, the trained NN is used to predict the out-of-plane stresses based on the measured stress difference from different delaminated TVs.

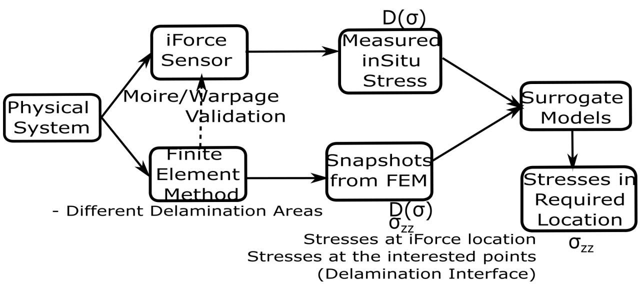

Figure 6.17: Surrogate Modelling.

6.4.1. BACK PROPAGATION ARTIFICIAL NEURAL NETWORK

Nowadays, a set of techniques shines for their performance called Artificial Neural Networks (ANN). A simple representation of a Feed-Forward Artificial Neural Network can be seen in Figure 6.18. By themselves, ANN is not a method but a tool to collaborate between methods towards a common goal. An ANN is a collection of Artificial Neurons;

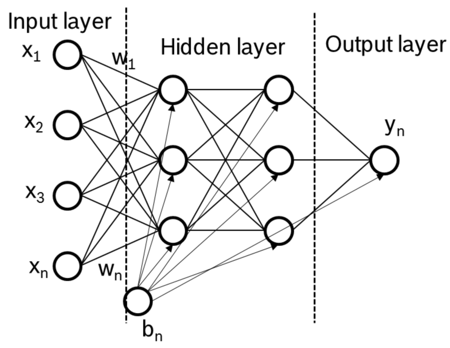

Figure 6.18: Visual representation of an Artificial Neural Network.

therefore, it is necessary to review what it is and what it does a single Artificial Neuron (AN).

ANs have been inspired in biology in the way it keeps a biological structure aiming to replicate a biological function[7] On Figure 6.19 it can be seen a comparison between a biological neuron (6.19a) and an artificial neuron (6.19b).

The most basic model that can be used on AN is a Perceptron. Frank Rosenblatt invented this linear model in 1958[26].

Neural Networks consist of the following components:

- An input layer, x
- An output layer, y
- A set of weights and biases between each layer, W and b
- A choice of activation function for each hidden layer, σ

Having a set of data points organized in the matrix **X** that is formed by individual data points vectors **x**. The model comprises a mathematical function as in equation 6.5.

$$y(x) = f(w \times x) + b \tag{6.5}$$

This means if we know weight matrix w and bias vector b, under the chosen activation function f, we can predict unknown output value y, by known input vector x. Input vector x is always known, so how to get weight matrix w and the bias vector b becomes the key problem, precisely the purpose of ANN training.

Most used activation functions are step, sign, sigmoid[8], tanh[9] and ReLU[10]:

[7] This is a common practice in Engineering: In the same fashion the wing of a plane preserves its general structure, replicating a specific function of a biological wing. ANs keep the structure of a biological neuron and loosely replicate a biological neuron's biological function.

[8] Also called logistic function.

[9] Hyperbolic tangent function.

[10] Rectified linear unit.

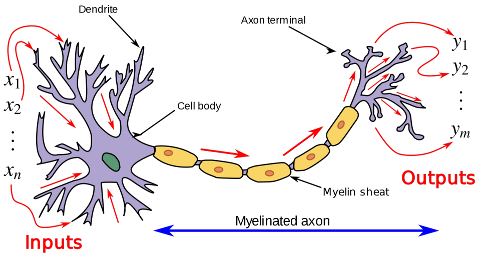

(a) Biological neuron[25].

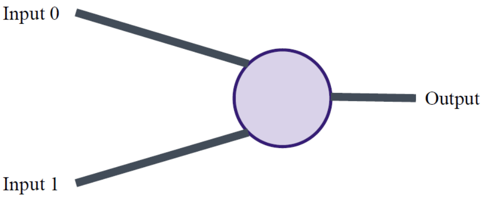

(b) Artificial Neuron.

Figure 6.19: Comparison between biological and artificial neurons.

$$step(z) = \begin{cases} 1 & \text{if z} \geq 0; \\ 0 & \text{if z} < 0. \end{cases} \tag{6.6}$$

$$sign(z) = \begin{cases} 1 & \text{if z} \geq 0; \\ -1 & \text{if z} < 0. \end{cases} \tag{6.7}$$

$$sigmoid(z) = \frac{1}{1+e^{-z}} \tag{6.8}$$

$$tanh(z) = \frac{e^z - 1}{e^z + 1} \tag{6.9}$$

$$ReLU(z) = max(0, z) \tag{6.10}$$

$$identity(z) = z \tag{6.11}$$

The selection of the activation function depends on what type of behavior the perceptron is designed to abstract from the data that will feed it. Like this, a perceptron with a sign activation function would be used for linear classification tasks, a perceptron with an identity activation function would be used for linear regression, and a perceptron with a sigmoid activation function would be used for logistic regression.

Backpropagation (BP) is a method used in artificial neural networks to calculate the error contribution of each neuron after a batch is processed. An enveloping optimization algorithm uses this to adjust the weight of each neuron, completing the learning process for that case. We predict the input part of training data by the current neural network, and this is usually called forward propagation. And we get a set of output data, which has differences from the output part of the training data; this is an error. In the optimization algorithm, this error is named loss function, and our goal is to optimize the parameters of the network to make the loss function reach its minimum point. This means the neural network fits the training data and can represent the real model. Technically it calculates the gradient of the loss function to reach the optimization goal. It is commonly used in the gradient descent optimization algorithm. It is also called backward propagation of errors because the error is calculated at the output and distributed back through the network layers to adjust all the parameters inside the network. This BP method has limitations because it is a gradient-based optimization method, so BP is not guaranteed to find the global minimum of the loss function, maybe just a local minimum. This can be solved by making some improvements, such as:

- add momentum factor to make learning rate adaptive
- training more times, then we may get the global minimum at a larger probability
- combining other optimization algorithms into BP, for example, Particle Swarm Optimization, Genetic algorithm, etc.

Learning rate can be regarded as an improvement step, represent how far we take the next step towards the negative gradient direction. If this value is big, we only need several steps (iterations) to approach the minimum point, which means faster convergence and time-saving. There are many rule-of-thumb methods for determining an adequate number of neurons to use in the hidden layers, such as the following: the number of hidden neurons should be between the size of the input layer and the size of the output layer. The momentum factor can be regarded as an adjustment of the learning rate to make the step length no longer fixed; thus, it can realize large steps at the beginning to make the loss function drop fast and shrink the step when approaching the minimum.

For our application, the input data contains the relative stress difference from all the 480 cells from 21 simulation data. The output data contains σ_z from all the corresponding 480 cells on the interface with the glue.

A Surrogate Model is constructed using a model of the outcome that is looked upon instead of real-world measures. This technique is used when the real world measures are impossible to obtain (like in the case of theoretical physics models), are computationally expensive (for example, for complex FEM simulations), or precise physical measures are hard to obtain (out of plane stresses in our case).

Because of the few amount of data points, this model will be trained with the whole simulation data set that includes all 21 delamination profiles. Then the results will be evaluated using SAM scans of the last state of the TVs. The input is a 480 signal corresponding to the 480 stress difference signals of the sensors that would be located on the top of the silicon of the TV, and the output is a 480 signal corresponding to the σ_z on the locations directly opposite to them on the other side of the silicon (interface with adhesive).

The BPNN architecture is as shown on Table 6.2:

Parameter	Value
Hidden layers	[100,]
Activation function	ReLU
Solver	SGD
Learning Rate	0.0001
Max iterations	2200
Tolerance	0.0005
Max iterations under tolerance	30
Momentum	0.1

Table 6.2: BPNN parameters.

A summary of the results obtained is shown in the appendix in Fig. 6.20. On these images, the output corresponding to the last thermal cycle of the module's experimental data sets is shown beside the SAM scan of its last state for comparison. A visual examination shows that the simple network created with the small simulation dataset has been able to predict the final delamination state of the TV to a certain degree. The maximum values of out-of-plane stresses are located at the boundary between the delaminated and not delaminated area, seen in the SAM images.

In Figure 6.20d it is observed that the σ_z prediction reveals the delamination area is located around the edge of the adhesive layer. The SAM image validates this. In this current form, the NN algorithm tries to fit the measurement data to one of the delamination profiles given to the simulation. It is therefore not able to interpolate between the delamination areas. Therefore, a generalization of this model is possible only when sufficient delamination profile data are available from the simulation.

6

6.5. CONCLUSIONS

In this chapter, a surrogate model based on simulated in-plane and out-of-plane stress are proposed. Mechanical stresses are able to capture structural change in the packages, including delamination. The BP NN model shows promising results to estimate the delamination areas inside the package. This non-intrusive method can be used to test new package designs, which can lead to better and fast designs. Also, it has the potential to be used in Digital Twin for automotive electronics as virtual sensors. Future work should be focused on acquiring more testing data for different designs and implementing more efficient FEM and ML methods.

REFERENCES

[1] A. Prisacaru, E. O. Guerrero, B. Chimmineni, P. J. Gromala, Y.-H. Yang, B. Han, and G. Q. Zhang, *Towards virtual twin for electronic packages in automotive applications,* Microelectronics Reliability **122**, 114134 (2021).

[2] S. Hosseini, K. Barker, and J. E. Ramirez-Marquez, *A review of definitions and measures of system resilience,* Reliability Engineering & System Safety **145**, 47 (2016).

[3] *24765-2017 - ISO/IEC/IEEE International Standard - Systems and software engineering–Vocabulary - IEEE Standard,* .

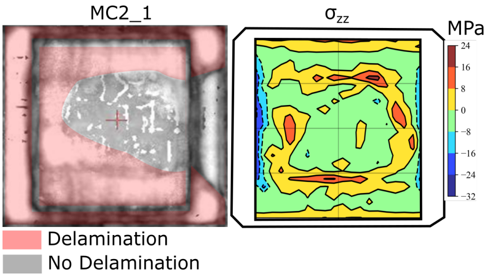

(a) σ_z surrogate modelling prediction at the end of TC.

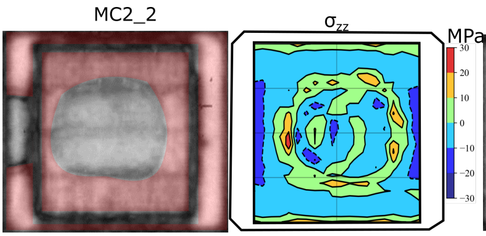

(b) σ_z surrogate modelling prediction at the end of TC.

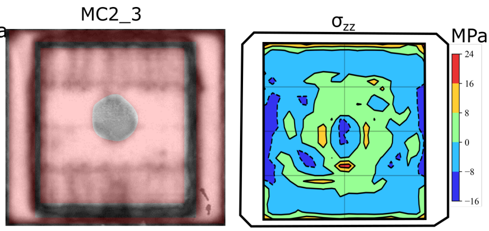

(c) σ_z surrogate modelling prediction at the end of TC.

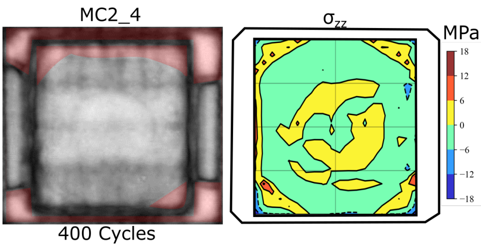

(d) σ_z surrogate modelling prediction at 400 TC.

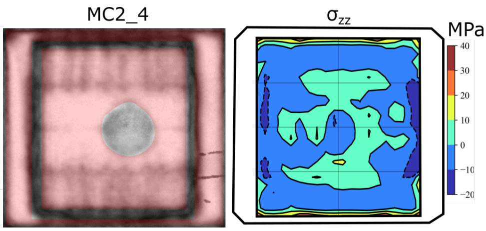

(e) σ_z surrogate modelling prediction at the end of TC.

Figure 6.20: SAM images versus the surrogate modeling predictions.

[4] C. B. Nielsen, P. G. Larsen, J. Fitzgerald, J. Woodcock, and J. Peleska, *Systems of systems engineering: Basic concepts, model-based techniques, and research directions,* ACM Comput. Surv. **48**, 18:1 (2015).

[5] W. Denson, *The history of reliability prediction,* **47**, SP321.

[6] D. Crowe and A. Feinberg, eds., *Design for Reliability*, Electronics Handbook Series, Vol. 7 (CRC Press, 2001) dOI: 10.1201/9781420040845.

[7] M. Xie and C. Lai, *Reliability analysis using an additive weibull model with bathtub-shaped failure rate function,* Reliability Engineering & System Safety **52**, 87 (1996).

[8] H. Tanaka, L. T. Fan, F. S. Lai, and K. Toguchi, *Fault-tree analysis by fuzzy probability,* **R-32**, 453.

[9] E. Glaessgen and D. Stargel, *The digital twin paradigm for future nasa and u.s. air force vehicles,* (2012).

[10] *Spotlight on automotive, pwc semiconductor report,* Accessed: 2019-02-04.

[11] DeepMind, *Alphago,* (2010), [Online; accessed 6th of January, 2019].

[12] A. C. Mueller and S. Guido, *Introduction to machine learning with Python: a guide for data scientists,* first edition ed. (O'Reilly Media, Inc) OCLC: ocn895728667.

[13] T. Bayes, *An essay towards solving a problem in the doctrine of chances,* Phil. Trans. of the Royal Soc. of London **53**, 370 (1763).

[14] DOMO, *Data never sleeps 5.0,* (2018), [Online; accessed 6th of January, 2019].

[15] DOMO, *Data never sleeps 6.0,* (2019), [Online; accessed 6th of January, 2019].

[16] A. Wang, *An industrial strength audio search algorithm,* in *ISMIR* (2003).

[17] Y. Taigman, M. Yang, M. Ranzato, and L. Wolf, *Deepface: Closing the gap to human-level performance in face verification,* in *Conference on Computer Vision and Pattern Recognition (CVPR)* (2014).

[18] A. Prisacaru, A. Palczynska, P. J. Gromala, B. Han, and G. Q. Zhang, *Condition monitoring algorithm for piezoresistive silicon-based stress sensor data obtained from electronic control units,* 2017 IEEE 67th Electronic Components and Technology Conference (ECTC) , 1119 (2017).

[19] A. Palczynska, A. Prisacaru, P. J. Gromala, B. Han, D. Mayer, and T. Melz, *Towards prognostics and health monitoring: The potential of fault detection by piezoresistive silicon stress sensor,* in *Thermal, Mechanical and Multi-Physics Simulation and Experiments in Microelectronics and Microsystems (EuroSimE), 2016 17th International Conference on* (IEEE) pp. 1–8.

[20] A. Prisacaru, A. Palczynska, P. Gromala, B. Wu, B. Han, and G. Zhang, *Accuracy of cmos-based piezoresistive stress sensor for engineering applications of thermal loading condition: Theoretical review and experimental validation,* IEEE Sensors Journal **19**, 9139 (2019).

[21] B. H. D. Post and P. Ifju, eds., *High Sensitivity Moire: Experimental Analysis for Mechanics and Materials* (Springer-Verlag, 1997).

[22] B. Han, *Thermal stresses in microelectronics subassemblies: quantitative characterization using photomechanics methods,* Journal of Thermal Stresses , 583 (2003).

[23] B. Wu and B. Han, *Advanced mechanical/optical configuration of real-time moire interferometry for thermal deformation analysis of fan-out wafer level package,* IEEE Transactions on Components, Packaging and Manufacturing Technology **8** (2018).

[24] B. Han, *Recent advancements of moire and microscopic moire interferometry for thermal deformation analyses of microelectronics devices,* Experimental Mechanics **38**, 278 (1998).

[25] Prof. Loc Vu-Quoc, *Neuron3,* (2018), [Online; accessed 6th of January, 2019].

[26] F. Rosenblatt, *The perceptron: A probabilistic model for information storage and organization in the brain,* Psychological Review , 65 (1958).

7

Concluding Remarks and Recommendations

Results obtained in Chapters 4, 5, and 6 look promising in predicting a simplified degradation model and a whole degradation state using ML models. Although these models included trade-offs like execution time or precision on behavior abstraction, they have proved that the concept is valid. More research is required in this area, as more experiments are necessary to develop faster and more precise models for degradation prediction. The models were trained on this Thesis using data from different sources, including different experimental setups. Nevertheless, the good performance of these models hints at a bright future in this area of research as more data is available and the preprocessing methods perfected. With the notorious success of the developed models, it can be stated that the raw data preprocessing methodology developed has been validated. Nevertheless, there is room for improvement in the Python scripts developed in running time efficiency and automation to expedite the process. As part of the proposed methodology, it was suggested to train the models with smoothed and non-smoothed data sets. The smoothed data set was believed to expedite the training process of the Neural Network but, in practice, failed to do so. The results obtained with the smoothed data set have not been shown on this Thesis as the models did not perform as expected. This outcome hints that the final smoothing process destroyed information contained in the data that was relevant to an accurate degradation estimation. For further research, it is advisable to try other techniques to speed up the NN training process as dimensionality reduction. The surrogate modeling returned promising results. The trained NN activates in the region around the real-world not delaminated area. Although its accuracy leaves room for improvement, it must be noted that the model was trained using only 21 simulation data. If there would be a more considerable simulation data set, the model's performance would probably improve. Finally, some remarks are listed as a guide for further research: It is recommended to keep variables like running cycles and ADC selection fixed in further experimental data gathering to have a more complete raw data set. Having a standardized experimental setup may improve the power of the models, as some variability will be taken out of the system. ESN has been a reliable option for degradation prediction using (i) exclusively experimental data and (ii) merged experimental and simulation data. It is recommended to keep testing its performance on bigger data sets. The inclusion of simulation data to the training data set has successfully introduced information that was not present on the experimental data set. While this concept has been tested and validated in this Thesis, there must be room for improvement on the merging process that includes the upscaling of the simulation data. In the future, the requirement of data upscaling may be eliminated in the case in which a considerably big simulation set exist. It is encouraged to further research to generate data set and evaluate other methods that could help share information of experimental and simulation sets to the final data set.

Some additional general remarks regarding data approaches:

- Data is found more important than which ML method to use. Preprocessing the data takes more time than training a good model.
- There are many ways how to extract what you are looking for from the data.
- Which ML method to be used is problem dependent, and the choice is based on experience or trial and error method.
- The output information must be integrated into the data, and engineering knowledge must be used. ML will not find something that is not found in the data.
- Generalization of ML methods is still a concern (Robustness). Not only the ML model must learn, but also the creator of the models.
- Additional Engineering information can be added to improve the model.

SUMMARY

This thesis describes a series of experiments, algorithms, and methodology development for implementing Prognostics and Health Management (PHM) in the field of automotive electronics. Furthermore, a new PHM framework is proposed explicitly tailored for the harsh environment electronics. In addition, the entire apparatus is built, such as the sensing capabilities of electronic packages and control units. A central PHM ECU is also developed to acquire the signal from sensors, process it, and perform calculations.

In Chapter 2 a strong literature review is performed. It is found that the concept is widely referenced in different electronic applications. Although different tries are performed, the literature mostly presents the framework on how this concept might work, but very few are showing concrete results. Even in these cases, most of them are statistically or monitoring-based; none of them reported quantitative prognostic values. There were and still many gaps in PHM for electronics, resulting in a rich environment for future research. Its necessity is still not yet fully understood, and the skepticism comes from the fact that it is not widely known that PHM is not something that needs to be developed from scratch. Most of its functions are or will be in electronic systems. Therefore, One must further develop only the interactions between these functions and the algorithms. One strong advantage of PHM is that until the system is mature enough to predict anything, the data gathered in between will help building experience, knowledge, and new insights about the product. In the end, this will only improve the product quality but also will help to optimize it for specific applications.

Most of the failures in the electronics are coming from the thermomechanical loads that cause different changes in the structure, which in the end will cause electric failure. Therefore, in this thesis, a unique sensor in chosen as data collected based on the piezoresistivity concept. The main idea is that when a thermomechanical or just a mechanical load is applied, corresponding stress arises inside of the structure. The piezoresistivity effect is a change in the current of a semiconductor when that stress is present. Therefore, the stress can be calculated based on these current changes, especially when the length changes are neglected due to the small size of the transistor. How these tiny mirrored piezoresistive transistors work in the field of reliability, its basics, accuracy, and usage are widely described in Chapter 3. Its capability and uncertainty are validated using high precision measurement techniques like Moiré optical measurement and numerical methods. The most prominent advocate for such a sensor is its high sensitivity to global and local changes in the structure. The stress measurement detects any slight change in the material property, dimension, rigidity, and composition in the structure. It makes the ideal sensor for any PHM application in electronics. Just as a side comment, a temperature sensor will only be sensitive to structural changes in power electronics applications due to high-temperature fluctuations. However, a piezoresistive silicon-based stress sensor can be used in all electronic applications, including power electronics. Of course, its location depends on the failure and application. This thesis presents two use

cases; in one, an overmolded ECU encapsulates a dedicated sensor. In the other case, an electronic package encapsulates the silicon die sensor.

The overmolded ECU algorithm development and application for fault detection and classification is described in Chapter 4. A unique algorithm is proposed and implemented to handle the data obtained from the piezoresistive stress sensing cells. The accuracy of measured data is examined by the Finite Element Method (FEM), and the physical changes are validated with Scanning Acoustic Microscope (SAM). One-class support vector machines are used to autonomously classify data based on a training set of measurements from a healthy state. The reported results confirm that robust classification is possible based on data from the silicon stress sensor. The experimental data contained only the fault information imposed from the beginning during the production phase. However, this data is linked with the delamination propagation between the molding compound and the PCB. Some initial Machine Learning (ML) methods determine whether such tools are feasible for this type of data. The initial findings are satisfactory, but the quality of data is still not yet ideal because of the apriori fault and the number of samples.

A second iteration presents the piezoresistive stress sensors encapsulated inside of the electronic package. A more excellent resolution for capturing more data and effects is desired; therefore, the 480 sensing cells replace the functional die. The new framework and the hardware provides features like connectivity, computational power, and security. The high precision stress measurements are performed during the reliability testing. In total, 2880 sensing cells are measured from 6 electronic packages. In one of the samples, 2500 temperature cycles are completed and provided accurate data regarding the failure. The 480 stress sensing cells continuously recorded the healthy state to the crack initiation and to complete delamination. An additional four samples of data drift in the stress measurements are recorded, but no significant change is observed in one sample. Failure analysis like Scanning Acoustic Microscope (SAM) and cross-sectioning of the samples confirmed the delamination and the drift in the stress data. SAM showed No delamination in the case of no stress data drift.

Chapter 5 describes in detail the experiments and their validation. In addition, it represents the methodology and algorithm applied to this type of data. One of the requirements today in the Internet of Things (IoT) applications in automotive is that the algorithms must be as simple and must use significantly less power. One of the IoT applications in automotive is to provide prognostics for its electronics. Therefore, an entire chain of simple methods and algorithms describes the failure features such as location, detection, and type. In addition, an Echo State Network is used to estimate and predict the degradation in the package. Nevertheless, the results show that the proposed framework is validated and can work in simple hardware such as Raspberry Pi. Data-driven approaches, mainly used in this chapter, provide the opportunity to monitor the asset during operation and understand the asset behavior based on its current design.

Chapter 6 shows how the numerical methods validate the results from experiments. The simulated stress distribution over the silicon die during delamination coincides with the measurement's one. Therefore, the model-based approach, in this case, numerical methods, connects with the data-driven one. In Chapter 6 a first Virtual Twin is built based on this fusion. A methodology is described in detail where the data exclusively from the simulation trains a neural network to represent delamination. Afterward, data from measurements are used as testing data for this model. Promising results are shown with certain accuracy in describing the delamination, but further data is required to improve the model. In Chapter 7 the conclusions of the thesis are discussed and gives an outlook towards future work. A discussion regarding data and its importance is also discussed.

SAMENVATTING

Deze dissertatie beschrijft een reeks experimenten, algoritmen en methodologie-ontwikkeling voor het implementeren van Prognostics and Health Management (PHM) op het gebied van auto-elektronica. Verder wordt een nieuw PHM raamwerk voorgesteld dat expliciet is toegesneden op elektronica voor ruwe omgevingen. Bovendien wordt het volledige apparaat gebouwd, waaronder de detectiecapaciteiten van elektronische pakketten en controle-eenheden. Ook wordt een centrale PHM ECU ontwikkeld om het signaal van sensoren te ontvangen, te verwerken en berekeningen uit te voeren.

In Hoofdstuk 2 wordt een sterk literatuuronderzoek verricht. Gebleken is dat in verschillende elektronische toepassingen veelvuldig naar het concept wordt verwezen. Hoewel verschillende pogingen zijn gedaan, presenteert de literatuur meestal het raamwerk over hoe dit concept zou kunnen werken, maar slechts weinige laten concrete resultaten zien. Zelfs in deze gevallen zijn de meeste van hen statistisch of op monitoring gebaseerd; geen van hen rapporteerde kwantitatieve prognostische waarden. Er waren en zijn nog steeds veel gaps in PHM voor elektronica, waardoor er een rijke omgeving is voor toekomstig onderzoek. De noodzaak ervan wordt nog steeds niet volledig begrepen, en de scepsis komt voort uit het feit dat niet algemeen bekend is dat PHM niet iets is dat van de grond af moet worden ontwikkeld. De meeste functies ervan bevinden zich of zullen zich bevinden in elektronische systemen. Men moet dus alleen de interacties tussen deze functies en de algoritmen verder ontwikkelen. Een sterk voordeel van PHM is dat, totdat het systeem volwassen genoeg is om iets te voorspellen, de tussentijds verzamelde gegevens zullen helpen bij het opbouwen van ervaring, kennis en nieuwe inzichten over het product. Uiteindelijk zal dit alleen de kwaliteit van het product verbeteren, maar ook helpen om het te optimaliseren voor specifieke toepassingen.

De meeste defecten in de elektronica zijn afkomstig van thermomechanische belasting die verschillende veranderingen in de structuur veroorzaken, die uiteindelijk elektrische defecten zullen veroorzaken. Daarom is in dit proefschrift gekozen voor een unieke sensor die gegevens verzamelt op basis van het concept van piëzoresistiviteit. Het hoofdidee is dat wanneer een thermomechanische of gewoon een mechanische belasting wordt uitgeoefend, overeenkomstige spanningen ontstaan binnenin de structuur. Het piëzoresistiviteit effect is een verandering in de stroom van een halfgeleider wanneer die spanning aanwezig is. Daarom kan de spanning worden berekend op basis van deze stroomveranderingen, vooral wanneer de lengteveranderingen worden verwaarloosd vanwege de kleine afmetingen van de transistor. Hoe deze kleine gespiegelde piëzoresistieve transistors werken op het gebied van betrouwbaarheid, de basisprincipes, nauwkeurigheid en gebruik worden uitgebreid beschreven in Hoofdstuk 3. De bruikbaarheid en de onzekerheid worden gevalideerd met behulp van zeer nauwkeurige meettechnieken zoals optische Moiré metingen en numerieke methoden. Het meest prominente voordeel van een dergelijke sensor is zijn hoge gevoeligheid voor globale en lokale veranderingen in de structuur. De spanningsmeting detecteert elke kleine

verandering in de materiaaleigenschappen, afmeting, stijfheid en samenstelling in de structuur. Het is de ideale sensor voor elke PHM-toepassing in de elektronica. Terzijde: een temperatuursensor zal alleen gevoelig zijn voor structuurveranderingen in vermogenselektronica als gevolg van hoge-temperatuurschommelingen. Een piëzoresistieve op silicium gebaseerde spanningssensor kan echter in alle elektronische toepassingen worden gebruikt, ook in de vermogenselektronica. Uiteraard is de plaats ervan afhankelijk van de storing en de toepassing. Deze dissertatie presenteert twee gebruikssituaties; in het ene geval wordt een speciale sensor ingekapseld in een overmolded ECU. In het andere geval kapselt een elektronisch pakket de silicium-die sensor in.

De ontwikkeling van het overmolded ECU algoritme en de toepassing voor foutdetectie en classificatie wordt beschreven in Hoofdstuk 4. Er wordt een uniek algoritme voorgesteld en geïmplementeerd om de gegevens van de piëzoresistieve spanningsmetende cellen te verwerken. De nauwkeurigheid van de gemeten gegevens wordt onderzocht met de Finite Element Method (FEM), en de fysieke veranderingen worden gevalideerd met Scanning Acoustic Microscope (SAM). One-class support vector machines worden gebruikt om autonoom gegevens te classificeren op basis van een trainingsset van metingen uit een gezonde toestand. De gerapporteerde resultaten bevestigen dat robuuste classificatie mogelijk is op basis van gegevens van de silicium spanningssensor. De experimentele gegevens bevatten alleen de foutinformatie die vanaf het begin tijdens de productiefase is opgelegd. Deze gegevens houden echter verband met de delaminatie voortplanting tussen de vormmassa en de printplaat. Enkele initiële Machine Learning (ML) methoden bepalen of dergelijke hulpmiddelen haalbaar zijn voor dit soort gegevens. De eerste bevindingen zijn bevredigend, maar de kwaliteit van de gegevens is nog niet ideaal vanwege de a priori fout en het aantal monsters. Een tweede iteratie presenteert de piëzoresistieve spanningssensoren ingekapseld in de elektronische verpakking. Een nog excellentere resolutie voor het vastleggen van meer gegevens en effecten is gewenst; daarom vervangen de 480 sensing cellen de functionele chip. Het nieuwe raamwerk en de hardware bieden eigenschappen als connectiviteit, rekenkracht en veiligheid. De zeer nauwkeurige stressmetingen worden uitgevoerd tijdens de betrouwbaarheidstests. In totaal worden 2880 meetcellen gemeten van 6 elektronische pakketten. In één van de monsters zijn 2500 temperatuurcycli doorlopen en deze leverden nauwkeurige gegevens op over het defect. De 480 spanning-meetcellen registreerden continu de gezonde toestand tot de scheur initiatie en tot volledige delaminatie. In nog eens vier monsters zijn gegevensdrift in de spanningsmetingen geregistreerd, maar in één monster is geen significante verandering waargenomen. Faalanalyse met behulp van een Scanning Acoustic Microscope (SAM) en dwarsdoorsneden van de monsters bevestigden de delaminatie en de drift in de spanningsgegevens. SAM toonde geen delaminatie in het geval van geen spanningsafwijking.

Hoofdstuk 5 beschrijft in detail de experimenten en hun validatie. Bovendien geeft het de methodologie en het algoritme weer die op dit soort gegevens zijn toegepast. Een van de eisen die tegenwoordig worden gesteld aan Internet of Things (IoT)-toepassingen in de automobielsector is dat de algoritmen zo eenvoudig mogelijk moeten zijn en aanzienlijk minder stroom moeten verbruiken. Een van de IoT-toepassingen in de automobielsector is het leveren van prognostiek voor de elektronica. Daarom beschrijft een hele keten van eenvoudige methoden en algoritmen de storingskenmerken, zoals locatie, detectie en type. Bovendien wordt een Echo State Network gebruikt om de degradatie in het pakket in te schatten en te voorspellen. Niettemin tonen de resultaten aan dat het voorgestelde kader gevalideerd is en kan werken in eenvoudige hardware zoals Raspberry Pi. Data-gedreven benaderingen, voornamelijk gebruikt in dit hoofdstuk, bieden de mogelijkheid om de asset tijdens bedrijf te monitoren en het gedrag van de asset te begrijpen op basis van het huidige ontwerp.

Hoofdstuk 6 laat zien hoe de numerieke methoden de resultaten uit experimenten valideren. De gesimuleerde spanningsverdeling over de siliciummatrijs tijdens delaminatie komt overeen met die van de metingen. Daarom sluit de modelmatige aanpak, in dit geval numerieke methoden, aan bij de gegevensgestuurde aanpak. In Hoofdstuk 5 wordt een eerste Virtual Twin gebouwd op basis van deze samensmelting. Een methodologie wordt in detail beschreven waarbij de data uitsluitend uit de simulatie een neuraal netwerk traint om delaminatie weer te geven. Daarna worden gegevens uit metingen gebruikt als testgegevens voor dit model. Veelbelovende resultaten worden getoond met een zekere nauwkeurigheid in het beschrijven van de delaminatie, maar verdere gegevens zijn nodig om het model te verbeteren. In Hoofdstuk 7 worden de conclusies van het proefschrift besproken en wordt een vooruitblik gegeven op toekomstig werk. Een discussie over data en het belang daarvan wordt ook besproken.

Acknowledgements

Each thesis is built on certain premises. Without them, the final form of this thesis would look very different or not exist at all. Therefore, I would like to show my appreciation for my thesis trio group; each contributed equally to this research success. Many thanks to my promotor Professor GuoQi Zhang for his encouragement and trust in my work. You are probably one of the few people I met who could inspire me to be more, even when I was in doubt. Much appreciation to my daily supervisor, Dr. Premyslaw J. Gromala, which I consider a true friend after all these years, for his valuable discussions and nurturing. These gave birth to many ideas in this thesis. In addition, he was there for me when things got sideways on several occasions, especially in my personal life, for which I thank him. You are an inspiration for me in terms of leadership, engineering, and life in general. My special thanks to the trio member, Professor Bongtae Han, for his detailed and challenging discussion during our meetings. My brain clockwork was always in full speed motion during our talks. You pushed me to think more complex but much clearer at the same time, and you tried to tidy up my disorganized brain.

I want to dedicate this thesis to the memory of my father and mother, Andrei and Elena Prisacaru, which gave me solid and healthy values to rely on. To my father for his guidance in the technical field and the planting the seed for solid analytical thinking. To my mother for giving me her morals and values, which are still intact to this day.

I would also like to thank Dr. Alicja Hellermann for her patience in explaining the electronic principles of how the stress sensor works and for her measurement data used in Chapter 3. In addition, many thanks to the students I worked with in helping me provide results for this thesis, such as Dongwei Wang, Yue Sun, Adrian Schmidt, and Ernesto O. Guerrero. You people showed me how essential teamwork is and how the results depend on.

I want to express my gratitude to Prof. Xuejun Fan for his constructive and elaborated feedback on this thesis and his general advice regarding my Ph.D. journey. Much appreciation goes to Professor Christopher J. Bailey for his detailed corrections and comments regarding this thesis and his fruitful conversations during the EurosimmE conference. Many thanks to the committee members: Prof. Bontae Han, Prof. Xuejun Fan, Prof. Christopher J. Bailey, Prof. Willem D. van Driel and Prof. Said Hamdioui for being present at my defense and for giving me valuable feedback to improve this thesis further.

I would also like to show my appreciation to Dr. Andreas Roessle and Dr. Petra Schiebel for their support in further education and for accepting all my requests for conferences, workshops, training, and trips. Also, many thanks to all my Bosch colleagues who helped me with the organization and their advice during my Ph.D. Especially to Balakrishna Chimmineni for helping me with the simulations. I would like to thank Dr. Christian Silber and Katrin Broermann for their support and help in building the packages. This was crucial for the results of this thesis.

Much appreciation goes to the colleagues from Laboratory for Optomechanics and Micro/nano Semiconductor/Photonics Systems, Professor Bongtae Han, Dr. Bulong Wu, and Yu-Hsiang Yang for Moiré measurements and for the warm welcome and enjoyable time during my visit at Maryland University.

Even all my stay was within the Bosch perimeter, I would like to thank all the ECTM colleagues for their warm welcome during every visit to Delft. Especially to Dr. Luke Middelburg and Dr. René Poelma for their support and constructive talks. I would like to acknowledge all the people that I might have forgotten at this point; your contribution has undoubtedly by no means been less significant.

Many thanks to Prof. Dr. Olga Fink from ETH Zürich (ETHZ) for her guidance on reviewing a journal paper and inviting me to a talk at the Smart Maintenance Conference.

I would like to give special, sincere, and heartful thanks to my wife for her unconditional support and understanding during my Ph.D. time. My long working hours, struggling, and uneasiness are something that she was happy to cope with. As Professor Han once said, she also deserves a PhT (Put him Through). Once again, Dana, I much appreciate it. To my newborn son, Albert, who kindly reminded me what is important in life and to the joy he brought. To my brother and sister for their support and for sharing so many moments in this life.

Finally, I am grateful to have had the privilege of attending the prestigious Technical University of Delft. This experience has allowed me to work with some of the best and brightest. Thank you for this opportunity.

Curriculum Vitæ

Alexandru Prisacaru

23-03-1987	Born in Comanesti, Romania.

Education

2001–2005	Informatics and Mathematics Theoretical High School "Spiru Haret", Moinesti
2005–2009	Bachelor of Science Civil Engineering Technical University "Gheorghe Asachi",Iasi,Romania
2009–2011	Master of Science Structural Engineering Technical University "Gheorghe Asachi",Iasi,Romania
2013–2015	Master of Science Computational Engineering Ruhr University, Bochum,Germany
2016–2021	PhD. in Microelectronics Delft University of Technology *Thesis:* Prognostics and Health Management of safety relevant electronics for future application in autonomous driving *Promotor:* Prof. dr. G. Q. Zhang

Awards

2014	Ruhr-Universität Scholarship, Ruth und Gert Massenberg Stiftung.
2018	Best Poster Award, Eurosime Conference

List of Publications

.1. Journal Papers

1. **A. Prisacaru**, P. Gromala, B. Han, G. Zhang, *Degradation Estimation and Prediction of Electronic Packages using Data Driven Approach*, IEEE Transactions on Industrial Electronics, (2021).

2. **A. Prisacaru**, E. O. Guerrero, B. Chimmineni, P. Gromala, Y.H. Yang, B. Han, G. Q. Zhang, *Towards Virtual Twin for Electronic Packages in Automotive Applications*, Microelectronics Reliability, (2021).

3. **A. Prisacaru**, A. Palczynska, P. Gromala, B. Wu, B. Han, G. Zhang, *Accuracy of CMOS-Based Piezoresistive Stress Sensor for Engineering Applications of Thermal Loading Condition: Theoretical Review and Experimental Validation*, IEEE Sensors Journal, (2019).

4. P. Meszmer, M. Majd, **A. Prisacaru**, P. J. Gromala, B. Wunderle, *Neural Networks for Enhanced Stress Prognostics for Encapsulated Electronic Packages - A Comparison*, Microelectronics Reliability (2021).

5. A. Inamdar, Y.H. Yang, **A. Prisacaru**, P. Gromala, B. Han, *High temperature aging of epoxy-based molding compound and its effect on mechanical behavior of molded electronic package*, Polymer Degradation and Stability (2021).

6. Y.H. Yang, B. Han, **A. Prisacaru**, P. Gromala, S. Jiang, A. Sarwar, *In-situ service load monitoring of automotive electronic systems using silicon-based piezoresistive stress sensor*, Microelectronics Reliability (2020).

7. M. S. Ibrahim, J. Fan, W. K. C. Yung, **A. Prisacaru**, W. v. Driel, X. Fan, G. Q. Zhang *Machine Learning and Digital Twin Driven Diagnostics and Prognostics of Light-Emitting Diodes*, Laser & Photonics Review (2020).

8. **A. Prisacaru**, A. Palczynska, A. Theissler, P. Gromala, B. Han, G. Q. Zhang, *In-Situ Failure Detection of Electronic Control Units Using Piezoresistive Stress Sensor*, IEEE Transactions on Components, Packaging and Manufacturing Technology (2018).

9. B. Wu, D. Kim, B. Han, A. Palczynska, **A. Prisacaru**, P. Gromala, *Hybrid Approach to Conduct Failure Prognostics of Automotive Electronic Control Unit Using Stress Sensor as In Situ Load Counter*, IEEE Transactions on Components, Packaging and Manufacturing Technology (2018).

10. A. Palczynska, **A. Prisacaru**, P. Gromala, B. Han, D. Mayer, T. Melz *Towards prognostics and health monitoring: The potential of fault detection by piezoresistive silicon stress sensor*, Microelectronics Reliability (2017).

.2. CONFERENCE PAPERS

11. **A. Prisacaru**, P. J. Gromala, *Aging of the Molding Compound Identification using Piezoresistive Silicon Based Stress Sensor*, 2021 22th International Conference on Thermal, Mechanical and Multi-Physics Simulation and Experiments in Microelectronics and Microsystems (EuroSimE).

12. **A. Prisacaru**, E. O. Guerrero, P. J. Gromala, B. Han, G. Q. Zhang, *Degradation Prediction of Electronic Packages using Machine Learning*, 2019 20th International Conference on Thermal, Mechanical and Multi-Physics Simulation and Experiments in Microelectronics and Microsystems (EuroSimE).

13. **A. Prisacaru**, Y. Sun, P. J. Gromala, B. Han, G. Q. Zhang, *Internal stress state of TQFP subjected to liquid thermal shock using piezoresistive silicon stress sensor*, 2018 19th International Conference on Thermal, Mechanical and Multi-Physics Simulation and Experiments in Microelectronics and Microsystems (EuroSimE).

14. **A. Prisacaru**, J. M. Bagetti , P. J. Gromala, B. Han, G. Q. Zhang, *Prognostics and health monitoring of electronic system: A review*, 2017 18th International Conference on Thermal, Mechanical and Multi-Physics Simulation and Experiments in Microelectronics and Microsystems (EuroSimE).

15. **A. Prisacaru**, A. Palczynska, P. J. Gromala, B. Han, G. Q. Zhang, *Condition monitoring algorithm for piezoresistive silicon-based stress sensor data obtained from electronic control units*, 2017 IEEE 67th Electronic Components and Technology Conference (ECTC).

16. M. Majd, P. Meszmer, **A. Prisacaru**, P. J. Gromala, B. Wunderle, *Stress Prognostics for Encapsulated Standard Packages by Neural Networks Using Data from in-situ Condition Monitoring during Thermal Shock Tests*, 2020 21st International Conference on Thermal, Mechanical and Multi-Physics Simulation and Experiments in Microelectronics and Microsystems (EuroSimE).

17. A. Inamdar, **A. Prisacaru**, M. Fleischman, E. Franieck, P. J. Gromala, A. Veres, C. Nemeth, Y. Yang, B. Han, *Study of Thermal Aging Behavior of Epoxy Molding Compound for Applications in Harsh Environments*, 2019 IEEE 69th Electronic Components and Technology Conference (ECTC).

18. P. J. Gromala, M. Jeronimo, **A. Prisacaru**, M. Schulz, J. Keller, *Interface Fracture Toughness Characterization in Electronic Packages Using the Crack Surface Displacement Extrapolation Method*, 2018 IEEE 68th Electronic Components and Technology Conference (ECTC).

19. P. J. Gromala, **A. Prisacaru**, M. Jeronimo, H.-S. Lee, Yong. Sun, B. Han, *Non-linear Viscoelastic Modeling of Epoxy Based Molding Compound for Large Deformations Encountered in Power Modules*, 2017 IEEE 67th Electronic Components and Technology Conference (ECTC).

20. A. Palczynska, **A. Prisacaru**, P. J. Gromala, B. Han, D. Mayer, T. Melz, *Piezoresistive Silicon Stress Sensor As a Tool to Monitor Health of an Electronic System*, ASME 2017 International Technical Conference and Exhibition on Packaging and Integration of Electronic and Photonic Microsystems collocated with the ASME 2017 Conference on Information Storage and Processing Systems.

21. B. Wu, D. Kim, B. Han, A. Palczynska, **A. Prisacaru**, P. Gromala, *Hybrid approach to conduct failure prognostics of automotive electronic control unit*, 2017 IEEE 67th Electronic Components and Technology Conference (ECTC).

22. A. Palczynska, A. Sasi, M. Werner, **A. Prisacaru**, P. J. Gromala, B. Han, D. Mayer, T. Melz, *Simulation Driven Design of Novel Integrated Circuits–Physics of Failure Simulation of the Electronic Control Modules for Harsh Environment Application*, 2016 IEEE 66th Electronic Components and Technology Conference (ECTC).

23. A. Palczynska, **A. Prisacaru**, P. Gromala, B. Han, D. Mayer, T. Melz *Towards prognostics and health monitoring: The potential of fault detection by piezoresistive silicon stress sensor*, 2016 17th International Conference on Thermal, Mechanical and Multi-Physics Simulation and Experiments in Microelectronics and Microsystems (EuroSimE).

.3. BOOK CHAPTER

24. A. Inamdar, **A. Prisacaru**, M. Dressler, A. Kabakchiev, P. Gromala, *Degradation and remaining useful life prediction of automotive electronics*, Reliability of organic compounds in microelectronics and optoelectronics.

25. A. Inamdar, P. Gromala, **A. Prisacaru**, A. Kabakchiev, Y. Yang , B. Han, *EMC oxidation under high temperature aging*, Reliability of organic compounds in microelectronics and optoelectronics.

.4. PATENT

26. **A. Prisacaru**, P. Gromala, *Method and Algorithm for Electronic Package Degradation Estimation*, IR-No. 2021/3754.